MEASUREMENT OF TRANSVERSE EMITTANCE IN THE FERMILAB BOOSTER

by

WILLIAM SPROULL GRAVES

A thesis submitted in partial fulfillment of the

requirements for the degree of

Doctor of Philosophy

(Physics)

at the

UNIVERSITY OF WISCONSIN — MADISON

1994

Abstract

A new beam profile monitor has been built and installed in the Fermilab Booster synchrotron. It nondestructively measures the beam's vertical density distribution on a fast turn-by-turn basis. This enables one to measure the beam's transverse emittance and to observe emittance growth as it occurs. For high intensities ($> 2 \times 10^{12}$ protons), the normalized 95% emittance was observed to grow from 6π mm-mrad at injection to 16π mm-mrad at extraction. The initial (< 5 msec) emittance growth and beam losses are shown to be caused by the space charge tune shift onto integer and 1/2 integer resonance lines. The growth near injection accounts for approximately 40% of the observed emittance increase throughout the acceleration cycle. The remaining 60% is due to two factors: slow linear growth due to betatron-motion driven by noise in the rf system; and faster growth after the transition energy that is caused by coupling of the longitudinal beam motion into the transverse planes.

Acknowledgements

Thanks to the staff in the Fermilab Booster Department for much help and guidance in the construction of the experiment and analysis of the results, particularly Ray Tomlin, Ken Koch, Jim Lackey, and my advisor, David McGinnis. Vinod Bharadwaj proposed this experiment and had many of the original concepts. Without his ideas it wouldn't have been possible.

Thanks to Don Reeder at UW-Madison for accepting an accelerator physics student and providing strong support in the UW Physics Department.

George Hendry of Cyclotron Inc. is responsible for introducing me to the field of accelerator design and helping push me on towards a PhD. He has provided guidance and enthusiastic support for many years.

To Janine, my wife, whose strong influence and high aspirations inspired me to earn a PhD, I dedicate this thesis.

Contents

List of Figures

List of Tables

Chapter 1

Introduction

1.1   High Energy Synchrotrons

The maximum energy attainable with particle accelerators has increased exponentially since the first electrostatic accelerators in the 1930's. The alternating gradient synchrotron[2] has driven this growth since its introduction in the 1950's. With strong transverse focusing and longitudinal phase stability, beam stability on the order of millions of orbits has been achieved. This has led to ever higher collision energies. The highest energies are reached by the large storage rings such as LEP at CERN which collides positrons and electrons with a center-of-mass energy of 110 GeV, and the Tevatron at Fermilab which collides protons and anti-protons with a center-of-mass energy of 1.8 TeV.

Modern accelerator complexes consist of several machines, each of which is particularly suited to a limited energy range. At Fermilab five accelerators, each one injecting into the next, accelerate protons and antiprotons from thermal energies to the final collision energy of 1.8 TeV in the center of mass. Linear accelerators are used to accelerate the beam to 200 MeV. From that energy on up, synchrotrons are used. The Booster synchrotron accelerates the

beam to 8 GeV, at which energy the particle velocity is quite relativistic at 0.994c. The Main Ring synchrotron then accelerates the beam to 150 GeV for injection into the Tevatron and antiproton production in the Antiproton Source. The Tevatron accelerates both protons and anti-protons to their final energy of 0.9 TeV.

1.2 Luminosity and Emittance

As the energy increases, the quality of the beam becomes critically important to observing the physics of interest. The beam densities must be very high in order to have appreciable event rates. The beams must also collide millions of times to produce the necessary events. Thus, not only must high density be attained, but also be maintained for long periods of time. Typical collider stores last 12 hours at Fermilab.

The luminosity of a beam is the interaction rate per unit cross section. For a bunched round gaussian beam it is given by

$$\mathcal{L} = f \frac{N^2}{4\pi\sigma^2},$$

where f is the frequency of collision, N is the number of particles per bunch, and σ is the rms width of the beam. The most recent collider run at Fermilab achieved $\mathcal{L} = 9.0 \times 10^{30} \text{cm}^{-2}\text{s}^{-1}$. In order to maintain high luminosity, accelerator physicists work to increase N and f, and reduce σ as much as possible. Interactions between particles within a bunch, between the bunches themselves, and between particles and their environment all conspire to limit the improvement in $\mathcal{L}$.

The mean square beam width is proportional to a quantity called emittance. The emittance is a measure of the phase space area (see Section 2.3.4) occupied by the beam. The expression for luminosity shows why small emittance is important to the success of the physics experiments. For a given number of particles, a large beam is less dense and so the event rate drops. This thesis is concerned with the measurement of emittance and the processes that lead to its growth.

The phenomena that increase emittance depend on the interaction of the beam particles' electric and magnetic fields with each other and the environment. The transverse electric and magnetic fields of a particle fall as $1/\gamma^2$ where $\gamma = E/mc^2$, so that many of these phenomena are most important in the lower energy accelerators.

1.3   The Fermilab Booster

The Booster is a high intensity, relatively low energy machine at Fermilab and so emittance preservation is important, but quite difficult. In fact, the beam's emittance more than doubles during its stay in the Booster. Efforts are underway to improve the Booster performance by raising the injection energy to 400 MeV. The following is a description of the components that make up the Booster, and details of its operation.

Table 1.1 shows the major parameters of the Booster. H^- beam is injected into the Booster at 200 MeV from the linac. During injection, the electrons are stripped from the H^- ions (Figure 1.1) and bare protons are accelerated to 8 GeV. The stripping process allows fresh H^- beam to be injected on top of
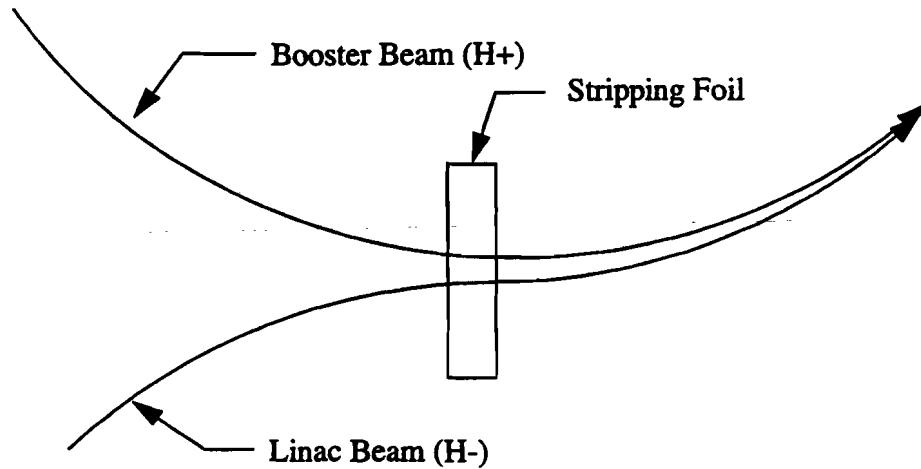
Figure 1.1: H^- stripping and injection into the Booster.

the existing beam in the ring. The low energy linac beam can then be of lower intensity to reduce the effect of space charge without compromising intensity in the later accelerators.

The Booster ring consists of 24 magnet periods. Each period is a set of combined function magnets[3] that both focus and bend the beam. The lattice consists of a horizontally focusing magnet followed by a short drift section, then two defocusing magnets separated by a long drift section, and finally another focusing magnet and short drift as shown is Figure 1.2. Nine of the long drift sections are taken up by rf accelerating cavities with two cavities per section. Three long drifts contain the injection and extraction lines. The long drifts are 6 m in length. There are also correction packages that consist of vertical and horizontal dipoles, quadrupoles, and skew quads. Sextupoles are present to correct the chromaticity (Section 2.3.6). Figure 1.2 shows the Booster lattice functions (see Section 2.3.2 for an explanation of lattice functions).
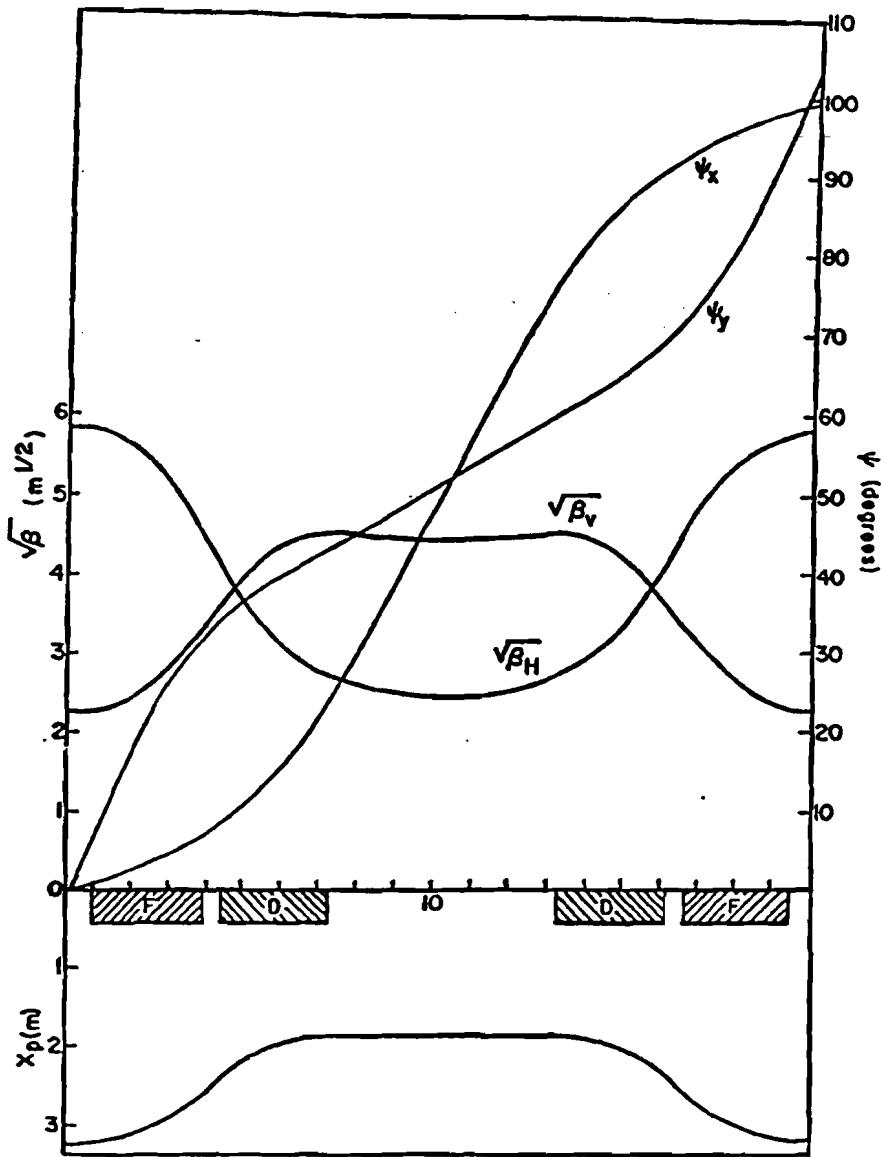
Figure 1.2: Booster lattice functions.

Table 1.1: Booster Parameters

Circumference	475 m
Particle Type	Proton
Injection Energy	200 MeV
Extraction Energy	8 GeV
Max Number of Particles Injected	4.0×10^{12}
Max Number of Particles Extracted	2.6×10^{12}
Transverse Tunes	$\nu_x = 6.7,\ \nu_y = 6.8$
Synchrotron Tune	.075 at injection, .015 at extraction
Period of Acceleration Cycle	33 msec
Number of Orbits in Cycle	$\approx 20,000$
Harmonic Number	84
Transition Energy	$\gamma = 5.5$
Average Vacuum	5×10^{-8} torr

1.4 Motivation for Thesis

The design intensity for the Booster is 4×10^{12} protons per cycle. However, beam losses in the first few milliseconds due to emittance growth reduce the typical operating intensity to 2.4×10^{12}. It has been suspected that space charge forces at low energy cause the beam emittance to grow until the combined effects of decreasing density, particle loss, and increasing energy ameliorate the driving force. The injected beam emittance is known from Linac measurements to be 7π mm-mrad. The extracted emittance has been measured to be 15π mm-mrad. For lack of a fast, nondestructive profile monitor it has not been possible to observe how and where in the acceleration cycle the emittance increase occurs. Analytical and computational work[4,1] has been done to investigate the causes of emittance growth in the Booster, and experiments[5] have been previously attempted, but suffered from uncertain time resolution.

This thesis will outline the task of building a device that measures the transverse beam profile on a short timescale (1 orbit) without interfering with the beam. The purpose of this thesis is to describe observations of emittance growth, understand what causes the growth, and finally prescribe remedies for the effects observed.

Chapter 2

Accelerator Physics

2.1 Introduction

In order to describe the phenomena that have been measured, a brief introduction to the language and terms of accelerator physics is necessary. A reference list of common accelerator terms and their definitions can be found in Appendix A. This chapter will mainly state results that are well-known, and so detailed derivations will be kept to a minimum. More detailed information can be found in the references in the bibliography, particularly the U.S. Particle Accelerator School Proceedings. This chapter closely follows the work in Reference 6.

The Booster is a synchrotron based on the alternating gradient or strong focusing principle. The beam consists of many protons circulating inside a ring shaped vacuum chamber. The beam is constrained by dipole magnets to follow a circle. Distributed radio-frequency (RF) cavities accelerate the beam in the longitudinal (z) direction and also provide longitudinal focusing. The dipole magnets increase their field synchronously with the beam's increasing energy to maintain the same radius of turning. Quadrupole magnets of alternating polarity provide transverse focusing so that individual protons within the beam
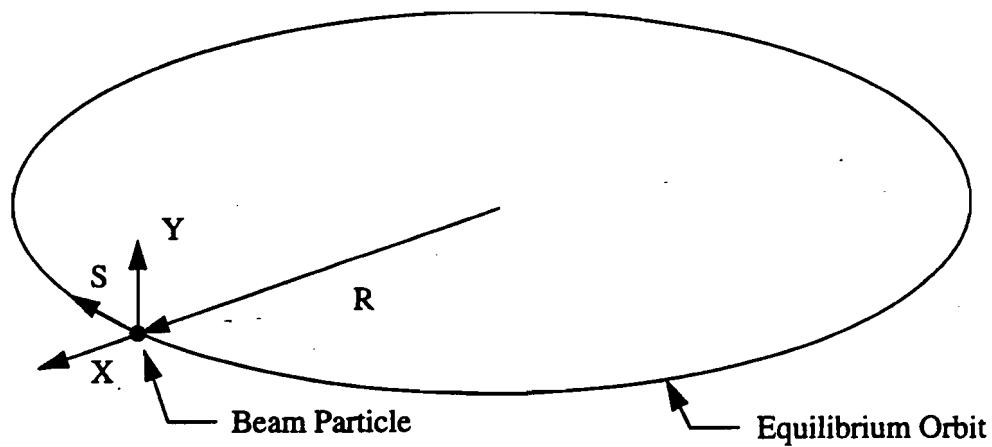
Figure 2.1: Coordinate system for particle motion.

execute small oscillations about a central reference trajectory. In the Booster, the quadrupole function and the dipole field are combined in one magnet. The x and y directions are defined perpendicular to the beam's direction of motion (see Figure 2.1), with x horizontal and y vertical.

2.2 Longitudinal Dynamics

Although this thesis is primarily concerned with transverse beam dynamics, longitudinal effects do show up in the measurements. The important concepts of synchrotron motion, longitudinal emittance, rf bucket area, and transition energy are therefore described.

2.2.1 Synchrotron Motion

The protons are accelerated by a series of radio-frequency (rf) cavities that oscillate at ω_{rf}. In the Booster there are 17 rf stations, each of which is resonant to the 84th harmonic of the particles' circular frequency. Thus there are 84 bunches in the ring during one pulse. At each cavity a particle will increase its energy by $eV \sin \phi$ where V is the peak cavity voltage and ϕ is the rf phase when the particle arrives. The ideal particle (called the synchronous particle) will arrive at phase ϕ_s with respect to the rf voltage. It is useful to discuss the particle dynamics of small deviations in phase and energy. In the discussion to follow, let

$$
\begin{aligned}
\tau &= \text{time spent between cavities} \\
v &= \text{particle speed} \\
L &= v\tau = \text{distance between rf cavities.}
\end{aligned}
$$

The variation in arrival time between cavities is

$$\frac{d\tau}{\tau} = \frac{dL}{L} - \frac{dv}{v}. \tag{2.1}$$

The fractional change in velocity can be written as

$$\frac{dv}{v} = \frac{1}{\gamma^2}\frac{\Delta p}{p}, \tag{2.2}$$

where $\gamma = E/mc^2$, p is the momentum, and Δp is the variation of a given particle's momentum from the ideal. The fractional change in path length between cavities is proportional to the particles' momentum,

$$\frac{dL}{L} = \frac{1}{\gamma_t^2}\frac{\Delta p}{p}, \tag{2.3}$$

where γ_t is a parameter known as the transition energy. Define the slip factor as

$$\eta = \left(\frac{1}{\gamma_t^2} - \frac{1}{\gamma^2} \right),$$ (2.4)

then Equation 2.1 becomes

$$\frac{d\tau}{\tau} = \eta \frac{\Delta p}{p}.$$ (2.5)

It is apparent that η will change sign as the particle accelerates from low energy through γ_t; hence the name "transition energy". The transition energy is a parameter of the accelerator lattice, and is due to the bending of the beam. A particle with an energy greater than the synchronous energy will bend at larger radius than the synchronous particle due to the dispersion (Section 2.3.5) of the lattice.

Below transition, the larger velocity of the high energy particle causes it to arrive *early in rf phase* relative to the synchronous particle (see Figure 2.2). In accordance with special relativity, the velocity of the particles increases more slowly as they reach higher energies. Thus particles of different energies have very nearly the same velocity. In that situation a particle with slightly higher energy than the synchronous particle will again follow a longer path, but now its velocity difference is not sufficient to overcome the time lost due to its greater path length. It will arrive at a *later rf phase* than the synchronous particle. The transition energy is the energy at which revolution time is independent of path length. This has important implications for the stability of the motion.

Each time a particle passes through a rf cavity, its energy is incremented.
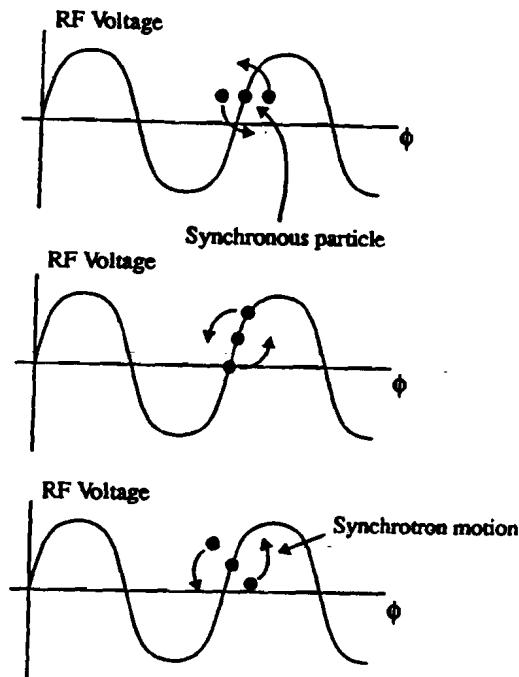
Figure 2.2: Particles oscillate in energy and phase (synchrotron motion) about the ideal particle .

The difference equations that describe the energy gain are

$$\Delta E_{n+1} = \Delta E_n + eV(\sin\phi_n - \sin\phi_s), \tag{2.6}$$

$$\phi_{n+1} = \phi_n + \omega_{rf}\eta\tau\left(\frac{\Delta p}{p}\right)_{n+1}, \tag{2.7}$$

where ϕ_n is the phase at the nth turn and ΔE_n is the energy gain at that turn. The energy gain at each cavity ($\approx$ 40 keV) is much less than the total kinetic energy ($>$ 200 MeV) and the phase shifts are small so that the difference equations may be approximated as differential equations.

$$\frac{d(\Delta E)}{dn} = eV(\sin\phi - \sin\phi_s), \tag{2.8}$$

$$\frac{d\phi}{dn} = \omega_{rf}\eta\tau\left(\frac{\Delta p}{p}\right). \tag{2.9}$$

Note also that

$$\frac{d(\Delta E)}{dn} = \beta^2\frac{\Delta p}{p}. \tag{2.10}$$

Combine the equations to get a single second order equation in phase:

$$\frac{d^2\phi}{dn^2} = \frac{2\pi h\eta eV}{\beta^2 E_s}\left(\sin\phi - \sin\phi_s\right), \tag{2.11}$$

where we have made the substitution $\omega_{rf}\tau = 2\pi h$. The ratio of the rf frequency to the revolution frequency is known as the harmonic number h. This equation is accurate provided that V varies very slowly and $\frac{dE_s}{dn} \ll E_s$.

For small deviations in phase ϕ the equations above may be linearized,

$$\phi \approx \phi_s + \Delta\phi\,, \ \Delta\phi \ll 1,$$

and

$$\begin{aligned}
\frac{d^2\Delta\phi}{dn^2} &= \frac{2\pi h\eta eV\cos\phi_s}{\beta^2 E_s}\Delta\phi \\
&= (2\pi\nu_s)^2\,\Delta\phi.
\end{aligned} \tag{2.12}$$

Stable solutions in phase require the coefficient of $\Delta\phi$ to be less than zero. At low energy $\gamma < \gamma_t$ implies that $\eta < 0$, therefore ϕ_s should be chosen such that $\cos\phi_s > 0$. Similarly, for $\gamma > \gamma_t$, the rf phase must be changed so that $\cos\phi_s < 0$. The number of phase oscillations per turn, ν_s is the synchrotron tune and is given by

$$\nu_s = \sqrt{-\frac{h\eta eV\cos\phi_s}{4\pi^2\beta^2 E_s}}. \tag{2.13}$$

At injection the Booster synchrotron tune is 0.0742 and at extraction it is 0.0013. At transition η goes to zero, thus longitudinal focusing is lost and the beam is unstable. Figure 2.3 shows several particle trajectories in longitudinal phase space. The closed orbits around the points $\phi = 0$ and $\phi = 2\pi$ show bounded oscillatory motion. The open orbits are unbounded motion. Particles on these orbits are lost to the beam pipe walls.
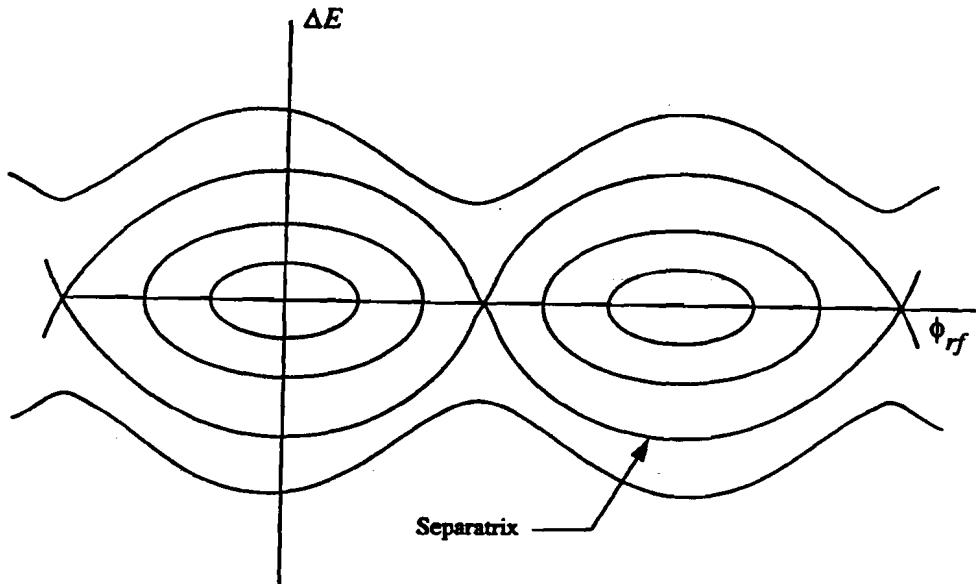
Figure 2.3: Particle trajectories in longitudinal phase space.

2.2.2 Longitudinal Emittance

The longitudinal phase space coordinates are ΔE-ϕ. As seen in Figure 2.3 there is a limited range of these coordinates for which the particle motion is oscillatory. The boundary between unbounded and bounded motion is known as the separatrix. The point p at ($\phi = \phi_s$, $\Delta E = 0$) is a stable fixed point - a particle at that point undergoes no phase motion. An unstable fixed point p' exists on the separatrix at $\Delta E = 0$. The area inside the separatrix is called an rf bucket, and the particles within one rf bucket are called a bunch. Figure 2.3 shows two buckets separated by 2π. There are 84 such buckets circulating in the Booster. The phase-space area that a bunch occupies is called the longitudinal emittance and is generally quoted in $E - \Delta t$ coordinates where $\Delta t = \frac{\Delta \phi}{\omega_{rf}}$. For $\phi_s = 0$ or π the area of the bucket is

$$A = \frac{16\beta}{\omega_{rf}} \sqrt{\frac{eVE_s}{2\pi h |\eta|}}. \tag{2.14}$$

This is known as a stationary bucket because the synchronous particle is not accelerated. The longitudinal emittance is then

$$\epsilon = \frac{\pi\beta(\Delta\phi)^2_{max}}{\omega_{rf}}\sqrt{\frac{eVE_s}{2\pi h|\eta|}}, \qquad (2.15)$$

where $(\Delta\phi)_{max}$ is the maximum phase excursion of any particle. It can be shown that the maximum phase excursion is proportional to the synchrotron tune. Liouville's Theorem requires the emittance to be constant. Thus at transition when $\Delta\phi \to 0$, $\frac{\Delta p}{p}$ becomes infinite. A more sophisticated analysis[6] would show that $\frac{\Delta p}{p}$ grows large but stays finite because at large amplitude the tune is amplitude-dependent. A large $\frac{\Delta p}{p}$ is undesireable for two reasons. First, sufficiently far away from the beam-pipe axis the guiding magnetic fields begin to weaken so that off-momentum particles may not be contained within the beam-pipe. This limit is called the dynamic aperture. Second, for a machine with large chromaticity (see Section 2.3), a spread in momentum may move parts of the beam onto destructive resonances in the transverse tune plane. The experimental data will show evidence of these effects.

2.3   Transverse Dynamics

The particles in a bunch are confined to oscillate transversely about the design or reference trajectory by guiding and focusing magnetic fields. The ideal particle would be on the design orbit. This section describes the motion of particles that deviate from the ideal.

2.3.1 Equation of Motion

The equation of motion for a charged particle in a magnetic field is

$$\frac{d\vec{p}}{dt} = e\vec{v} \times \vec{B}. \tag{2.16}$$

We will use the coordinate system shown in Figure 2.1. $\hat{x}$ and $\hat{y}$ are the transverse unit vectors and $\hat{s}$ is the unit vector in the particle's direction of motion. The local radius of bending is ρ. The vectors $\hat{s}$ and ρ refer to the design orbit. Assuming that the transverse velocities v_x and v_y are much less than the longitudinal velocity v_s, the equations of motion in x and y are

$$\frac{d^2x}{ds^2} = \frac{\rho + x}{\rho^2} - \frac{B_y}{(B\rho)}\left(1 + \frac{x}{\rho}\right)^2, \tag{2.17}$$

$$\frac{d^2y}{ds^2} = \frac{B_x}{(B\rho)}\left(1 + \frac{x}{\rho}\right)^2, \tag{2.18}$$

where the longitudinal position s is the independent variable. In general B is nonlinear in x and y. However, most of the physics of transverse motion may be illustrated by considering only linear fields. That is, assume that only dipole (bending) and quadrupole (focusing) magnets are present. Then the transverse equations of motion are

$$\frac{d^2x}{ds^2} = -\left[\frac{1}{\rho^2} + \frac{1}{(B\rho)}\frac{\partial B_y(s)}{\partial x}\right]x, \tag{2.19}$$

$$\frac{d^2y}{ds^2} = +\frac{1}{(B\rho)}\frac{\partial B_y(s)}{\partial x}y. \tag{2.20}$$

Both of these equations are of the form

$$u\prime\prime + K(s)u = 0, \tag{2.21}$$

where

$$K(s) = \frac{1}{(B\rho)}\frac{\partial B_y(s)}{\partial x} = \frac{B\prime}{(B\rho)}. \tag{2.22}$$

Equation 2.21 resembles the harmonic oscillator equation except that the spring constant is position dependent. A constraint on K is that it must be periodic because the accelerator is circular. The repeat distance is called the super period. The Booster has 24 super periods. The coefficient K is piecewise constant around the ring. Equation 2.21 (including the periodicity requirement) is known as Hill's equation and has a solution of the form

$$u = Ak(s)\cos[\psi(s) + \psi_0], \qquad (2.23)$$

where A and ψ_0 are specified by initial conditions relating u and s. This solution reduces to simple harmonic motion if $K(s)$ is a positive constant throughout the machine.

2.3.2 Courant-Snyder Parameters

The solution to Hill's equation is traditionally written in terms of the Courant-Snyder [2] parameters, $\alpha_\ell(s)$, $\beta_\ell(s)$, and $\gamma_\ell(s)$ as

$$u = A\sqrt{\beta_\ell(s)}\cos[\psi(s) + \psi_0], \qquad (2.24)$$

where

$$\beta_\ell(s) \equiv K^2(s), \qquad (2.25)$$

$$\alpha_\ell(s) \equiv -\frac{1}{2}\frac{d\beta_\ell(s)}{ds}, \qquad (2.26)$$

$$\gamma_\ell(s) \equiv \frac{1 + \alpha_\ell^2}{\beta_\ell}. \qquad (2.27)$$

β_ℓ is called the lattice function and α_ℓ is its derivative. Unfortunately, the symbols α, β, and γ are each commonly used to denote several different quantities. In this thesis, they will always have the subscript ℓ appended when they refer to the Courant-Snyder parameters.

The betatron phase advance between any two points s_1 and s_2 is then given by

$$\Delta\psi = \int_{s_1}^{s_2} \frac{ds}{\beta_\ell(s)}, \qquad (2.28)$$

and the total number of betatron oscillations per turn,

$$\nu \equiv \frac{1}{2\pi} \oint \frac{ds}{\beta_\ell(s)}, \qquad (2.29)$$

for either vertical or horizontal motion is called the betatron tune or transverse tune (Figure 2.4). For the Booster $\nu_x = 6.7$ and $\nu_y = 6.8$. Chapter 3 will show that it's very important to avoid tunes for which the fractional part is a low order rational number.

2.3.3 Matrix Description of Transverse Motion

At times it is convenient to use the closed-form solutions to the equations of motion that were just derived, and at other times (*e.g.* describing magnet errors) an alternative description based on matrices is a better choice. In this alternative approach the action of a magnet on a particle's motion is represented as a matrix acting on a vector.

The position and angle after passing through one magnet are given by

$$\begin{pmatrix} x \\ x' \end{pmatrix}_{out} = M_1 \begin{pmatrix} x \\ x' \end{pmatrix}_{in}, \qquad (2.30)$$

where M_1 is a matrix representing the action of the magnet. Some examples of magnet matrices are

$$M_{drift} = \begin{pmatrix} 1 & L \\ 0 & 1 \end{pmatrix}, \qquad (2.31)$$

Real Orbit
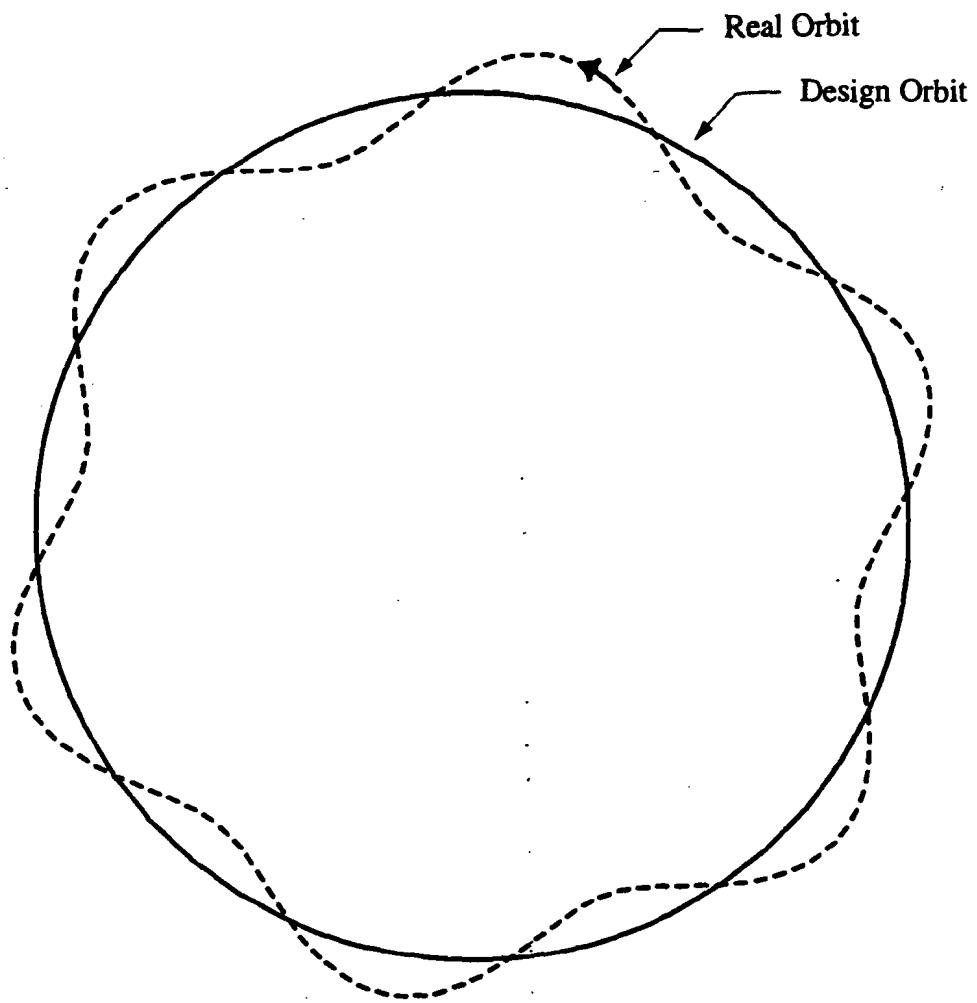
Design Orbit

Figure 2.4: Betatron motion about the design orbit. In this diagram the tune is 6.

$$M_{focus} = \begin{pmatrix} \cos(\sqrt{K}L) & \frac{1}{\sqrt{K}L}\sin(\sqrt{K}L) \\ -\sqrt{K}\sin(\sqrt{K}L) & \cos(\sqrt{K}L) \end{pmatrix}, \qquad (2.32)$$

$$M_{defocus} = \begin{pmatrix} \cosh(\sqrt{|K|}L) & \frac{1}{\sqrt{|K|}L}\sinh(\sqrt{|K|}L) \\ \sqrt{|K|}\sinh(\sqrt{|K|}L) & \cosh(\sqrt{|K|}L) \end{pmatrix}, \qquad (2.33)$$

where

$$K = \frac{B\prime}{(B\rho)} \qquad (2.34)$$

and L is the length of the magnet. A description of the whole ring can then be built up by multiplying the matrices for each element,

$$\begin{pmatrix} x \\ x\prime \end{pmatrix}_{s+C} = M_n \ldots M_3 M_2 M_1 \begin{pmatrix} x \\ x\prime \end{pmatrix}_s$$

$$= M \begin{pmatrix} x \\ x\prime \end{pmatrix}_s. \qquad (2.35)$$

where C is the ring circumference.

If the betatron wavelength is long compared to the magnet length, then a thin lense approximation may be used for the quadrupole magnets:

$$M_{focus} = \begin{pmatrix} 1 & 0 \\ -\frac{1}{f} & 1 \end{pmatrix}, \qquad (2.36)$$

where f is the focal length. This expression will be useful when the defocusing effects of space charge on the beam are calculated.

The single turn matrix M may be written in terms of the Courant-Snyder parameters as

$$\begin{pmatrix} x \\ x\prime \end{pmatrix}_{s+C} = \begin{pmatrix} \cos\psi + \alpha_\ell\sin\psi & \beta_\ell\sin\psi \\ -\gamma_\ell\sin\psi & \cos\psi - \alpha_\ell\sin\psi \end{pmatrix} \begin{pmatrix} x \\ x\prime \end{pmatrix}_s$$

$$= I\cos\psi + J\sin\psi, \qquad (2.37)$$

where ψ is the betatron phase advance in one revolution, I is the identity matrix, and

$$J = \begin{pmatrix} \alpha_\ell & \beta_\ell \\ -\gamma_\ell & -\alpha_\ell \end{pmatrix}. \tag{2.38}$$

2.3.4 Transverse Emittance

The expressions for position and angle (x and $x\prime$) can be used to derive an equation for the parameter A,

$$A\sqrt{\beta_\ell}\cos(\psi + \psi_0) = x, \tag{2.39}$$

$$-A\sqrt{\beta_\ell}\sin(\psi + \psi_0) = \alpha_\ell x + \beta_\ell x\prime. \tag{2.40}$$

From which

$$A^2 = \gamma_\ell x^2 + 2\alpha_\ell xx\prime + \beta_\ell x\prime^2, \tag{2.41}$$

which is the equation for the area of an ellipse. A is the invariant area of a phase space ellipse traced out by a particle as it oscillates (see Figure 2.5).

The emittance, ϵ of a beam is defined as the phase space area occupied by some fraction of the beam and is given by

$$\frac{\epsilon}{\pi} = \gamma_\ell x^2 + 2\alpha_\ell xx\prime + \beta_\ell x\prime^2. \tag{2.42}$$

A gaussian distribution is a reasonable model of the transverse density profile for the beam. The emittance may be written in terms of the rms beam width:

$$\epsilon = -\frac{2\pi\sigma^2}{\beta_\ell}\ln(1 - F), \tag{2.43}$$

where F is the fraction of beam inside the ellipse. At Fermilab, the emittance is traditionally defined as containing 95% of the beam, and so with this value
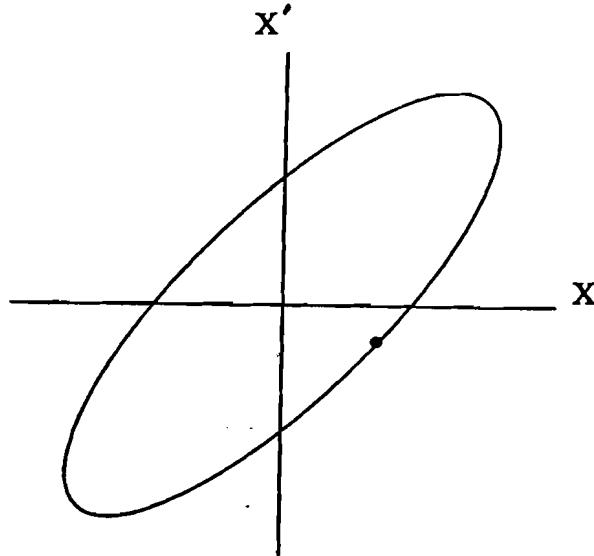
Figure 2.5: Phase space area traced out by a particle.

for F the emittance becomes

$$\epsilon = \frac{6\pi\sigma^2}{\beta_\ell}.$$ (2.44)

In the presence of dispersion, particles with different momentum travel on different closed orbits, which adds to the effective width of the beam. Dispersion is mainly a horizontal phenomenom due to the bending fields. The calculation above does not take dispersion into account. It is valid only in the vertical plane.

A useful expression is the maximum displacement from the ideal orbit given by

$$x_{max} = \sqrt{\frac{\epsilon\beta_\ell}{\pi}},$$ (2.45)

and the maximum angle given by

$$x\prime_{max} = \sqrt{\frac{\epsilon\gamma_\ell}{\pi}}.$$ (2.46)

The value of emittance given by Equation 2.44 assumes constant particle

momentum. However, if acceleration is considered the equation of transverse motion becomes

$$x'' + \frac{p'}{p}x' + \frac{eB'}{p}x = 0, \tag{2.47}$$

which is Hill's equation with a damping term. If the momentum is changing slowly, then the solution to this equation[6] is

$$x = A_0 \left(\frac{p_0}{p}^{1/2}\right) \sqrt{\beta_\ell} \cos[\psi + \psi_0]. \tag{2.48}$$

This indicates that the amplitude of the transverse oscillations damp with increasing particle energy. Therefore, in order to have an invariant emittance, the amplitude must be normalized in energy. In all of our subsequent discussion, the normalized emittance,

$$\epsilon_N \equiv \gamma\beta\epsilon, \tag{2.49}$$

will be used. At injection into the Booster, the normalized emittance is typically 6π mm-mrad. By the time of extraction the emittance has grown to 15π mm-mrad.

2.3.5 Dispersion

It has already been noted that particles of different momenta are deflected by different angles in the bending magnets. This means that off-momentum particles will oscillate about a different closed orbit than the design orbit. The momentum dispersion function is a characteristic of the accelerator lattice that is a measure of the displacement of the off-momentum orbit from the ideal. Because there is inevitably a spread in momentum within a bunch of particles, dispersion will increase the effective width of the beam.
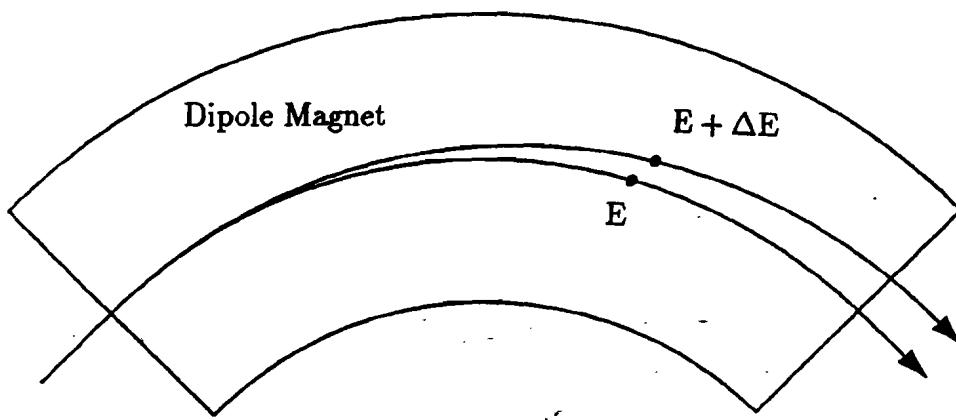
Figure 2.6: Momentum dispersion: particles with higher than synchronous energy orbit at larger radii.

Including only linearly varying fields, the equation for off-momentum particles is

$$x'' + \left[\frac{1}{\rho^2}\frac{2p_0 - p}{p} + \frac{B\prime}{(B\rho)}\frac{p_0}{p}\right] x = \frac{1}{\rho}\frac{\Delta p}{p}, \qquad (2.50)$$

where p_0 is the ideal momentum, p is the particle's momentum, and $B\prime = \partial B/\partial y$. This is an inhomogeneous Hill's equation. The solutions are of the form

$$x = D(s,p)\frac{\Delta p}{p_0}, \qquad (2.51)$$

where D is the dispersion function. Typical values of dispersion in the Booster are from 2 to 3 meters. The momentum spread $\frac{\Delta p}{p}$ is about .002 at injection. At transition, the spread in momentum becomes very large. Thus, in the presence of dispersion, beam may be lost on the vacuum pipe walls or it may wander outside the region of good magnetic field and be lost from the bunch.

The rms width of the beam in the presence of dispersion is given by

$$\sigma^2 = \frac{\epsilon_N \beta_\ell}{6\pi} + D^2 \left(\frac{\Delta p}{p}\right)^2. \tag{2.52}$$

This presents a difficulty when trying to measure the beam emittance with a single detector. We can no longer just measure σ to find ϵ because of the additional width due to the momentum spread. In general two detectors placed in regions of different dispersion are necessary to extract the emittance from the width measurement. However, since the beam is only bent in the horizontal plane, there is no (design) vertical dispersion. In that case the use of a single vertical detector can determine the (vertical) emittance.

2.3.6 Chromaticity

Off-momentum particles are also focused less (high momentum) by the quadrupole magnets, thus they have a different transverse tune (number of betatron oscillations per revolution) than the ideal particle. This is the same effect as chromatic aberration in an optical lense. The change in tune due to spread in momentum is called the chromaticity and is denoted by

$$\delta\nu = \xi(p)\frac{\Delta p}{p_0}. \tag{2.53}$$

This is the natural chromaticity due to the quadrupole magnets. The chromaticity has about the same magnitude as the betatron tune, but is opposite in sign,

$$\begin{aligned} \xi &= \frac{1}{4\pi} \oint K(s)\beta_\ell(s)\, ds \\ &= \frac{1}{4\pi} \oint \frac{B\prime}{(B\rho)}\beta_\ell(s)\, ds. \end{aligned} \tag{2.54}$$

To correct this effect, a magnet is needed for which the focusing strength is proportional to momentum. Since displacements in orbit are proportional to momentum as given by

$$x = D\frac{\Delta p}{p_0},\qquad(2.55)$$

the magnet should have a gradient that varies with transverse position. The sextupole field

$$B = kx^2,\qquad(2.56)$$

$$B\prime = 2kx,\qquad(2.57)$$

provides the correct type of field. Sextupoles are used to reduce the natural chromaticity of the machine to nearly zero. A large chromaticity is bad because, if the momentum spread becomes large (typically at the transition energy), then portions of the beam may cross resonance lines in tune space leading to emittance growth. The head-tail instability is also sensitive to the chromaticity. These phenomena are described in more detail in the next chapter.

Chapter 3

Transverse Emittance Growth

In an ideal accelerator, the emittance stays constant throughout the acceleration cycle. In real accelerators a number of factors cause the emittance to grow, leading to undesireable effects such as beam loss and a decrease in luminosity. This chapter will discuss several causes of emittance growth in a low energy accelerator. For the Booster, there are two times in the acceleration cycle where fast emittance growth is observed: (1) at injection, and (2) at the transition energy. At injection the beam is barely relativistic so that space charge forces are important. At transition longitudinal focussing is poor, so that there is often longitudinal growth which may be coupled into the transverse planes. In addition a slow linear growth is observed throughout the cycle which is probably caused by noise sources, some of which will be described below.

True emittance growth is an irreversible process. It is possible to reduce a beam's effective emittance using stochastic[7] or electron[8] cooling if the beam is stored for a long enough period. This is not possible for the fast cycling Booster.
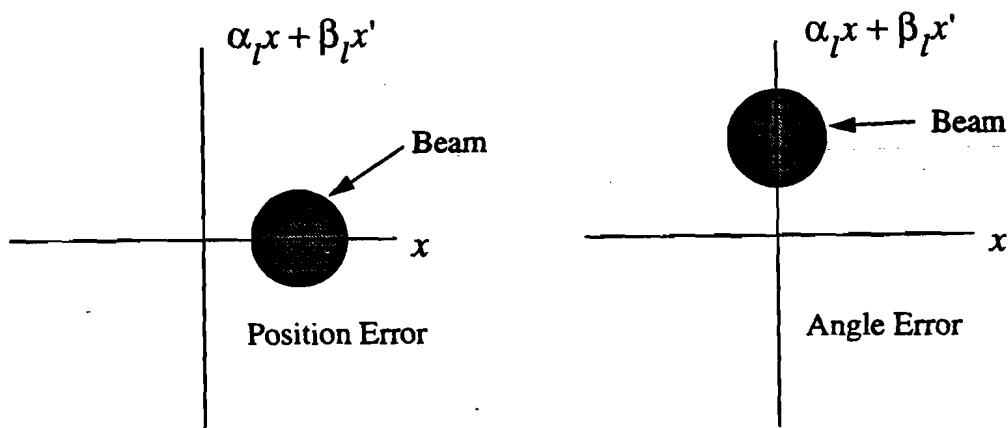
Figure 3.1: Beam steering errors at injection can be in position or angle.

3.1 Injection Errors

3.1.1 Beam Steering

Figure 3.1 shows a phase space plot of a beam that is injected at an offset in position. The phase space coordinates are chosen to be $(x, \alpha_\ell x + \beta_\ell x')$ so that the particle trajectories are circles instead of ellipses. Recall that the tune is defined to be the number of oscillations a particle makes about the phase space origin during one trip around the accelerator.

Figure 3.2 shows the phase space distribution as the betatron phase advances through 2π for an ideal accelerator. An ideal accelerator, in which the magnetic fields have at most a linear transverse variation, has a tune that is independent of betatron oscillation amplitude. For this case, the particle distribution rotates undisturbed about the phase space origin and no emittance increase results.
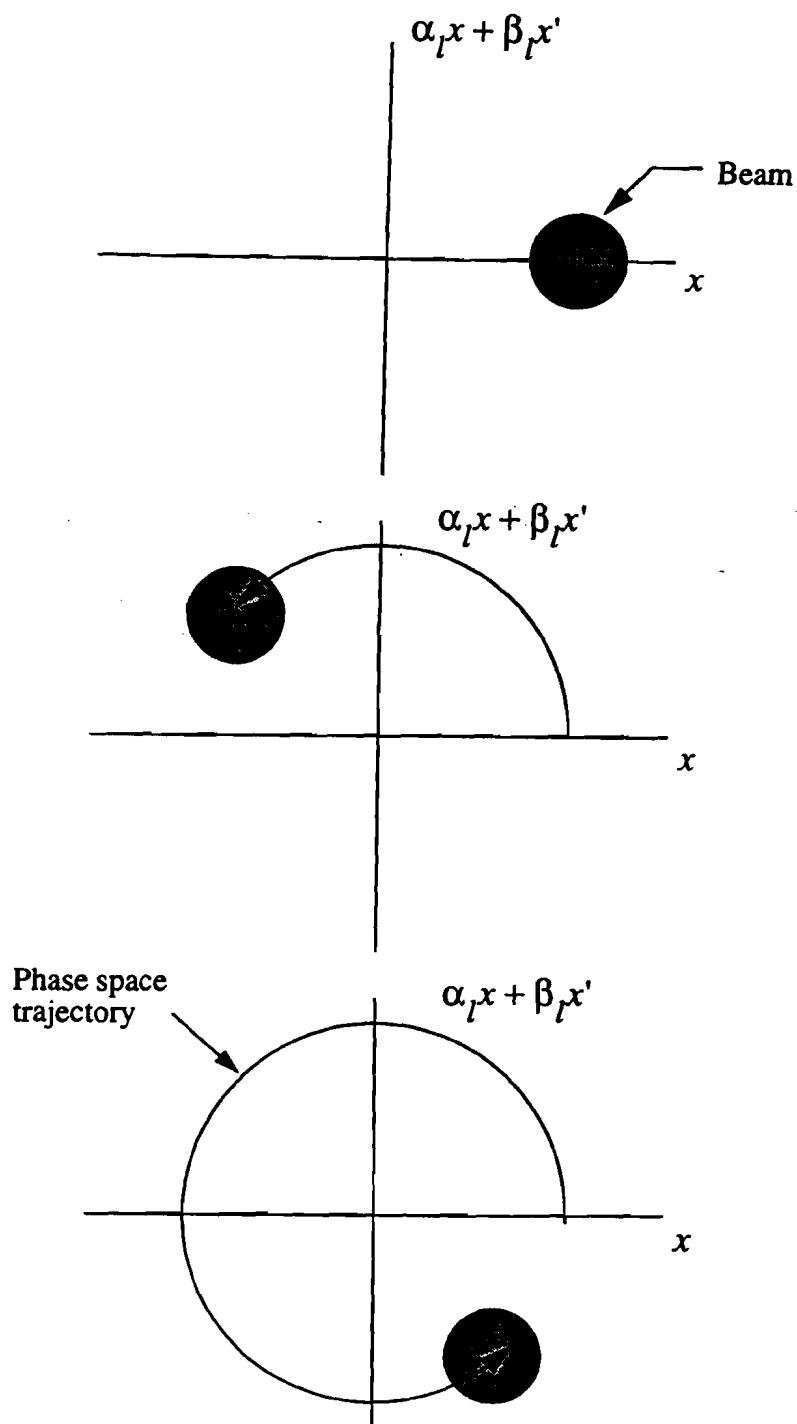
Figure 3.2: In the absence of nonlinear magnetic fields a beam injected off the phase space axis will revolve about the origin without distortion.
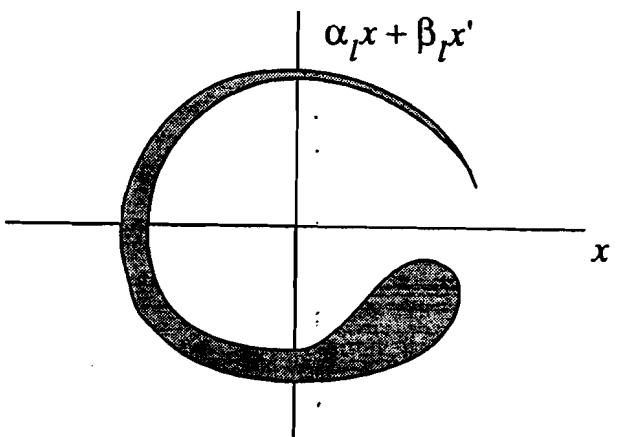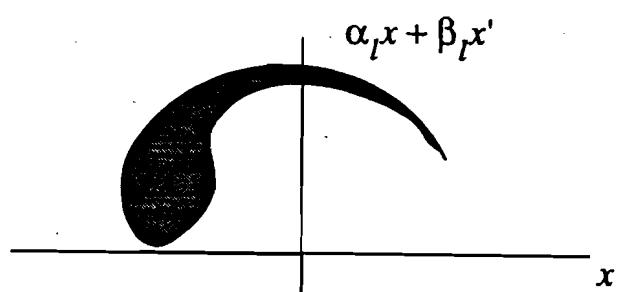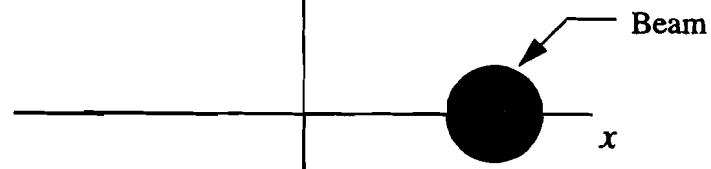
Figure 3.3: A beam steering error at injection in the presence of nonlinear magnetic fields causes distortions in the distribution.
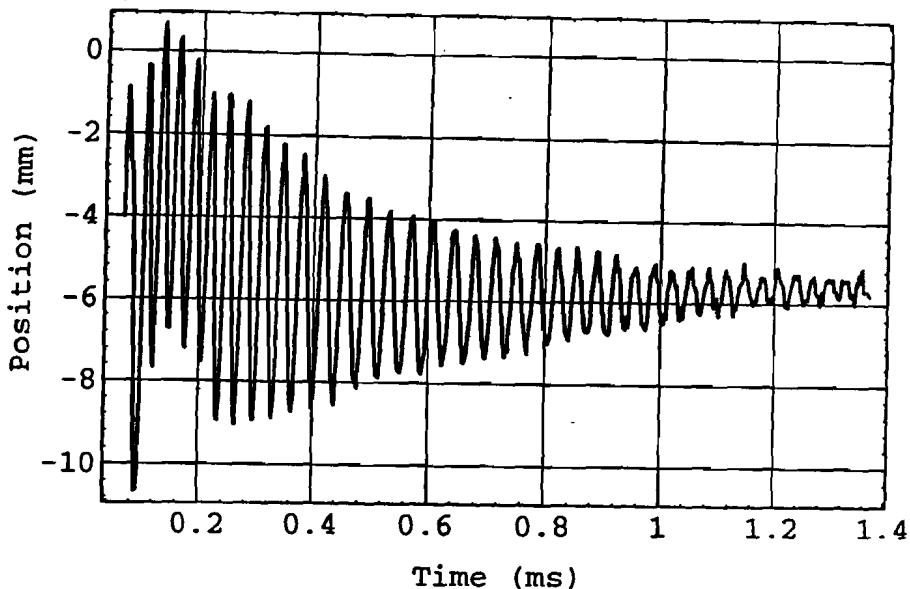
Figure 3.4: Measured beam position signal from IPM showing betatron oscillation and decoherence.

In a real machine, the fields have higher order multipole components due both to remanent magnetization in the iron and by design from sextupoles used to correct the chromaticity. The tune is then amplitude dependent, so that a beam injected off-axis in either angle or displacement will develop tails and eventually smear out to fill a larger phase space area. This type of emittance growth is called decoherence or filamentation. Figure 3.3 shows the evolution of the beam when nonlinear fields are included. For a beam that is injected with a position displacement Δx, the emittance will grow [6] by a factor

$$\frac{\epsilon}{\epsilon_0} = 1 + \frac{(\Delta x)^2}{2\sigma_0^2}, \tag{3.1}$$

where σ_0 and ϵ_0 are the original beam width and emittance. The typical injection error observed for the Booster is $\Delta x = 2.0$ mm. For a beam width of $\sigma_0 = 6.0$ mm, the emittance will increase by 10% over its initial value.

The betatron oscillations due to a beam that is injected off axis can be

$$\alpha_l x + \beta_l x'$$

Actual Trajectory
in Lattice

x

Mismatched Trajectory
at Injection
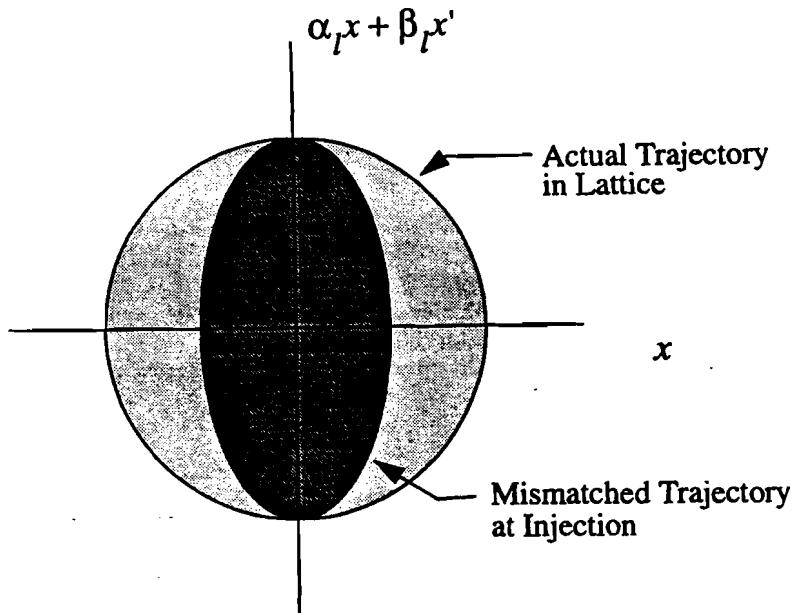
Figure 3.5: Lattice function mismatch at injection.

detected by a beam position monitor. Initially, a coherent oscillation at the betatron frequency is observed as the beam rotates about the origin in phase space. However, as the filamentation becomes substantial the coherent signal decays and the (now larger) beam is centered in phase space. Figure 3.4 is a plot of the beam centroid position vs time as measured by the ion profile monitor (IPM), and clearly shows the injection error and subsequent decoherence.

3.1.2 Lattice Mismatch

Another type of injection error occurs when the beam is steered correctly but the phase space ellipse isn't properly oriented to the accelerator lattice. Figure 3.5 illustrates the situation where the slope $\alpha_\ell(s)$ of the lattice function is not properly matched. In an ideal machine the ellipse would just tumble about the origin (Figure 3.6) and would be observed by a profile monitor as a quadrupole (width) oscillation. Again, in the real machine nonlinear magnetic fields cause filamentation (Figure 3.7) and subsequent emittance growth.
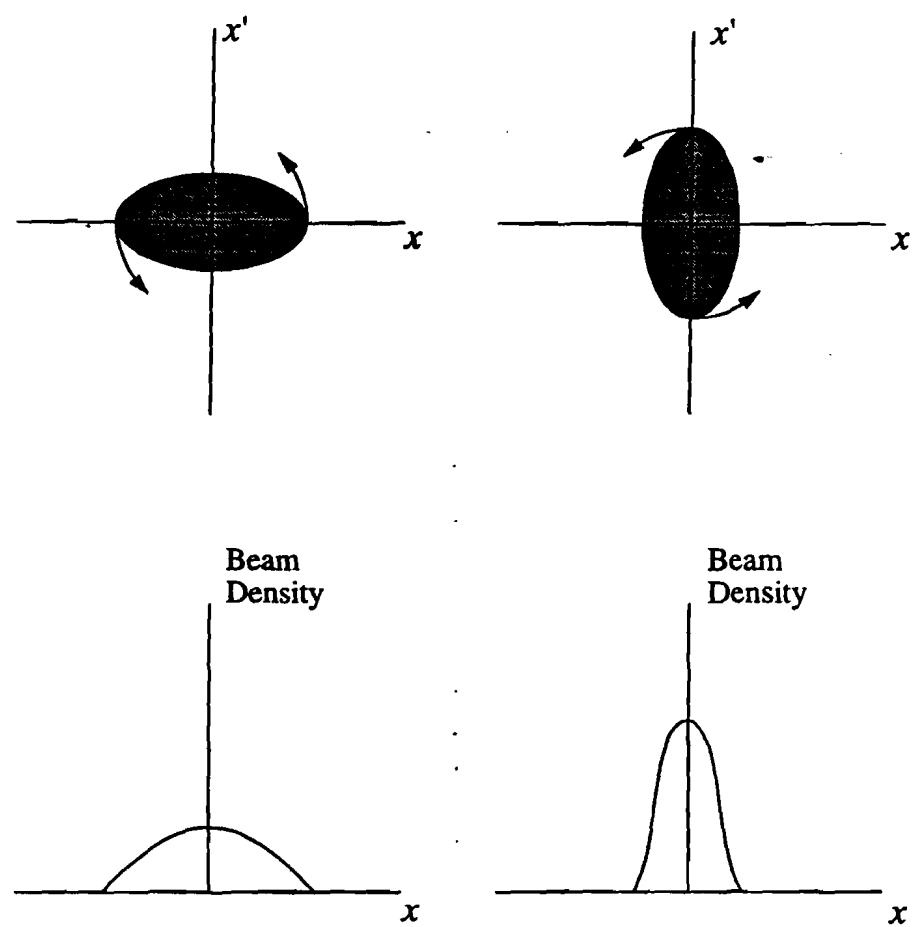
Figure 3.6: Phase ellipse tumbling and projection onto x axis.
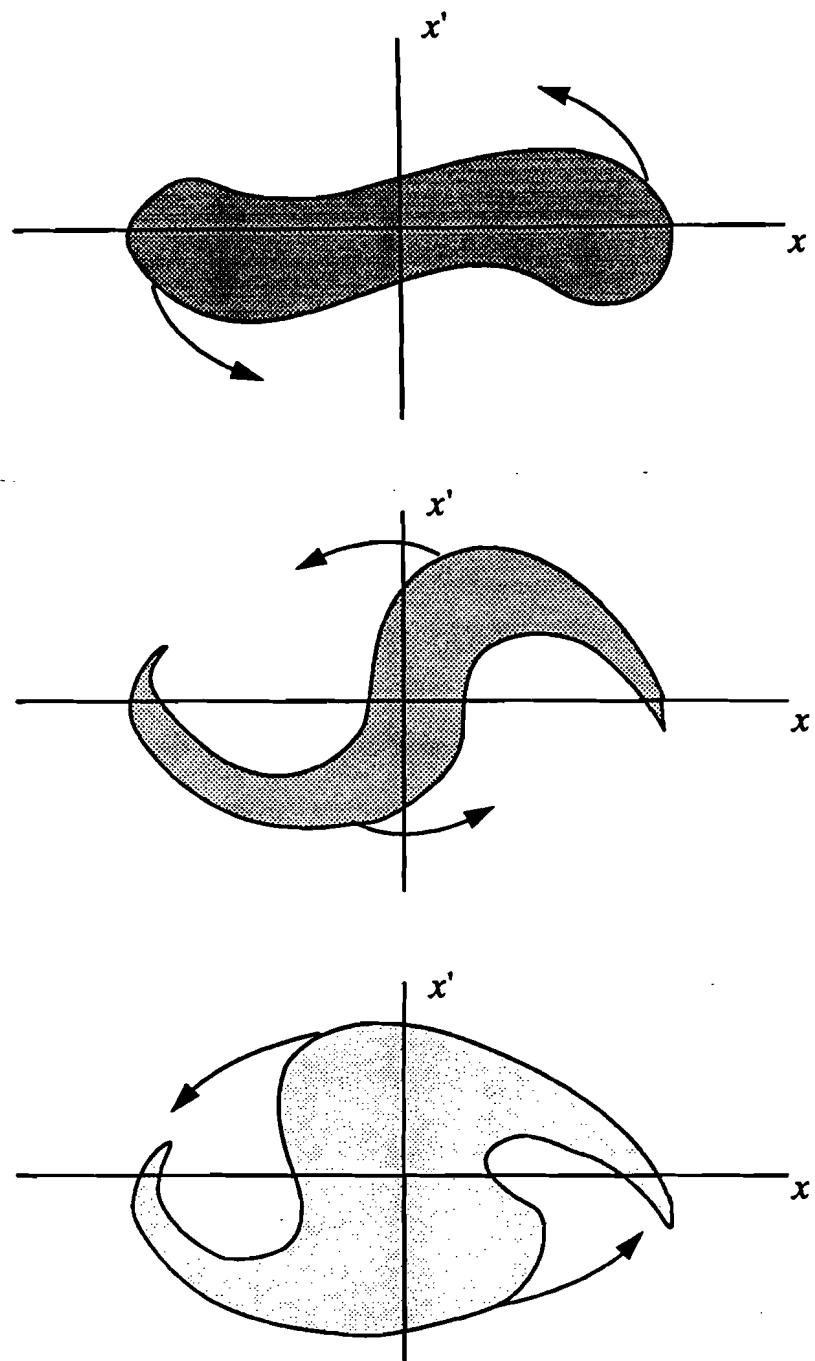
Figure 3.7: Phase ellipse tumbling with filamentation.

3.2 Resonance Lines in Tune Space

If the fractional part of the tune is a rational number, then as the particles repeatedly pass through a magnetic field imperfection at some point in the ring, the betatron oscillation will always have the same phase at the error, so that it will grow in amplitude from turn to turn. The growing amplitude is the same as emittance growth. This is true for all rational values of tune, but in practice only the low-order values such as 1, 1/2, 1/3 integer are strong enough to be of concern in a booster accelerator where the beam is not stored for long periods. Each resonance is driven by its corresponding magnetic multipole component, e.g. integer resonances are driven by dipole fields, 1/2 integer by quadrupoles, and 1/3 by sextupoles.

The effect of magnetic errors on particle motion can be given quantitatively by writing the linear oscillation as

$$x(s) = a\sqrt{\frac{\beta_\ell}{\beta_\ell^o}} \cos \Psi(s), \tag{3.2}$$

where β_ℓ^o is the amplitude function at the point of observation. As the other phase space coordinate use

$$\begin{aligned} y &= \beta_\ell(s)x' + \alpha_\ell(s)x \\ &= -a\sqrt{\frac{\beta_\ell}{\beta_\ell^o}} \sin \Psi(s). \end{aligned} \tag{3.3}$$

These phase space trajectories are again circles of radius a.

Suppose there is an error field ΔB acting over a distance Δs. If Δs is much shorter than the betatron wavelength, then $\Delta x = 0$ and $\Delta y = -\beta_\ell(s)\frac{\Delta B \Delta s}{B\rho}$ while the field acts. To find how the field affects a particle's amplitude and

phase expand Δx and Δy,

$$\Delta x = \frac{dx}{da}\Delta a + \frac{dx}{d\Psi}\Delta \Psi$$

$$= \sqrt{\frac{\beta_\ell}{\beta_\ell^O}}\cos \Psi(s)\Delta a - a\sqrt{\frac{\beta_\ell}{\beta_\ell^O}}\sin \Psi(s)\Delta \Psi \tag{3.4}$$

$$= 0.$$

$$\Delta y = -\sqrt{\frac{\beta_\ell}{\beta_\ell^O}}(\sin \Psi(s)\Delta a - a\cos \Psi(s)\Delta \Psi \tag{3.5}$$

$$= -\beta_\ell \frac{\Delta B\Delta s}{B\rho}.$$

In the absence of the error field the phase will advance as

$$\Psi(s) = \nu\phi(s) + \psi, \tag{3.6}$$

where ψ is the phase at the observation point on the first pass. The variable $\phi(s)$ advances 2π for each orbit around the ring. Solve for Δa and $\Delta \Psi$ to find

$$\Delta a = \frac{\beta_\ell^O}{B\rho}\sqrt{\frac{\beta_\ell}{\beta_\ell^O}}\Delta B\Delta s\sin \Psi, \tag{3.7}$$

$$\Delta \Psi = \frac{\beta_\ell^O}{B\rho}\sqrt{\frac{\beta_\ell}{\beta_\ell^O}}\frac{\Delta B\Delta s}{a}\cos \Psi. \tag{3.8}$$

At the observation point, the particle oscillation amplitude and phase will grow turn-by-turn as

$$\frac{da}{dn} = \frac{\beta_\ell^O}{B\rho}\oint ds\sqrt{\frac{\beta_\ell}{\beta_\ell^O}}\Delta B(x,s)\sin(\nu\phi + \psi), \tag{3.9}$$

$$\frac{d}{dn}(\psi - 2\pi\nu) = \frac{\beta_\ell^O}{B\rho}\oint ds\sqrt{\frac{\beta_\ell}{\beta_\ell^O}}\frac{\Delta B(x,s)}{a}\cos(\nu\phi + \psi). \tag{3.10}$$

Once the tune and rate of emittance growth are measured Equation 3.9 may be used to estimate the rms field-error of the multipole components in the ring. In the next two sections the explicit expressions for the emittance growth due to dipole and quadrupole field errors are derived.
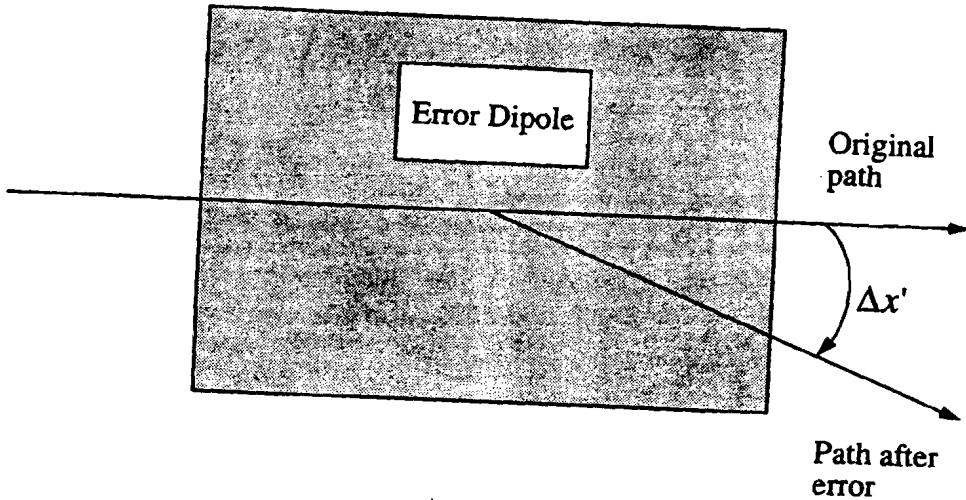
Figure 3.8: Angular kick from error dipole.

3.2.1 Integer Tune and Dipole Errors

If there is an incorrect dipole component in the ring, then each time a particle passes through that component it will receive a kick in angle as illustrated in Figure 3.8. If the tune is not an integer, then the particle will be at a different point on its phase-space ellipse each time it passes through the error field and so the effects of the angular kicks will average to zero. However, for integer tune the particle will have the same betatron phase at each pass and the kicks will add coherently as shown in Figures 3.9 and 3.10. The emittance will increase linearly with each orbit. The dipole multipole component is just a constant, $\Delta B = f_0$.

From Equation 3.9 the emittance growth due to dipoles of rms strength f_0
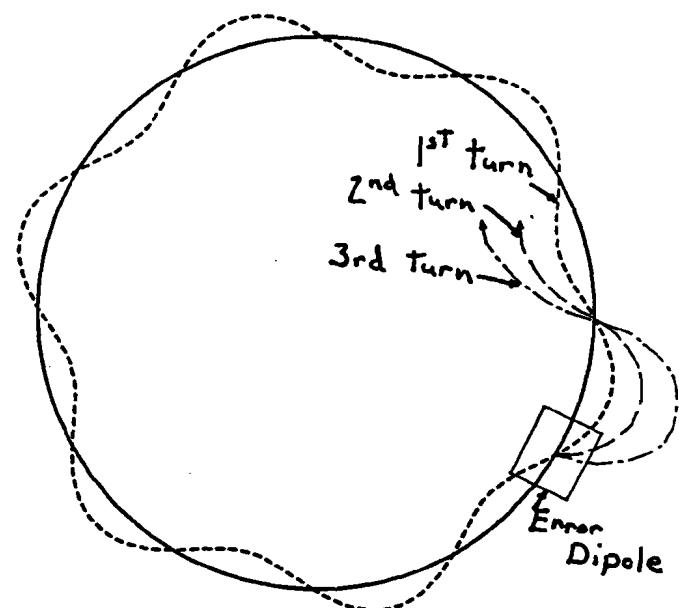
Figure 3.9: Effect of dipole magnet error on particle with integer tune - orbit deviation. Amplitude grows from turn to turn.
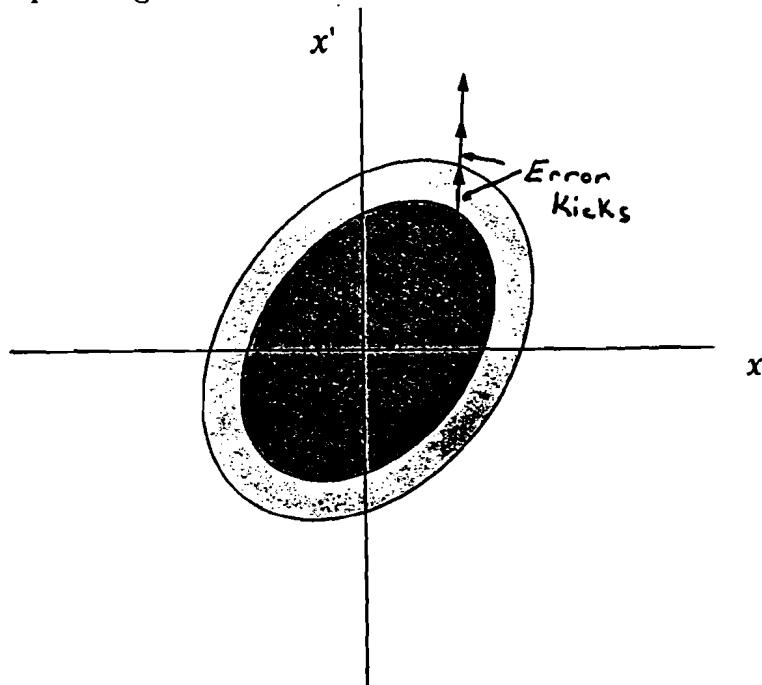
Figure 3.10: Effect of dipole magnet error on particle with integer tune - phase space.

distributed uniformly around the ring is

$$\frac{da}{dn} = \frac{\beta_\ell^0}{B\rho} \oint ds \sqrt{\frac{\beta_\ell}{\beta_\ell^0}} \Delta B(x,s) \sin(\nu\phi + \psi)$$

$$= \frac{\beta_\ell^0}{B\rho} \oint ds \sqrt{\frac{\beta_\ell}{\beta_\ell^0}} f_0(s) \left[\sin \nu\phi \cos \psi + \cos \nu\phi \sin \psi\right]. \qquad (3.11)$$

The initial phase ψ is arbitrary, so for convenience let $\psi = 0$. Then

$$\frac{da}{dn} = \frac{\beta_\ell^0}{B\rho} \oint ds \sqrt{\frac{\beta_\ell}{\beta_\ell^0}} f_0(s) \sin \nu\phi. \qquad (3.12)$$

There are a finite number of magnets in the ring, so the above integral can be made into a sum

$$\frac{da}{dn} = \frac{\beta_\ell^0}{B\rho} \sum_{i=1}^{N} \Delta s_i \sqrt{\frac{\beta_{\ell i}}{\beta_\ell^0}} f_{0i} \sin \nu\phi_i. \qquad (3.13)$$

Without knowledge of the exact distribution of errors, the best we can do is average over an ensemble of synchrotrons to find the rms value of $\beta_{\ell i} f_{0i}$,

$$\langle \frac{da}{dn} \rangle rms = 2\pi R \frac{\sqrt{\beta_\ell^0}}{B\rho} \sqrt{\frac{N}{2}} \langle \sqrt{\beta_\ell} f_0 \rangle rms. \qquad (3.14)$$

This equation tells us that, for integer tune, the average rate of amplitude growth due to dipole errors is constant as a function of turn number.

3.2.2 1/2 Integer Tune and Quadrupole Errors

If the fractional tune is 1/2, then the quadrupole components of the magnetic fields will cause the particle oscillations to grow. Figure 3.11 shows the orbit deviation caused by subsequent passes through an error in a focusing magnet. Figure 3.12 shows the phase space picture of the same situation.

The error field has the form $\Delta B = f_1 x$ where x is either transverse coordinate. Inserting this expression into Equation 3.9 the rate of emittance growth
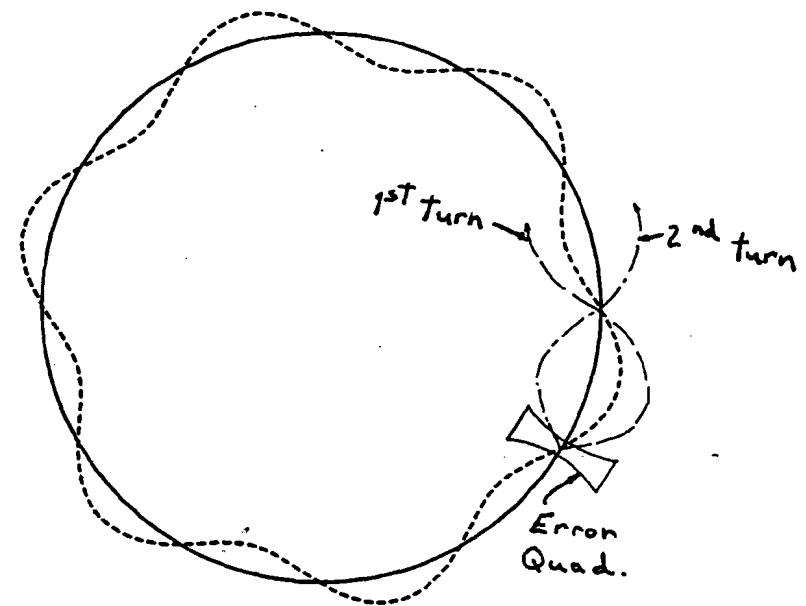
Figure 3.11: Effect of quadrupole magnet error on particle with 1/2 integer tune - orbit deviation.
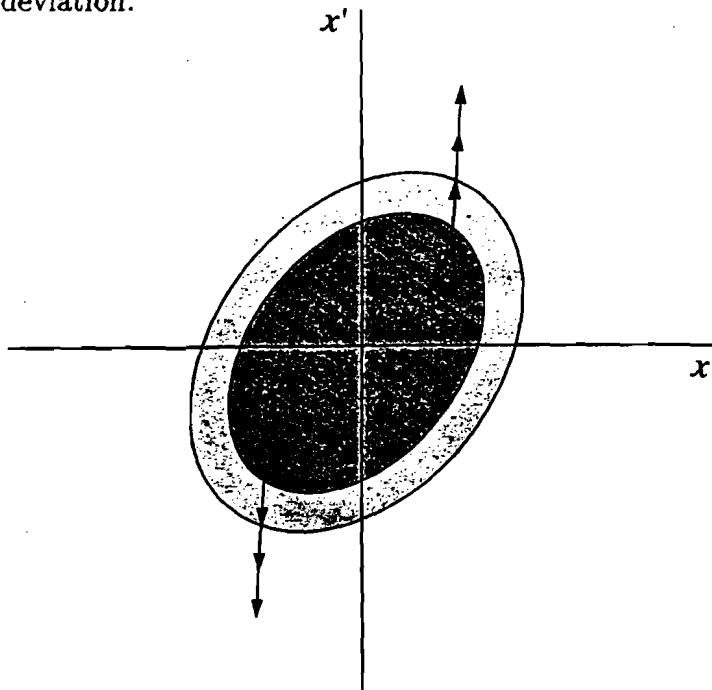
Figure 3.12: Effect of quadrupole magnet error on particle with 1/2 integer tune - phase space.

due to quadrupole errors is

$$\frac{da}{dn} = \frac{\beta_\ell^0}{B\rho} \oint ds \sqrt{\frac{\beta_\ell}{\beta_\ell^0}} f_1(s) x \left[\sin \nu\phi \cos \psi + \cos \nu\phi \sin \psi\right]$$

$$= \frac{a\beta_\ell^0}{2B\rho} \oint ds \frac{\beta_\ell}{\beta_\ell^0} f_1(s) \left[\sin 2\nu\phi \cos 2\psi + \cos 2\nu\phi \sin 2\psi\right]. \quad (3.15)$$

Again choosing a convenient value of ψ, the integral can be rewritten as

$$\frac{da}{dn} = \frac{a\beta_\ell^0}{2B\rho} \oint ds \frac{\beta_\ell}{\beta_\ell^0} f_1(s) \cos 2\nu\phi. \quad (3.16)$$

The argument to the cosine function indicates that for $\nu = 1/2$ integer, the amplitude will increase with each turn. The exact distribution of errors in the ring is unknown so we average over an ensemble to get

$$\langle\frac{da}{dn}\rangle rms = \frac{\pi R a}{B\rho} \sqrt{\frac{N}{2}} \langle\beta_\ell f_1\rangle rms. \quad (3.17)$$

Here, da/dn is proportional to a, which indicates exponential amplitude growth at the 1/2 integer tune.

The tune need not lie exactly on the resonance for emittance growth to take place. There is a range of tunes near the 1/2 integer for which particle growth occurs. This range is known as the stop-band width.[9] It's value is

$$\Delta\nu = \frac{1}{2} \frac{\beta_\ell^0}{B\rho} \oint ds f_1(s) \frac{\beta_\ell}{\beta_\ell^0} \cos 2\nu\phi. \quad (3.18)$$

This concludes the description of how emittance growth occurs when the tune is near a resonance line. Accelerators are designed to avoid placing the tune on low order resonances. In a particle collider where the beams are stored for many hours (typically 12 hours in the Tevatron), resonances up to order 10 are cause for concern. In the Booster (beam present for only 33 ms), the dipole and quadrupole field errors are the primary concerns. Despite the best

efforts of designers to avoid resonances, other physical effects conspire to move the design tune to a different value. The sections below describe some of these mechanisms.

3.3   Tune Shift Onto Resonance Lines

The operating tune of the machine is chosen to avoid sitting on any resonance lines. For the Booster, the tunes are $\nu_x = 6.7$, $\nu_y = 6.8$. This is the coherent tune which one could measure by perturbing the closed orbit and observing the frequency of the ensuing betatron oscillations of the beam centroid. However, particles within a bunch may have a tune quite different from the coherent tune. Two effects that can change the tune substantially are space charge forces within the beam and the differing focusing forces exerted by the quadrupoles on particles of different energies. Recall that this tune shift due to energy spread is called chromaticity.

3.3.1   Space Charge Tune Shift

The electrostatic repulsion of particles within a bunch acts to reduce the externally applied focusing force. This is particularly strong at low energy before the particles' fields are Lorentz contracted. A useful method of describing the effect of the space charge force is to examine its impact on the betatron tune.

We will assume the transverse density profile is gaussian in x and y. For a round bigaussian beam the net force due to space charge is given in the lab frame by [6]

$$\vec{F}_{sc} = \frac{e^2 NB}{4\pi^2 \epsilon_0 r R \gamma^2} \left(1 - e^{-r^2/2\sigma^2}\right) \hat{r}, \tag{3.19}$$

where B is a bunching factor, N is the number of particles in the ring, r is radial distance from the beam center, R is the ring radius, and σ is the rms beam width. F_{sc} is a defocusing force because it always points outward. At low energies ($\gamma \approx 1$) this force can be quite large for an intense beam. Near the center of the beam the force is linear in r,

$$F_{sc} \approx \frac{e^2 N B}{8\pi^2 \epsilon_0 R \gamma^2 \sigma^2} r, \quad (r \ll \sigma), \tag{3.20}$$

which makes it behave like a quadrupole magnet that defocuses in both the horizontal and vertical planes. We will treat the effect of space charge by considering it to be a continous quadrupole force distributed around the ring.

In the presence of space charge the equation of motion becomes

$$x'' + K(s)x = \frac{1}{\gamma m c^2 \beta^2} F_{sc}. \tag{3.21}$$

Inserting the expression for space charge,

$$x'' + \left(K(s) - \frac{r_0 N B}{2\pi R \sigma^2 \gamma^3 \beta^2} \right) x = 0 \tag{3.22}$$

$$x'' + [K(s) - \Delta K]x = 0. \tag{3.23}$$

where

$$r_0 = \frac{e^2}{4\pi\epsilon_0 mc^2} = 1.535 \times 10^{-18} \mathrm{m} \tag{3.24}$$

is the classical proton radius. If there were just one error quad present the thin lense matrix describing it would be

$$M = M_0 \begin{pmatrix} 1 & 0 \\ -\frac{1}{f} & 0 \end{pmatrix}, \tag{3.25}$$

where M_0 is the original single turn matrix. Taking the traces of the matrices on both sides of the equation and inserting the Courant-Snyder parameters,

$$\cos(2\pi\nu) = \cos(2\pi\nu_0) - \frac{\beta_\ell}{2f} \sin(2\pi\nu_0). \tag{3.26}$$

If the new tune, ν, is near the original, ν_0, then

$$\nu = \nu_0 + \Delta\nu, \tag{3.27}$$

$$\cos(2\pi\nu) = \cos[2\pi(\nu_0 + \Delta\nu)]$$

$$= \cos(2\pi\nu_0) + 2\pi\Delta\nu\sin(2\pi\nu_0). \tag{3.28}$$

Equating the above equation with Equation 3.26, the perturbation in tune is given by

$$\Delta\nu = \frac{1}{4\pi}\frac{\beta_\ell}{f}. \tag{3.29}$$

The focal length of the space charge "lense" is given by

$$\frac{1}{f} = \Delta K L, \tag{3.30}$$

where L is the interaction length and ΔK is given by Equation 3.22. Integrate the expression around the ring to find the total change in tune:

$$\Delta\nu = \frac{1}{4\pi}\oint_C \beta_\ell \Delta K\, ds$$

$$= -\frac{3r_0 NB}{4\pi R\gamma^2\beta}\oint_C \frac{\beta_\ell(s)}{6\pi\gamma\beta\sigma^2(s)}ds. \tag{3.31}$$

Recall that the normalized emittance is

$$\epsilon_N = \frac{6\pi\sigma^2\beta\gamma}{\beta_\ell}, \tag{3.32}$$

so that the space charge tune shift is given by

$$\Delta\nu_{sc} = -\frac{3r_0 NB}{4\pi R\gamma^2\beta}\oint_C \frac{ds}{\epsilon_N}$$

$$= -\frac{3r_0 NB}{2\gamma^2\beta\epsilon_N}. \tag{3.33}$$

Equation 3.33 is accurate for particles in a round gaussian beam near the beam center. This represents a maximum tune shift. Particles near the edge of the

bunch longitudinally or transversely will be shifted much less or not at all depending on the strength of the space charge force at their location. Since not all particles are shifted the same amount, this tune shift is called incoherent and cannot be measured by simply perturbing the beam and measuring the ensuing betatron oscillations. It can only be calculated by measuring the beam emittance and intensity to deduce the maximum shift.

Because the tune shift is proportional to $(\gamma^2\beta)^{-1}$, it is more pronounced at low energies. At injection into the Booster,

$$E = 200\text{MeV}$$
$$N = 3.5 \times 10^{12}$$
$$\epsilon_N = 7\pi\text{mm} - \text{mrad}$$
$$\beta = 0.55$$
$$\gamma = 1.2$$
$$1 \leq B \leq 2$$

therefore the maximum space charge tune shift is approximately

$$\Delta\nu_{sc} \approx -0.8! \tag{3.34}$$

This very large tune shift represents the spread in tunes within the beam. Particles must cross several low-order resonance lines, and so it isn't surprising that there is rapid emittance growth and beam loss at injection. This tune shift calculation indicates that the intense core of the bunch lies at an integer tune. This raises questions about the calculation because it is well known that the entire beam is lost in just a few turns when the coherent tune is deliberately set near an integer. However only a fraction (typically 30%) of the beam is

lost during normal operation. One explanation for the relatively small beam loss may be that the tune is now amplitude dependent, with the particles that experience the largest tune shift having small betatron amplitudes. The dipole errors in the ring quickly force the amplitude of these integer-tune particles to grow, which decreases the space charge tune shift, hence they move off the resonance. A computer study[4] has also shown that very large space charge tune shifts as calculated by the Laslett formula[10] can be supported, but that the rms tune shift of the whole beam cannot cross nearby low order resonance lines without severe beam loss and emittance growth. Our experimental data seems to support this view. Chapter 6 will describe the experimental results at injection in more detail.

3.3.2 Chromaticity

Recall that chromaticity is the tune shift due to momentum spread. This is because the strength of magnet focusing depends on the particles' momentum. Near transition the bunches become very short, that is, their spread in phase is small. Since emittance is conserved, the spread in momentum must get large. A large spread in momentum can put portions of the beam on nearby resonance lines in the presence of nonzero chromaticity. The "natural" chromaticity of a lattice is typically equal in magnitude but of opposite sign to the tune. This is reduced by the inclusion of sextupole magnets which provide focussing forces proportional to momentum. Above transition, the chromaticity must be slightly positive in order to avoid the head-tail instability.[11]

Another effect due to a spread in momentum is that the closed orbit differs for particles of differing momentum. For a large enough variation from

the design orbit, the particles travel outside the good-field region of the magnets. This is one mechanism whereby a longitudinal effect is coupled into the transverse motion. Chapter 7 will show striking examples of large amplitude transverse motion due to momentum spread just after transition.

3.4 Random Noise Effects

In the sections above the effect of dipole and quadrupole magnet errors on the beam was described. It was shown that if the tune is equal to a low order rational number, then the error kicks in the betatron angle or amplitude are additive from turn to turn, leading to emittance growth. A similiar problem arises even if the tune is not near a resonance line. Inevitably there are random noise sources that affect the beam. Examples are fluctuations in either the rf voltage[12,13] or magnet power supply currents, or in motion of the ground itself. If the noise source has power at the betatron frequency, then this noise will kick the beam in much the same manner as the magnet errors at resonance. The betatron frequency of the Booster is a few MHz, which is high enough to exclude the effects of ground motion and magnet power supplies. However, there is a large amount of rf voltage applied (750 KV/turn), and the rf cavities have a wide enough bandwidth that there may be significant power at the betatron sidebands.

The rf cavities are placed in the long straight sections where the dispersion function $D = 2.0$m and its derivative $D' = 0$. A particle passing through the cavity abruptly changes its momentum by an amount Δp. The closed orbit radius is changed by an amount $D\Delta p/p$ because of the non-zero dispersion ,

but the particle cannot instantly change its radius. Thus the particle begins executing a betatron oscillation of magnitude $D\Delta p/p$ around the new closed orbit. For a random noise source the kicks from turn to turn will be uncorrelated so that amplitude of the particle motion grows like a random walk. Phase space filamentation will cause the amplitude growth to become emittance growth. The dipole kicks caused by rf noise produce a linear rate of emittance growth given by [6]

$$\frac{d\epsilon_N}{dt} = 3\pi\gamma f_0 \mathcal{H}\frac{e^2\bar{V}^2}{\beta^3 E^2}. \tag{3.35}$$

where f_0 is the orbit frequency, $\bar{V}$ is the rms noise voltage, and

$$\mathcal{H} = \gamma_\ell D^2, \tag{3.36}$$

where γ_ℓ is the Courant-Snyder parameter. Chapter 7 will show emittance measurements that indicate linear emittance growth driven by rf noise is substantial in the Booster.

3.5 Instabilities

An instability is a coherent motion of the beam that grows with time. It may grow until the beam is lost, or other effects may damp the oscillation at some intermediate point. Even if the growth stops, the emittance will have been increased because of filamentation. The oscillation begins when a bunch passes through beamline structures such as rf cavities or bellows and excites electromagnetic fields. These fields can act back on the tail of the bunch or on following bunches causing distortions in their position or shape. The bunch oscillations then excite further fields. If the perturbation of subsequent

particles is in phase with the field oscillations, then bunch-shape distortions will feed back on the excited fields to create an instability in the beam motion. The fields induced in the structures are called wake fields and are a property of the structure. The Fourier transform of the wake field is the impedance seen by the beam. There are both longitudinal and transverse instabilities. The finite resistivity of the beam pipe is mainly responsible for the transverse modes. Longitudinal oscillations are excited primarily by parasitic rf cavity modes. The following sections qualitatively describe instabilities that have been observed in the Booster. See Reference 11 for a complete instability analysis, and Reference 14 for measurements of coupled-bunch instabilities in the Booster.

3.5.1   Wakefields and Impedance

A brief description of how the beam excites wakefields, and how the fields act back on the beam is given. We will focus on the longitudinal direction because it illustrates the essential physics involved.

A relativistic charge q_2 travelling a distance $c\tau$ behind another particle q_1 will gain (or lose) energy

$$\Delta E = q_2 \int ds_2 \vec{E}_1(s_2, \frac{s_2}{c} - \tau) \cdot \hat{s}. \tag{3.37}$$

The longitudinal wake potential is defined as

$$W_\parallel = \frac{\Delta E}{q_1 q_2}. \tag{3.38}$$

Generalizing this expression to a test particle trailing a distribution of particles given by

$$\int I(\tau) d\tau = Nq \tag{3.39}$$

yields a voltage drop of

$$V(\tau) = \int_{-\infty}^{\infty} d\tau' W_{\parallel}(\tau - \tau')I(\tau'),$$ (3.40)

where V is called the longitudinal wakefield. The Fourier transform of the wakefield is

$$\tilde{V}(\omega) = \tilde{W}_{\parallel}(\omega)\tilde{I}(\omega) = Z_{\parallel}\tilde{I},$$ (3.41)

where $Z_{\parallel}$ is the longitudinal impedance. The impedance is in general a complex quantity. Whether an oscillation is unstable or not depends on the nature of the impedance. The reactive part of the impedance causes a frequency shift in the normal-mode oscillation, but no growth, while the resistive part can cause growth or damping depending on whether it is negative or positive, respectively.

3.5.2 Longitudinal Modes

Any coherent instability can be described in terms of modes of oscillation. Two indices are necessary to describe any particular mode: one to describe the motion between bunches, and the second to describe distortions within a single bunch. Longitudinal oscillations are characterized by bunches differing in energy. For instance, suppose there are four bunches circulating in the ring. For the purposes of illustration we assume there is dispersion in the ring so that differences in energy cause the bunches to circulate at differing radii. A snapshot in time of the bunches (Figure 3.13) shows a number of oscillations in radial position around the ring. The number of oscillations around the ring is the coupled-bunch mode number.
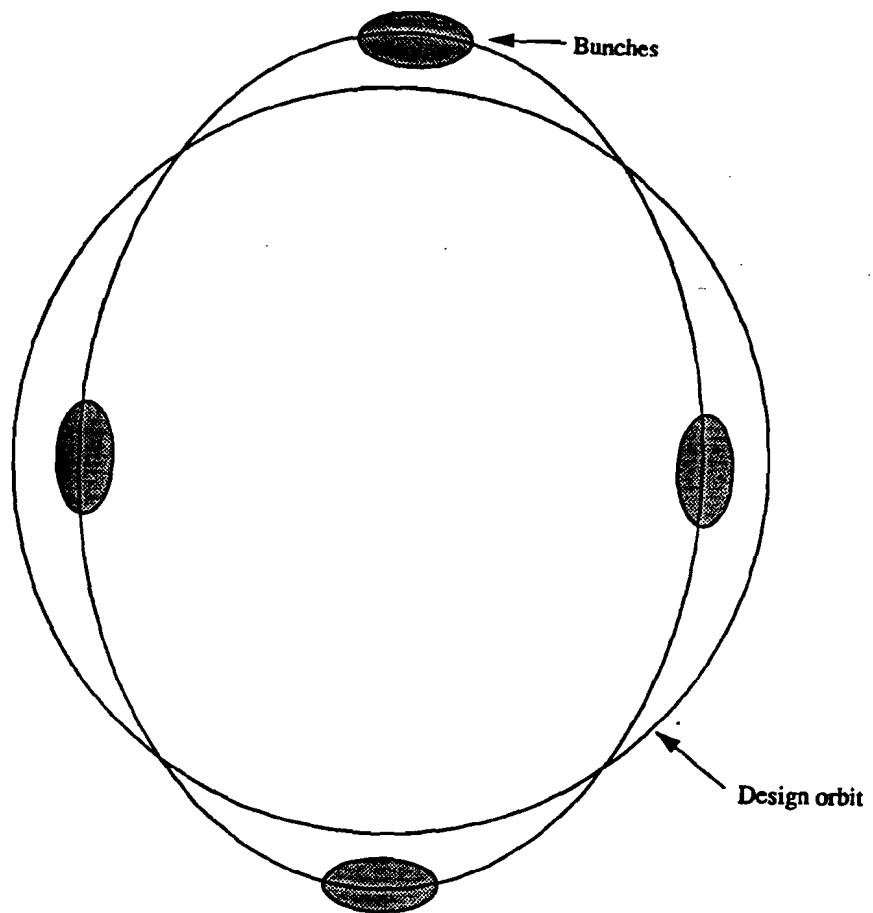
Figure 3.13: Mode = 2 coupled bunch instability. Bunch radial (energy) oscillations are 180 degrees out of phase.
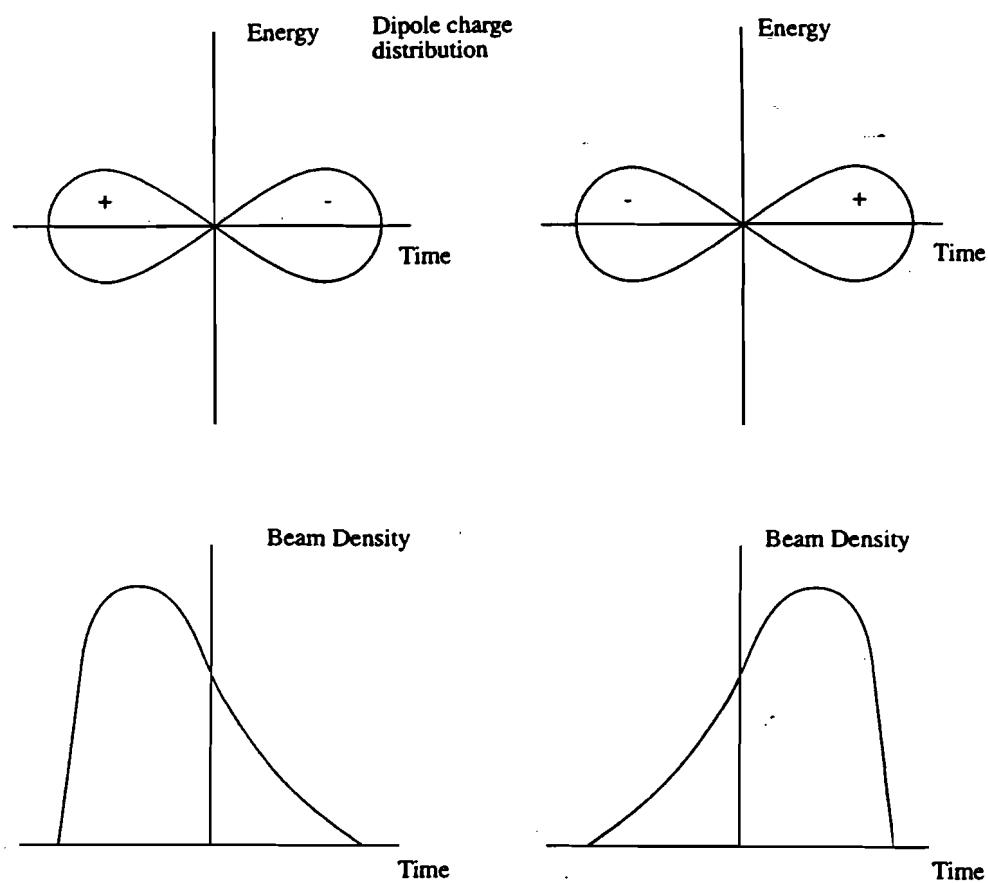
Figure 3.14: Upper figure shows dipole distribution in longitudinal phase space. Distribution rotates about about origin at frequency ν_s. Lower figure shows projection onto time axis.
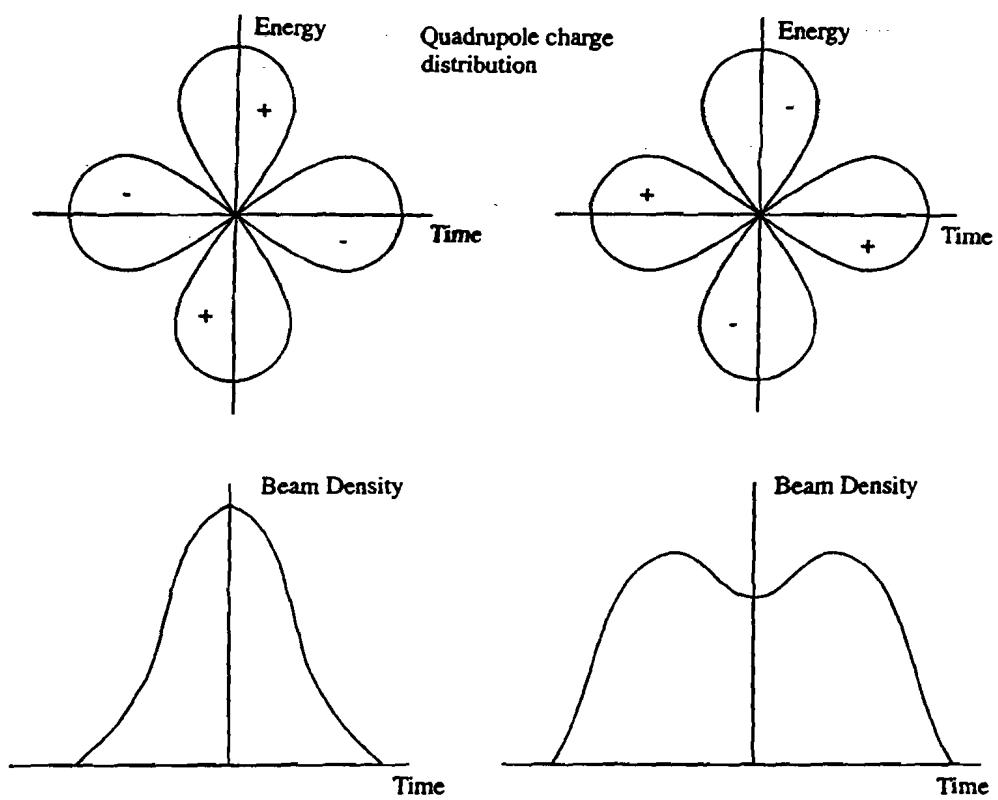
Figure 3.15: Upper figure shows quadrupole distribution in longitudinal phase space. Distribution rotates about origin at frequency ν_s. Lower figure shows projection onto time axis.
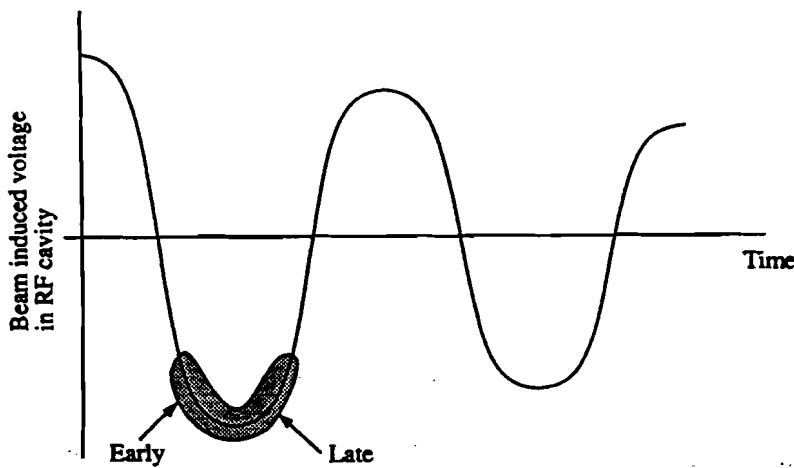
Figure 3.16: Cavity frequency set to $h\omega_{rf}$. No instability.

In addition to coupled-bunch motion, the wakefields excited by the bunches can change the charge distribution in each bunch. Figures 3.14 and 3.15 show the first and second (dipole, quadrupole) multipoles. These distortions have been observed with the IPM and are described in Chapter 7. Below, a particular mechanism that drives a representative instability is described in more detail.

Robinson Instability

The Robinson instability [15] was one of the first observed and is a good example of the beam-wakefield interaction. It is an interaction between the beam and a narrowband impedance such as an rf cavity. An rf cavity has a high quality factor (Q) at its fundamental mode so that it can efficiently store energy to accelerate the beam. The high Q means that the accelerating field decays slowly. The frequency of the cavity relative to the orbit frequency determines whether the beam's synchrotron oscillations are stable or unstable. Suppose the cavity fundamental mode is tuned exactly to the harmonic number times the revolution frequency, $\omega_{rf} = h\omega_{rev}$. Let there be just one bunch cir-
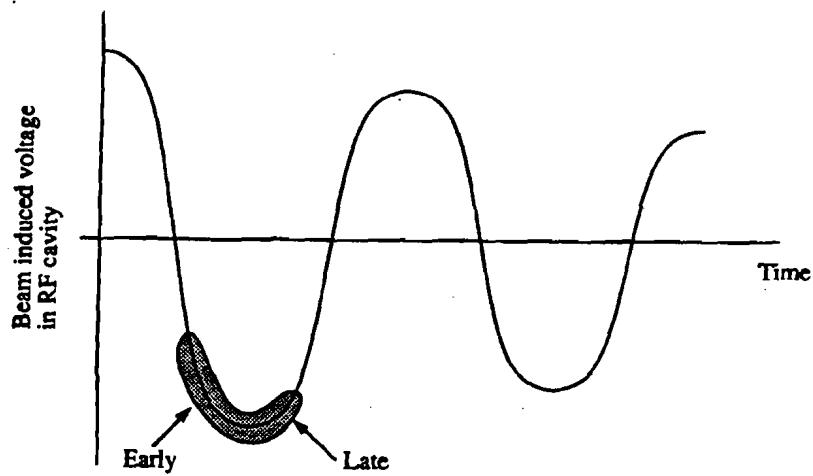
Figure 3.17: Cavity frequency set below $h\omega_{rf}$. Damping occurs.
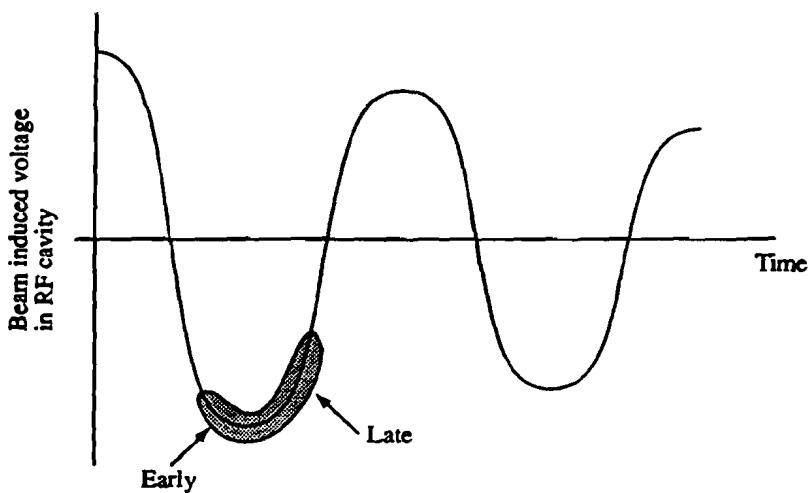
Figure 3.18: Cavity frequency set above $h\omega_{rf}$. Instability.

culating in the accelerator. As the bunch passes through the cavity on the first turn it excites a voltage as shown in Figure 3.16. The cavity rings at its fundamental mode. When the voltage is negative it will decelerate a beam. Particles in the bunch are undergoing synchrotron oscillations, so their phase at the cavity is modulated by the synchrotron frequency. Assuming the beam is above the transition energy, particles with more than the synchronous energy (E_s) will arrive late and particles with lower energy will arrive early in phase. Since the cavity is tuned to exactly $h\omega_{rev}$ particles above and below E_s will be decelerated the same amount on the next pass through the cavity. There is no instability. Now tune the cavity to a frequency just below $h\omega_{rev}$. High energy particles arrive late again, but the frequency shift means they will be decelerated more than the low energy particles (Figure 3.17). Over many turns this will reduce the amplitude of the synchrotron motion. It is again stable. Now suppose the cavity is tuned above $h\omega_{rev}$ (Figure 3.18). The late arriving high energy particles are decelerated less than the low energy ones causing the synchrotron amplitude to grow. This is the unstable oscillation. The rf frequency should be tuned just below $h\omega_{rev}$ for stable operation above transition. Below transition the frequency should be set just above $h\omega_{rev}$. This example considered just one bunch. For the case of many bunches, the dynamics are the same, and the motion of all of the bunches are in phase. This is a mode 0 coupled bunch instability.
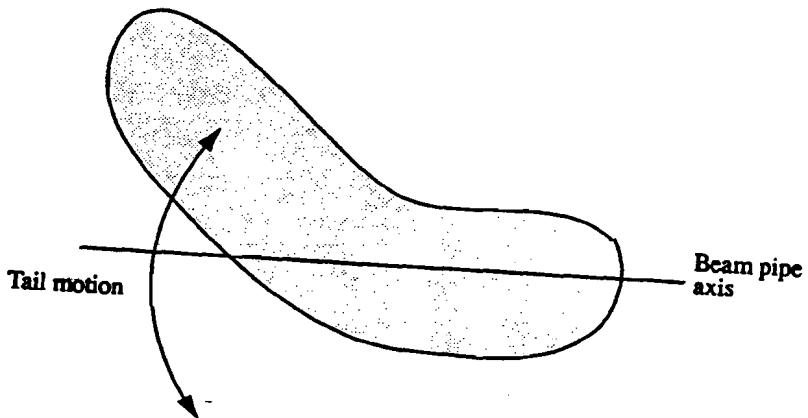
Figure 3.19: Head-tail instability.

3.5.3 Transverse Modes

A displacement of the beam from the beampipe axis can drive tranverse electromagnetic modes, particularly in the RF cavities. Figure 3.19 shows a transverse oscillation of the beam where the head's wakefields are deflecting the tail of the bunch. The bunch itself is distorted transversely, and the oscillation is called a head-tail mode. Higher order modes in RF cavities are the prime cause of this instability.

A simple model to illustrate the motion is to assume that the bunch is composed of two macroparticles, each of charge $Ne/2$, separated by a distance z (Figure 3.20). The leading macroparticle (head) will execute free betatron oscillations as

$$x_h = A \cos \omega_\beta t, \qquad (3.42)$$

while the trailing macroparticle (tail) will see a driving force due to the head's

$$\frac{Ne}{2}$$

$$\frac{Ne}{2}$$

Beam pipe
axis

z
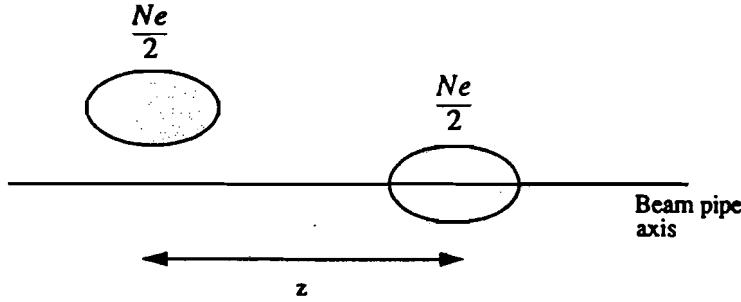
Figure 3.20: Macroparticle model of a bunch.

betatron motion. Its equation of motion can be expressed [11] in terms of the
1st order multipole as

$$\ddot{x}_t + \omega_\beta^2 x_t = \frac{Ne^2 W_1}{2m\gamma} A \cos \omega_\beta t, \tag{3.43}$$

where W_1 is the 1st order transverse wakefield. Thus the head drives the tail
at its betatron frequency. The solution to the this equation is

$$x_t(t) = A \cos \omega_\beta t + \frac{Ne^2 W_1}{4\omega_\beta m\gamma} A \sin \omega_\beta t. \tag{3.44}$$

The oscillation amplitude of the tail grows linearly with time.

This simple model is accurate in a linac, but in a circular machine there are
two important effects that modify the above results. The first is synchrotron
motion. If the synchrotron period is short relative to the growth time, then the
head and tail swap positions often enough to avoid growth. The second effect
is the variation of betatron frequency with momentum. Including momentum

spread in the above calculation[6] one finds a nonzero growth rate whenever the chromaticity is different from zero. However, the growth rate is very slow for chromaticity slightly negative below transition and slightly positive above it. [11]

The other transverse instability of note in the Booster is the resistive wall. [14] Transverse dampers have been installed that are designed to stop oscillations due to the resistive wall and head-tail instabilities. The signature of an instability is an oscillation at a particular frequency. We do not observe such motion with the dampers in operation and so regard instabilities as an unlikely source of emittance increase under the present operating conditions.

This completes the description of the processes that may lead to emittance growth. We find that the largest contributors to the emittance growth measured in the Booster are the space-charge tune shift at injection, and rf noise at later times in the cycle. After describing the experimental apparatus and its performance in the next two chapters, the measurement results will be presented to illustrate the concepts presented here.

Chapter 4

Experimental Apparatus

Now that the beam and its possible emittance growth mechanisms have been described we turn to a description of the experiment. There are four major components of the IPM; the detector itself that is installed in the beam pipe, the wide-band analog electronics that act as a preamp, the remote VME crate electronics that digitize and record the signal, and finally the software that controls the whole process.

4.1 Theory of Operation

As the beam particles speed through the vacuum pipe they occasionally collide with molecules of the residual vacuum gas. The number of ions produced by the collisions is directly proportional to the density of the beam. Therefore, if the ions are collected and the signal amplified, the original beam density can be deduced. The energy loss rate for a moderately relativistic particle of charge ze passing through a material of atomic weight A is given by [16]

$$-\frac{dE}{dx} = 4\pi N_A r_e^2 m_e c^2 z^2 \frac{Z}{A} \frac{1}{\beta^2} \left[\ln\left(\frac{2m_e c^2 \gamma^2 \beta^2}{I}\right) - \beta^2 \right],$$

where r_e is the classical electron radius, I is the ionization constant and is approximately equal to $16Z^{0.9}$ eV for $Z > 1$, and dx is measured in units

of g cm^{-2}. The composition of the vacuum gas is not known precisely, but is primarily water vapor and carbon monoxide. A rough estimate of A will suffice to calculate the expected signal strength. Use the following parameter values

$$
\begin{aligned}
A &= 25 \\
Z/A &= 1/2 \\
z &= 1 \\
I &= 100\text{eV} \\
\beta &= 0.994 \\
\gamma &= 9 \\
\text{vacuum gas density} &= 5.6 \times 10^{-14}\text{g/cm}^3
\end{aligned}
$$

to get

$$
-\frac{dE}{dx} \approx 9.0 \times 10^{-8}\text{eV/cm.} \tag{4.1}
$$

The maximum signal is expected to occur at the center of the beam near extraction when adiabatic damping has reduced the beam size. Assuming a round gaussian beam with rms width 2.0 mm, and intensity 2.5×10^{12}, the beam current density at the beam center is 21.1 μA/cm^3. The average rate of ion production is then

$$
\begin{aligned}
R &= \frac{N}{2\pi\sigma^2\tau I}\frac{dE}{dx} \\
&= 5.6 \times 10^9 \text{ ions/cm}^3\text{/sec,} \tag{4.2}
\end{aligned}
$$

where τ is the revolution period.

A transverse electric field is applied to the beam to collect the ions at the IPM pickup plate (Figure 4.1). The pickup plate is a micro-channel plate[17]

that is described in Section 4.2. Using the values from the equation above, the ion current density incident on the center of the plate is 0.5 nA/cm^2.

The IPM cannot distinguish single bunches, but instead averages its signal over several bunches. This is because of the long drift time from the beam to the pickup plate. The applied electric field is 700 V/cm and the pickup plate is 6 cm from the center of the beam pipe, thus the average drift time is 0.87 μs. At injection the orbit period is 3 μs and at extraction it's 1.6 μs. Therefore the signal from many bunches is mixed and the best time resolution is on-the order of 1/2 turn. Most of the phenomena that cause emittance growth occur on timescales of 1 turn or longer. Although higher order multipole distortion of the bunches can be (and are) observed with the IPM, coupled-bunch modes[11,14,18] with periods less than 1/2 a revolution will not be resolved.

4.2   Ion Profile Monitor

The IPM consists of a cyclindrical, stainless-steel vacuum chamber that bolts inline with the beam pipe (Figure 4.2). It is about 0.5 meters long and is placed in one of the empty long straight sections in the Booster. This particular vessel was used in a previous experiment[19] in the Antiproton Source. Inside the chamber are two parallel stainless-steel plates placed on either side of the beam. The plates are supported on ceramic insulators. High voltage leads to each plate provide the electric field used to clear the ions onto the microchannel plate (MCP). The MCP is inserted in a cutout in the negatively charged plate (cathode). The amplification of the MCP is controlled by varying the voltage on the cathode. The MCP is grounded through a voltage divider so that the
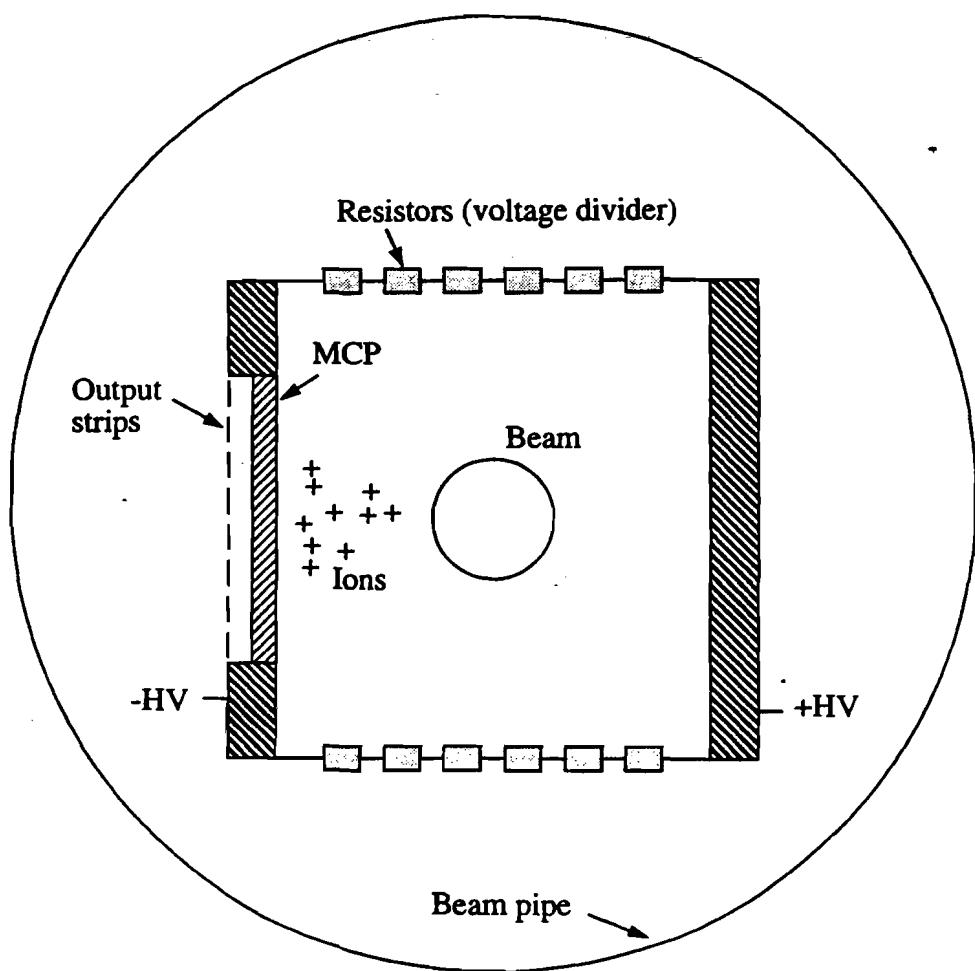
Figure 4.1: Ions created by beam drift to pickup plate in IPM.
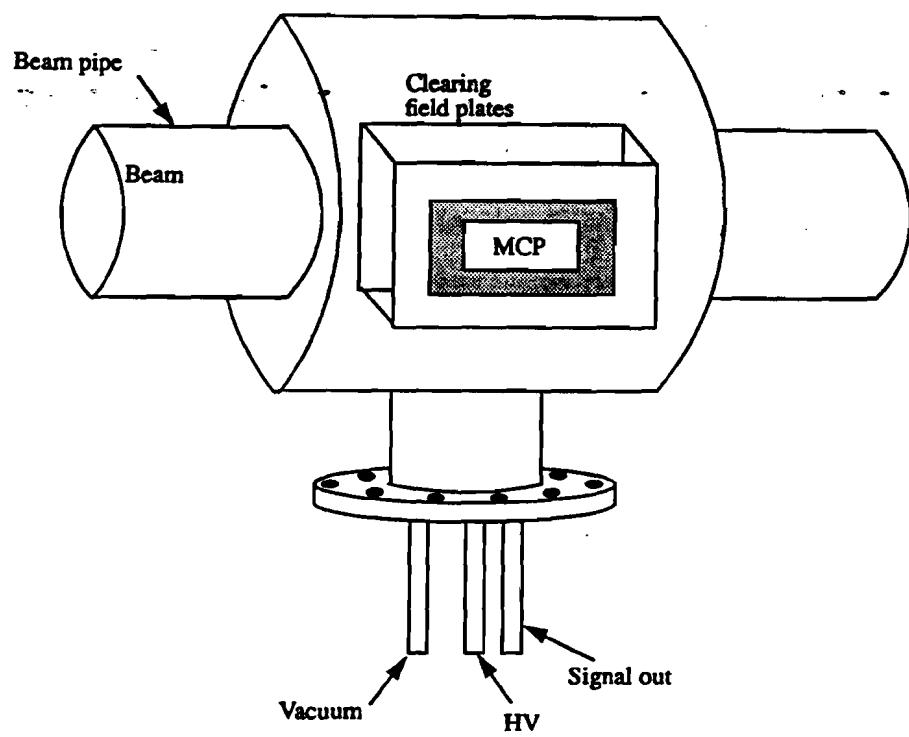
Figure 4.2: Ion Profile Monitor

rear side of it is slightly below ground. A multi-anode array of 48 channels is separated from the rear of the MCP by a 1.5 mm gap. The array is a printed circuit board with the channels laid out as copper strips running lengthwise along the direction of the beam. The 48 channels are then fed through the vacuum wall. Each channel has 1 cm^2 active area.

4.2.1   Micro Channel Plate

A Model 3810 MCP from Galileo Electro Optics[20] was chosen. It has dimensions of 8×10 cm. The MCP is a secondary electron multiplier that consists of millions of capillaries, each having an internal diameter of about 10 μm. The inside of each capillary is coated with a secondary electron emissive material and both ends of each channel are covered with a thin metal film that acts as an electrode. Thus each channel is an independent electron multiplier.

An incident ion strikes the side of one of the channels and secondary electron multiplication begins (Figure 4.3). Gains for a single MCP range from 10^2 to 10^4 as set by the voltage across the ends. Maximum voltage is 1 kV. For this application, typical voltage is 600V for a gain of a few hundred. The maximum linear gain is limited by distortion of the potential distribution near the output end. The maximum current sourced from the MCP should be kept below 5% of the strip current, where strip current is I_s = (applied voltage) / (plate resistance).

Dark current due to effects such as thermionic emission and ionization of residual gases is less than 1 pA/cm^2. The transit time for multiplication is less than 1 ns. When the MCP is excited by a pulse of ions, it outputs a pulse of electrons. For high intensities, there is a dead time after the pulse which will
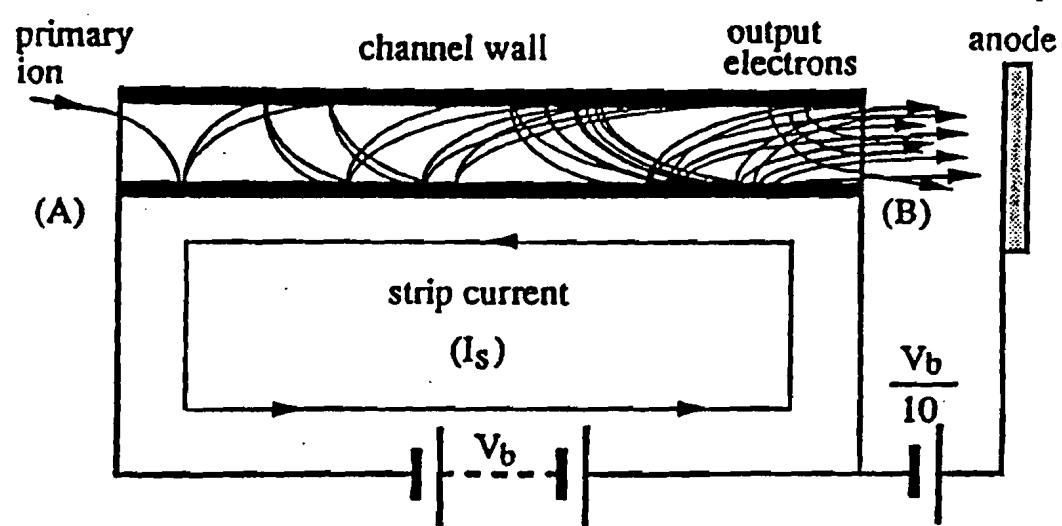
Figure 4.3: Electron multiplication in micro channel plate.

result in reduced gain. The gain voltage must be adjusted until no reduction in gain is observed for long pulses.

By reversing the leads to the high voltage clearing plates, one could multiply electrons instead of ions. The disadvantages of this are that the electrons have substantial transverse velocity from the ionizing event, distorting the profile, and the polarity on the MCP is such that an incident electron splashes secondary electrons into adjacent channels thus reducing the resolution.

As already stated, the maximum input signal on the MCP is expected to be 0.5 nA/channel. With a gain of 500 the amplified current signal will be 0.25 μA/channel.

4.3 Analog Preamp

The preamps are positioned within one meter of the beam pipe to keep the signal leads short in order to minimize stray capacitance. They are shielded by lead bricks for radiation protection. In addition, a quiet (in terms of beam loss) section was chosen in which to place the IPM to reduce radiation damage and noise.

Currently, 30 of the 48 channels from the MCP are in use. Each channel feeds into a separate analog preamp. The preamp was the most difficult part of the experiment to construct because the conflicting needs of wide bandwidth and high gain must be met. A two stage design based on opamps was used (Figure 4.4). Some of the key design features are the matched impedances of the first stage loop with the input line, the large resistor on the first stage input to reduce noise-voltage gain without affecting current-to-voltage gain,
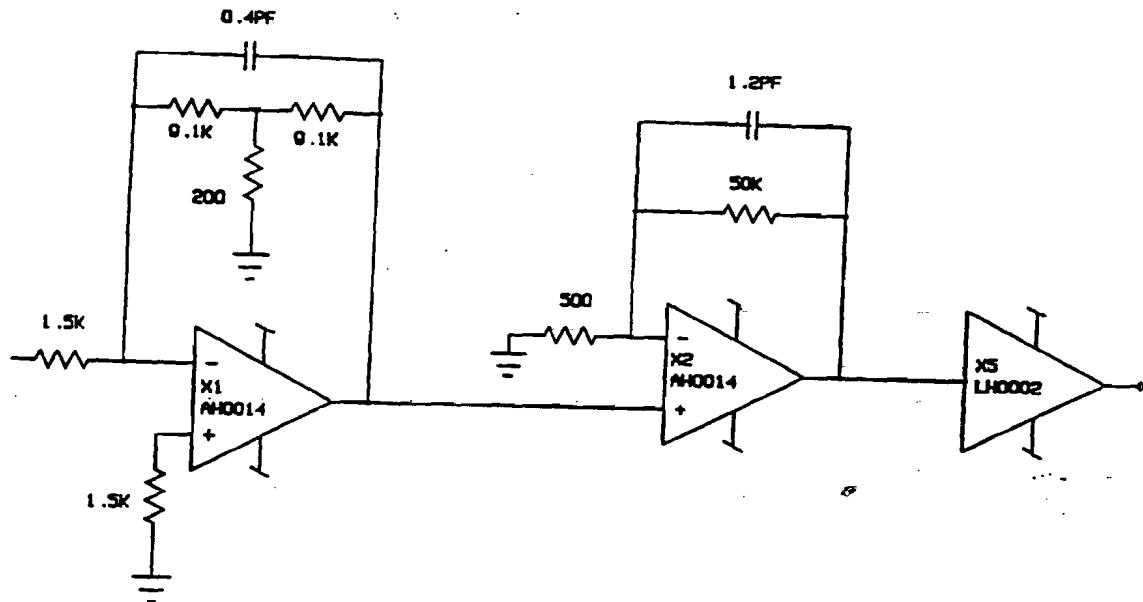
Figure 4.4: Analog preamp circuit.

and the careful grounding layout and shielding. Because of the large gain, careful layout and shielding (particularly of the first stage) is necessary to achieve stable operation.

The 3 dB point of the amps was set at half the maximum revolution frequency (630 kHz) to get single turn time resolution (Figure 4.5). The input signal is about $1/4$ μA for each channel, which should be amplified to a few volts before being sent on the long cable to the upstairs electronics. This requires a current-to-voltage gain of about 10^7. With a bandwidth of 320 kHz, that requires a gain bandwidth product of 3×10^{12}. FET input opamps from Optical Electronics [21] were chosen for their large gain bandwidth product and low noise. DC temperature drift has proven to be a problem, necessitating baseline correction in software.
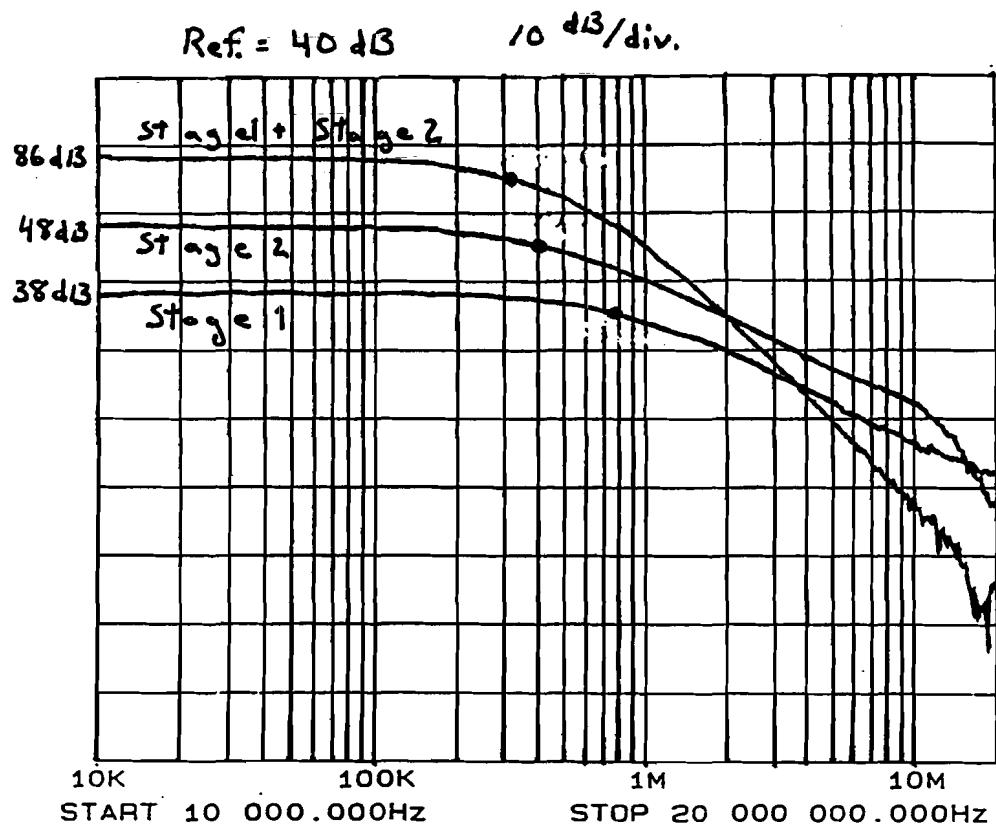
Figure 4.5: Frequency response of preamp.
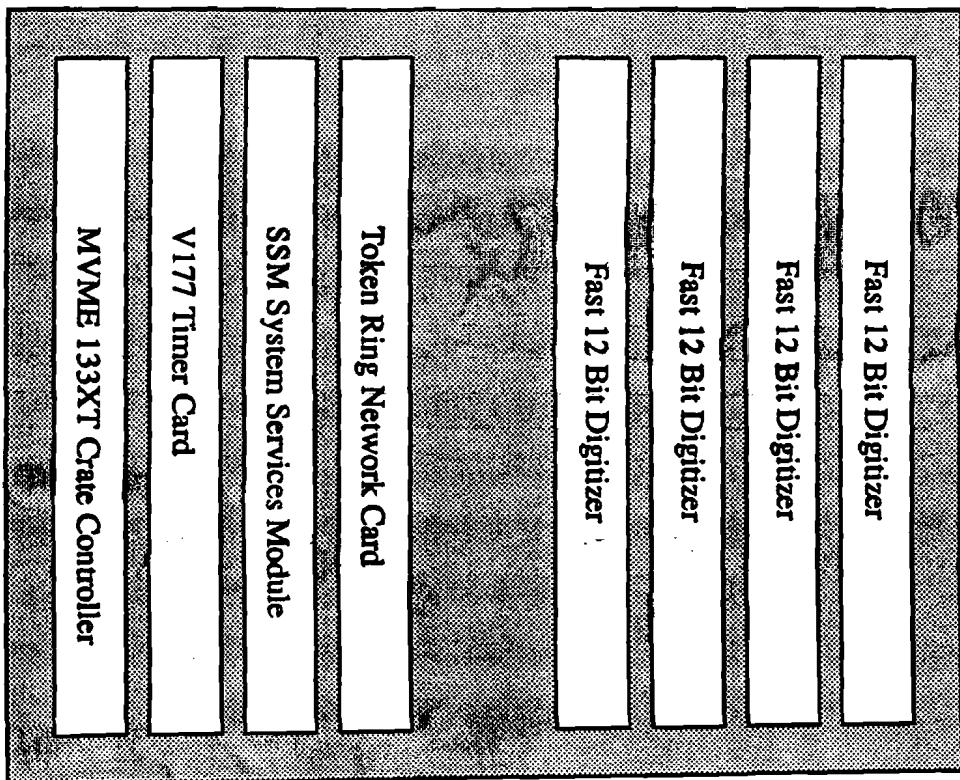
Figure 4.6: VME Electronics.

4.4 VME Electronics

The signal from the preamp is sent over 50 meters of twinax cable through a tunnel penetration to the VME electronics in an equipment gallery above ground. The VME cards consist of eight digitizer cards to record the data, a microprocessor card that acts as crate controller, a Token Ring card for network communications, and a clock decoder card that can decipher the timing events that signal when beam is present and which acceleration cycle is running.

4.4.1 Digitizer Cards

Each ADC has four channels, each of which has 12 bit resolution, a maximum clock rate of 1 MHz, and 128 kbytes memory. The channels are not multiplexed, so each channel digitizes at the full clock speed. These fast ADC's with large memories allow us to record every channel on each of the 20,000 turns in the acceleration cycle so that beam dynamics may be observed on a single turn time scale throughout the cycle. The cards include an internal clock, but for this application they are connected to the low-level rf signal divided by the harmonic number to clock synchronously with the beam. Note that this clock slews from 360 kHz to 630 kHz. An external trigger is provided by the TCLOCK signal from the main accelerator control system.

4.5 Control Software

Besides completing the present experiments, the IPM is intended to be in continous use as a diagnostic for tuning up the Booster performance. Thus it was important that it be integrated into the main control system at Fermilab, known as ACNET.[22] Figure 4.7 shows the graphical input page used to control the IPM. It may be accessed from any control console on site and does not require special knowledge of the IPM operation. Using mouse and keyboard input, one can choose the first turn of data to read, the number of turns to read, and the clock event to trigger on. It takes about 15 seconds after the trigger to move the raw data across the network and process it for graphical display. After the data is gathered, one may view the beam centroid position, second moment, or emittance, plotted vs time. Raw data of single profiles can

```
B77        -1                                                      ◆Pgm_Tools◆
                           Booster Ion Profile Monitor
─────        Beam Width ──────              ───── Plot Data
First Turn to Read  :   ████████           Plot Emittance
Turns to Read       :   ████████           Plot Beam Width
Turns to Skip       :   ████████           Plot Beam Position
ADC Status          :   OP█                Plot Beam Charge
Select Event: <1▐, ▐▐, ▐▐, ▐▐>             One Profile
Plot Data                                  Set Plot Limits
Write File to Disk
Read File from Disk                        ── Cursor Readout
Copy to local disk                         X Value: -1
                                           Y Value: -1


VME Diag.  ·
ADC Cards  |


                          - Messages
05-JAN-93 11:36:48 Continue.
05-JAN-93 11:36:42  WAIT: Building a directory.
```

Figure 4.7: Graphical control panel to operate IPM.
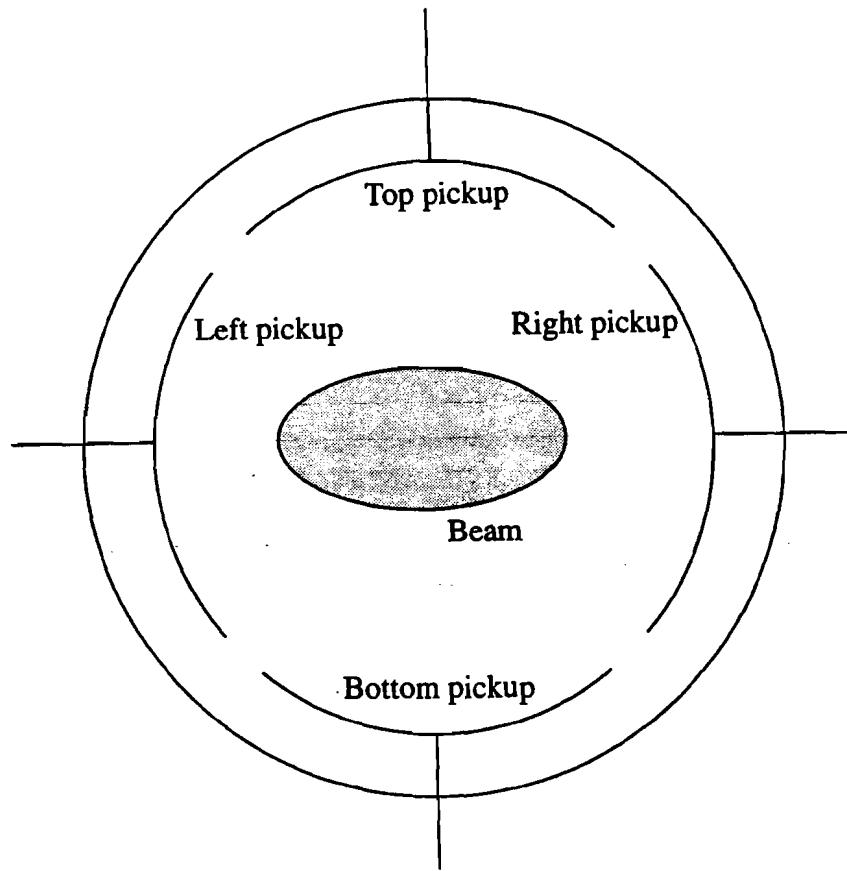
Figure 4.8: Beam Position Monitor.

also be viewed. The program also will save files to disk or read and display previously saved files.

4.6   Other Devices

In the course of the experiments it was necessary to use several other devices for various measurements. This section offers a brief description of each device and its purpose. The literature in Reference 23 offer more complete information.
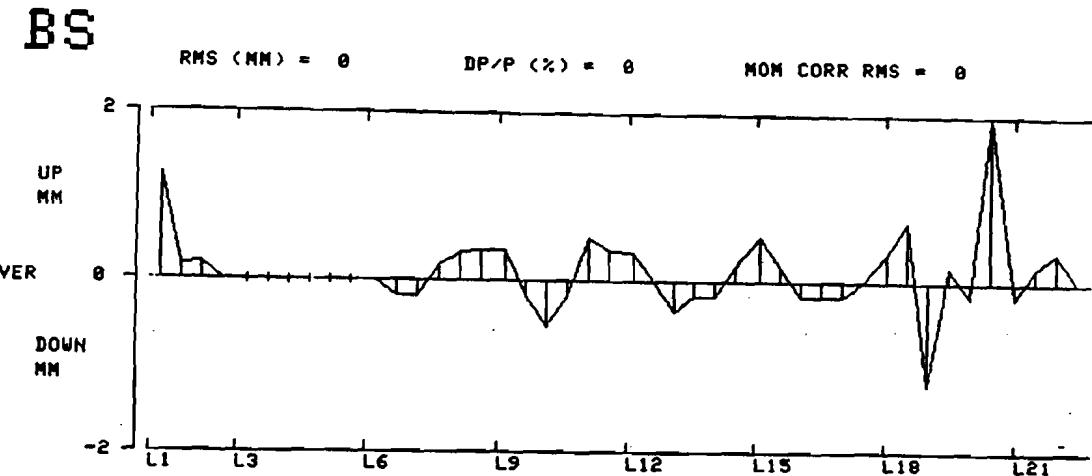
Figure 4.9: BPM signal.

Beam Position Monitor

The most basic and common piece of beam instrumentation is the beam position monitor (BPM). It consists of 4 pickup plates, 2 horizontal and 2 vertical, placed parallel to the beam (Figure 4.8). The difference of the signals from each plate is linearly proportional to the beam offset from center. The BPMs are used to monitor beam position and to look for dipole oscillations such as might be caused by an injection oscillation or instability. Figure 4.9 shows typical output from the BPMs.
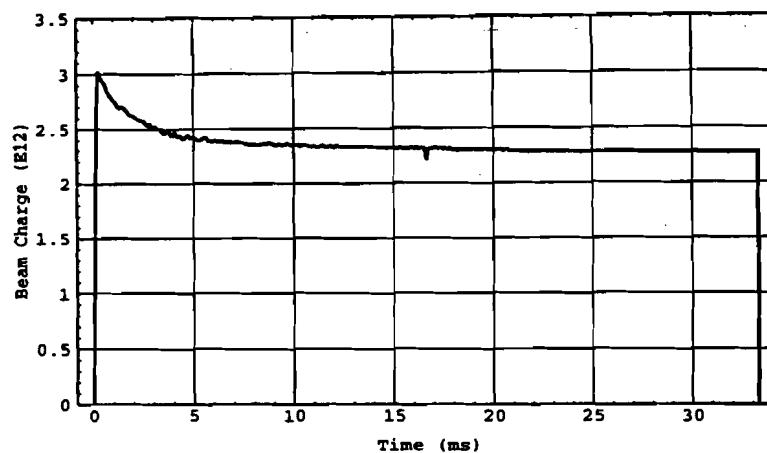
Figure 4.10: Beam intensity signal.

Beam Charge Monitor

The intensity monitor measures the amount of charge in the ring at any time. It is a toroid of ferrite surrounding the beam pipe that is wound with wire that acts as the secondary of a transformer, where the beam is the single turn primary. Figure 4.10 shows a typical signal from this instrument.

Abs-Mean=1.3 mm   Sigma=2.1 mm   ChiSq=4.5
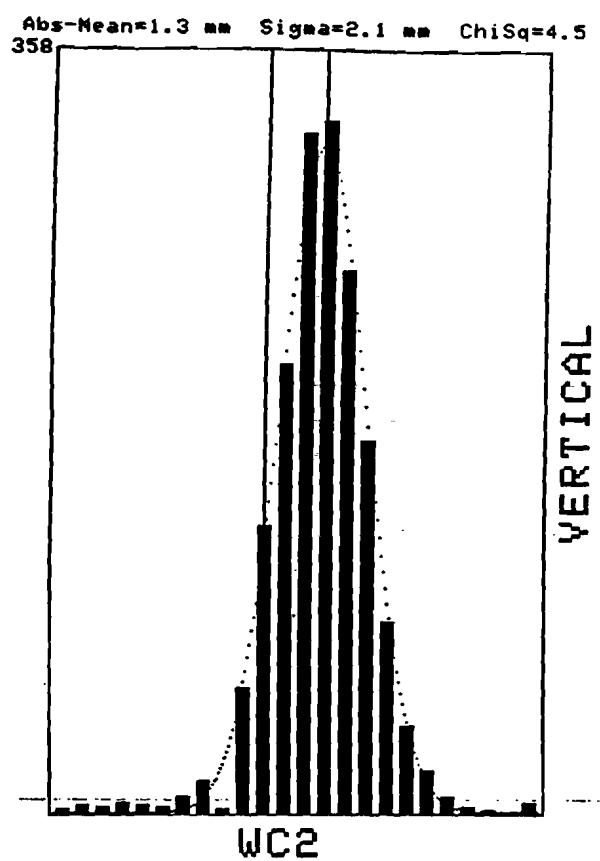
Figure 4.11: Beam profile measured by multiwire.

Multiwire Profile Monitor

The multiwire profile monitors are in the injection and extraction lines of the Booster. They provide independent measures of the beam width and emittance as a check on the IPM. Figure 4.11 shows a profile measured with the extraction line multiwire, and Figure 4.12 shows a sketch of the device. When beam strikes the individual wires, secondary electrons create a current in the wires which is amplified to produce the profile.
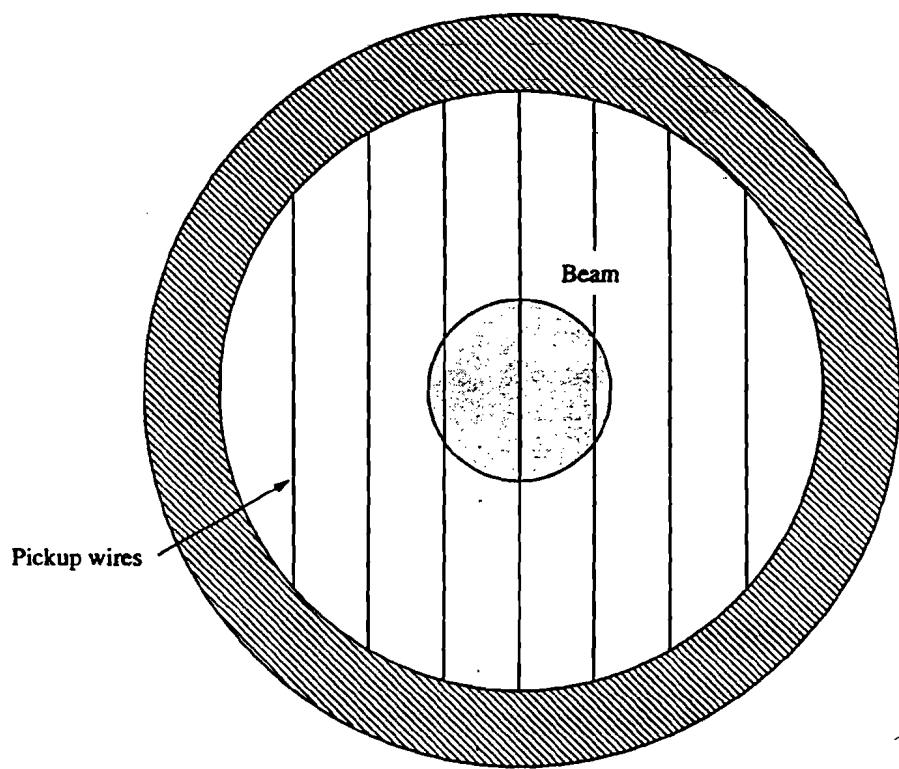
Figure 4.12: Multiwire profile monitor.

1.30V

200 mV/div

-700mV

5 ms/div
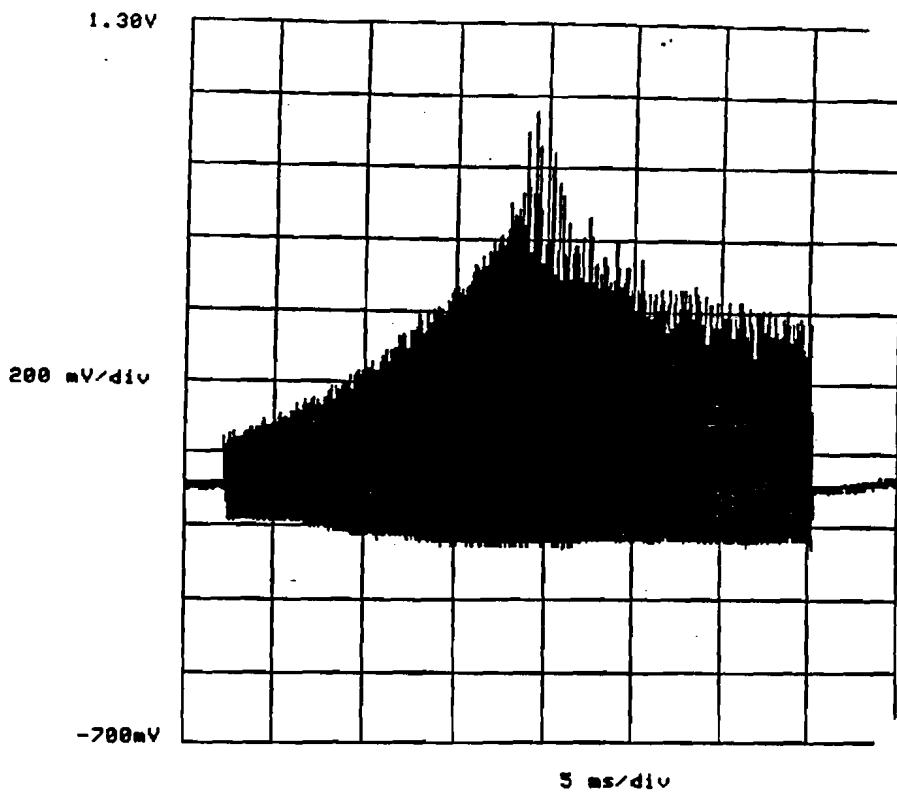
Figure 4.13: Signal from resistive wall monitor.

Bunch Length Monitor

A relative change in bunch length can be found by measuring the peak current in each bunch with a resistive wall monitor, then dividing by the revolution frequency. For a given amount of charge, the peak current is inversely proportional to the bunch length. The resistive wall monitor is made by cutting a gap in the beam pipe and placing 50Ω resistors around its periphery. The beam image currents flow through each resistor creating a voltage drop. If one of the resistors is then replaced with a transmission line leading to an oscilloscope the instantaneous beam current can be measured. This diagnostic is useful when looking at phenomena around the transition energy where the bunch length is subject to large changes.

Chapter 5

IPM Error Analysis

The profiles measured by the IPM are subject to errors caused by several factors. The ions must drift on straight paths from their point of creation to the microchannel plate (MCP). Collisions with other ions or errors in the clearing field may modify their path. There are also statistical errors arising from channel-to-channel variations in signal and from cycle-to-cycle variations in the Booster beam. The fitting function chosen must also be appropriate for the data. In this chapter we analyse the magnitude of these errors and examine the accuracy of the fitting function used.

5.1   Ion Collisions

The ions may collide with gas molecules before reaching the MCP, resulting in deflections and loss of resolution. The mean free path between collisions is

$$\lambda = \frac{1}{n\sigma},$$

where n is the residual gas density and σ is the collision cross section. For the Booster

$$n = 1.7 \times 10^9 \text{cm}^{-3},$$

$$\sigma \approx 10^{-14} \text{cm}^2.$$

therefore

$$\lambda \approx 6 \times 10^4 \text{cm}.$$

Since the distance to the MCP is much less than this (about 6 cm), collisions are unlikely and are assumed to have no effect on the measured profile.

5.2 Space Charge Distortion

The ions created by the beam must drift in the x-direction only (Figure 5.1). Any motion in the y-direction will cause distortion of the true profile. Although the applied electric field in the IPM is carefully shaped so that the field lines are straight across the beam, the beam's self field is radial, thus it has a y-component (Figure 5.2). The effect of the self field is most pronounced near extraction because the betatron oscillations damp as the beam energy rises (see Equation 2.48), thus the beam is smaller and more dense at high energy. Typical parameters of an intense beam near extraction are $N = 2.5 \times 10^{12}$ and $\sigma = 2.0$ mm. This gives a maximum transverse electric field of 30 V/cm. The applied electric field is 720 V/cm. It is perhaps surprising that the ions are significantly deflected by a transverse field 24 times smaller than the applied field. However, both simulation and experiment clearly show that the measured width depends on the intensity.
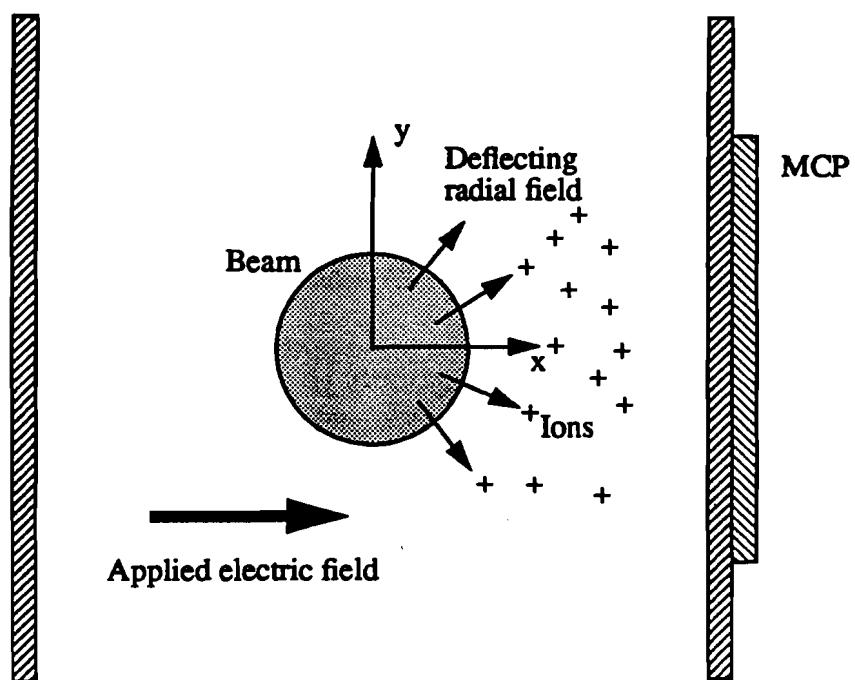
Figure 5.1: Electric fields in the IPM.
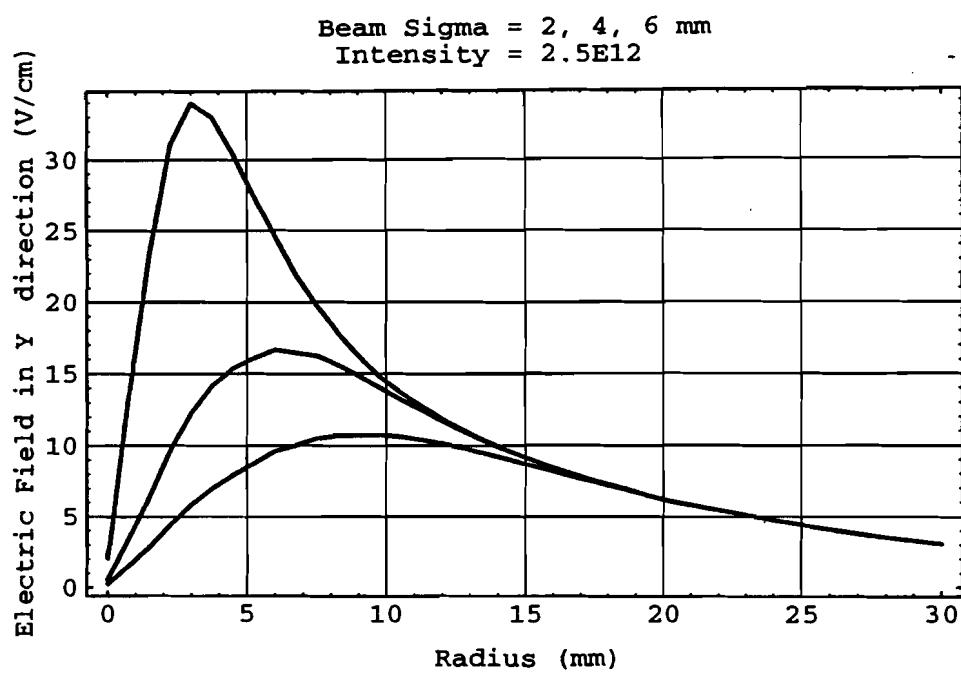
Figure 5.2: Deflecting self-fields for different beam sizes.

5.3 Computer Model of IPM

To investigate the effects of space charge a computer model was constructed using the program TOSCA2D.[24] This is a commercially available program that uses the finite element method to solve Poisson's equation in two dimensions. The model consisted of the proper boundary conditions plus a round gaussian charge distribution to simulate the beam (Figure 5.3). Only the upper $1/2$ plane needs to be modeled because of symmetry. After the fields are found a pseudo-random gaussian distribution of 1000 ion positions is generated using the program Mathematica[25] (Figure 5.4). These ions are then input to TOSCA2D and tracked through the electric fields to the MCP. At the plate the ion positions get binned and fitted with a gaussian curve. This procedure was repeated several times for different beam widths, beam intensities, and clearing field voltages. The beam sizes ranged from 2 mm to 6 mm, and the intensities from 0.5×10^{12} to 3.5×10^{12}. This allowed us to develop a comprehensive numerical description of the errors in the profile under different conditions.

5.3.1 Intensity Dependence

Figure 5.5 shows several profiles at the MCP resulting from simulations of different beam intensities and a fixed beam width of 2 mm. Figures 5.6 and 5.7 show similar data for 4 and 6 mm. As expected, the data for 2 mm shows a large smearing effect because of the intense fields felt by the ions. The 6 mm data shows less effect. An approximate analytic solution for the radial electric

IPM_MODEL.PIC
30/Jun/93 11:37:10   Page 8 : RECO -50 60 0 60 +ERAS

Y [MM]

Component: CHARDEN

0.0   1.66651E-11   3.33303E-11

ELEM=LINE SYMM=XY SOLN=V SCALE=1.0 FIEL=ELEC
Static Solution   Mesh   3896 Elements   166 Regions

VF/PE2D.8
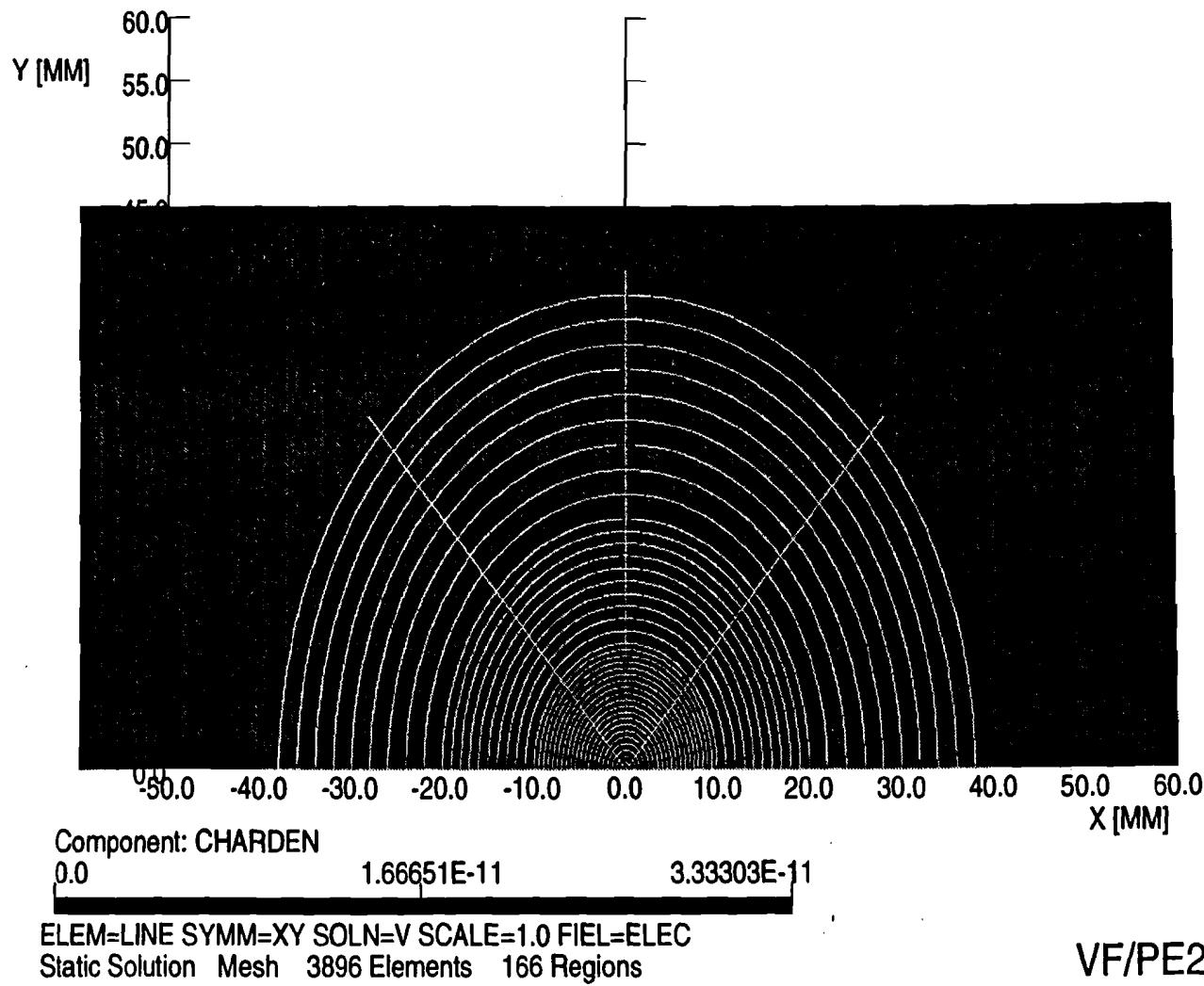
Figure 5.3: TOSCA2D model of IPM.
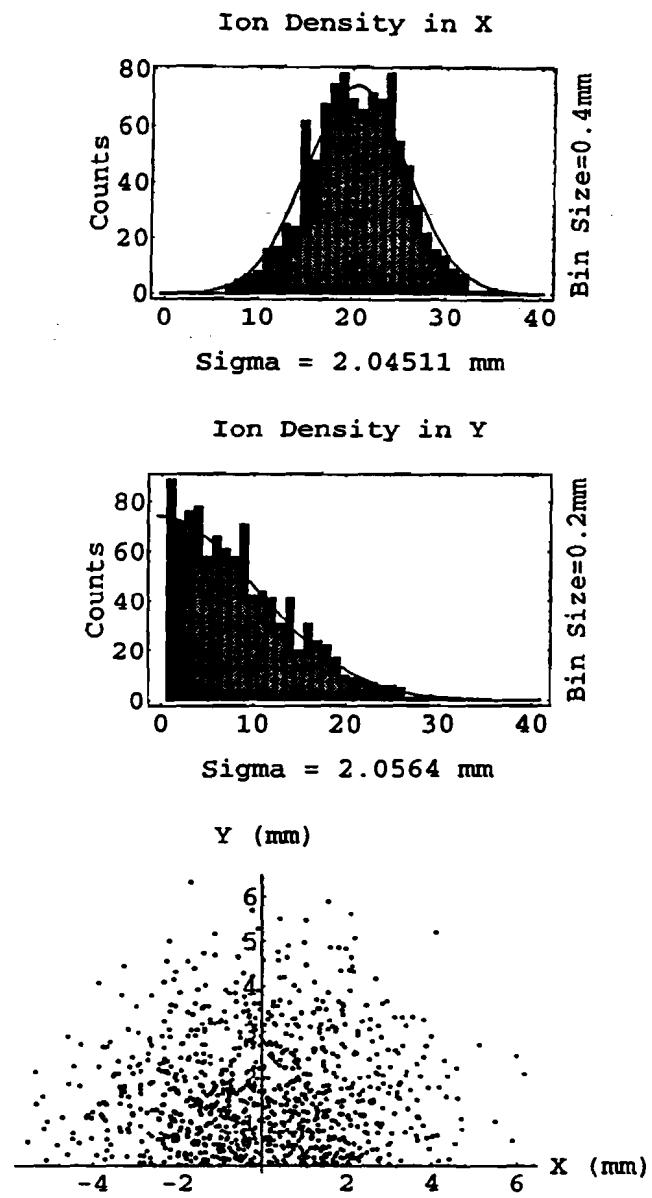
Figure 5.4: Typical ion distribution generated by *Mathematica*.

field is

$$E = \frac{e\lambda}{2\pi\epsilon_0 r}(1 - e^{-r^2/2\sigma^2}),$$

where λ is the line charge density. The electric field is inversely proportional to the *square* of the beam width, so the distorting effects of space charge increase rapidly with decreasing beam size.

To get a complete description of the space charge effects several distributions were generated for each intensity. Figure 5.8 shows the variation in rms beam width *vs* intensity. The error bars represent one standard deviation determined by five separate runs with different initial distributions. Virtually all of the error is due to the variation in the initial distributions.

5.3.2 Statistical Tests of Distributions

We have assumed that the beam maintains a gaussian distribution. The Central Limit Theorem says that the distribution of a large number of particles subject to random, uncorrelated processes will tend to a gaussian. The beam is affected by many random processes (*e.g.* fluctuations in ion source output, magnet errors, power supply noise, vibration) so the assumption that it is gaussian is justified. The χ^2 statistic will be used to test the validity of a gaussian fit. χ^2 is defined as

$$\chi^2 = \sum_i \frac{[f(x) - y_i(x_i)]^2}{\sigma_i^2},$$

where $f(x)$ is the fitting function, $y_i(x_i)$ are the measured points, and σ_i is the error in each point. The reduced χ^2 statistic is defined as

$$\chi^2_\nu = \frac{\chi^2}{\nu},$$
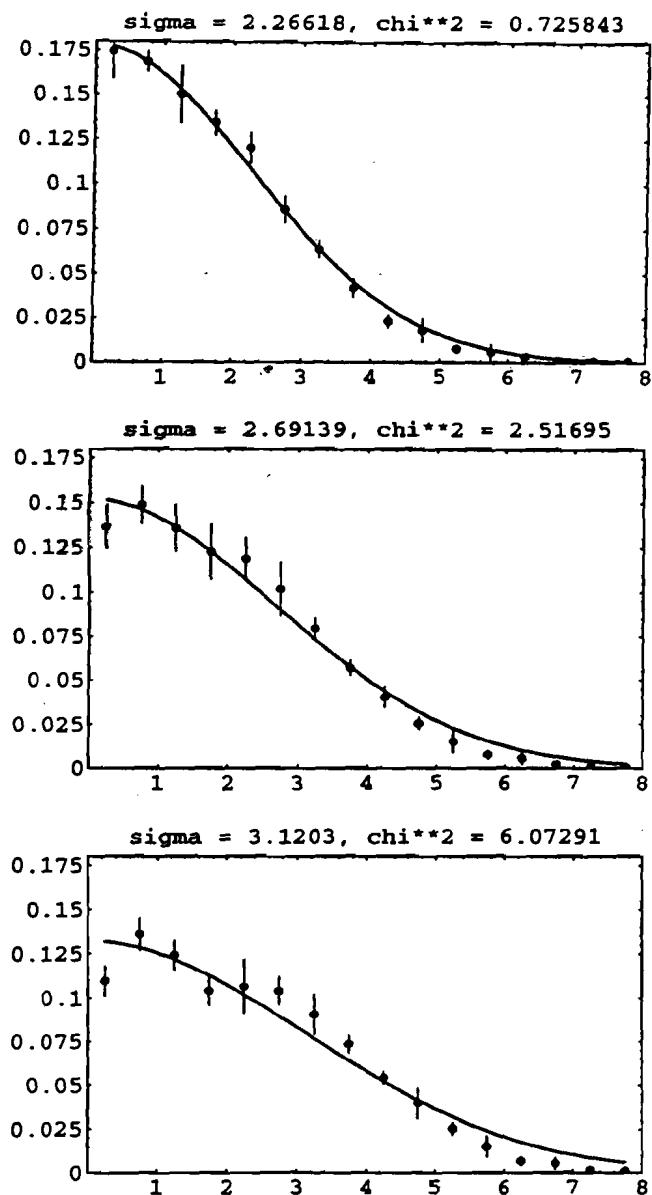
Figure 5.5: Profiles for different beam intensities from TOSCA2D model with fixed initial beam width of 2 mm. X-axis shows vertical position and Y-axis shows normalized signal. Intensities are 0.5×10^{12}, 1.5×10^{12}, and 2.5×10^{12} from top to bottom.
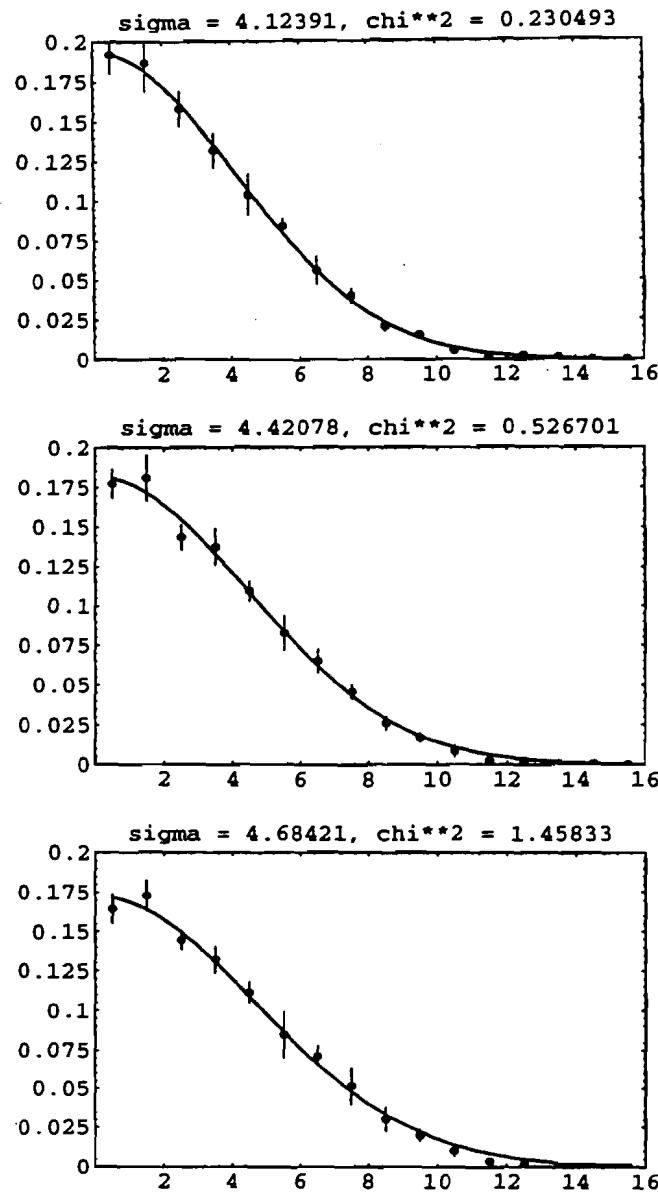
Figure 5.6: Profiles for different beam intensities from TOSCA2D model with fixed initial beam width of 4 mm. X-axis shows vertical position and Y-axis shows normalized signal. Intensities are 0.5×10^{12}, 1.5×10^{12}, and 2.5×10^{12} from top to bottom.

sigma = 6.39037, chi**2 = 0.236732

sigma = 6.5816, chi**2 = 0.293423

sigma = 6.78104, chi**2 = 0.436543
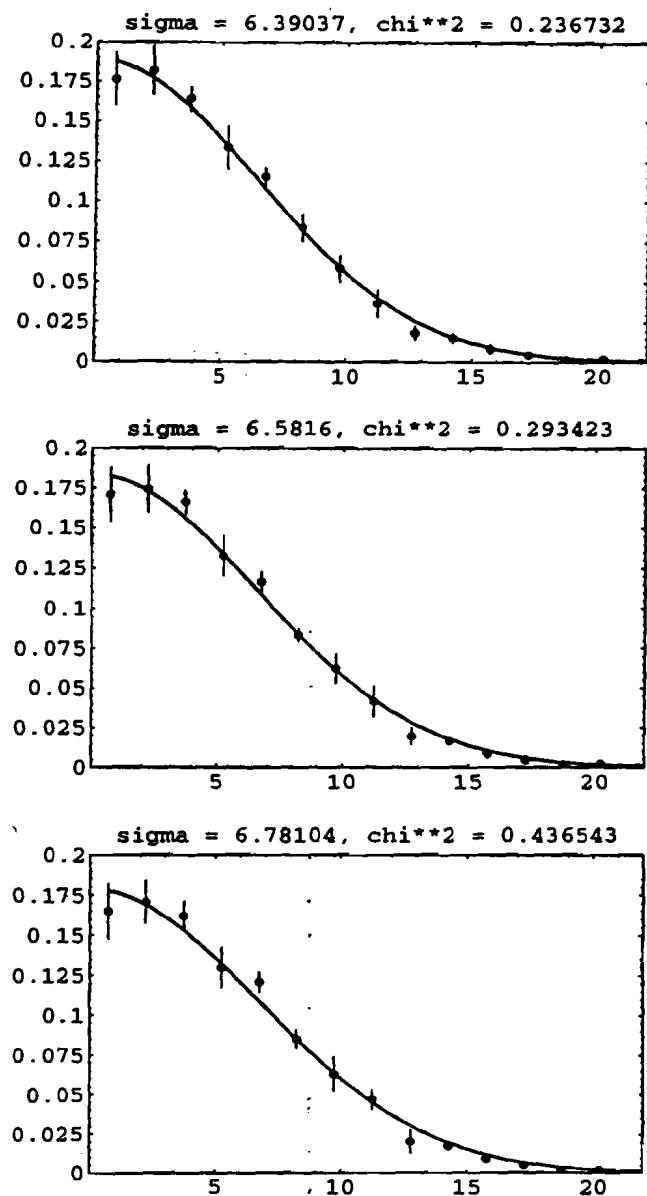
Figure 5.7: Profiles for different beam intensities from TOSCA2D model with fixed initial width of 6 mm. X-axis shows vertical position and Y-axis shows normalized signal. Intensities are 1.5×10^{12}, 2.5×10^{12}, and 3.5×10^{12} from top to bottom.
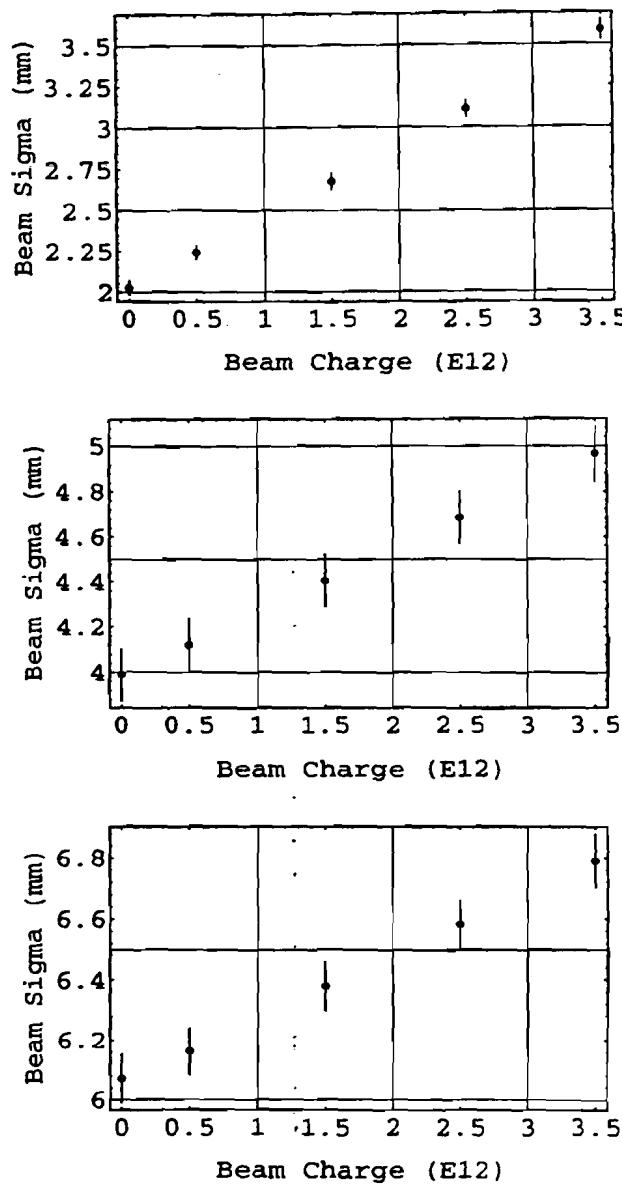
Figure 5.8: Intensity dependence of measured beam width for true widths of 2, 4, and 6 mm.

Table 5.1: χ_ν^2 of simulated beam profiles.

Beam Width	Beam Intensity (E12)			
	0.5	1.5	2.5	3.5
2.0 mm	0.726	2.517	6.073	4.969
4.0 mm	0.230	0.527	1.458	1.783
6.0 mm	0.571	0.237	0.293	0.437

where ν is the degrees of freedom of the measurement. We will use the fitting function

$$f(x) = Ae^{-(x-\bar{x})^2/2\sigma^2},$$

where $\bar{x}$ is the mean position, σ is the beam width, and A is the maximum value of f. This is a 3 parameter fit, and there are 30 channels of data, giving 27 degrees of freedom. Table 5.1 shows χ_ν^2 for several different widths and beam intensities.

At high intensities the space charge distortion will change the beam distribution measured by the IPM to something other than gaussian. Nevertheless, we would like to fit it with a gaussian curve because it's unlikely that another fitting function will yield better results. The computer results will enable us to map from the measured width to the true width because they reproduce the same phenomena that occur in the real detector to distort the beam shape.

5.3.3 Effect of Varying Clearing Field Voltage

Unfortunately the real beam width cannot be independently observed in the Booster except at injection and extraction, so the computer simulations that

vary the beam width and intensity cannot be verified directly through experiment. However, there is one parameter that can be changed in both the computer model and the experiment, and that is the clearing field voltage. For a given intensity, we would expect to measure different widths at the MCP for different applied clearing fields. Figure 5.9 shows different profiles measured with the IPM. For these measurements the intensity was fixed and the clearing field voltage was varied from 4 kV to 8 kV. The profiles shown were taken just before extraction. Figure 5.10 compares TOSCA2D simulation results with the measured data. To create the proper initial distribution for the simulation, the space charge correction was subtracted from the experimental data and a distribution with the resulting width used as input. Then a number of random distributions with 1000 ions each were used to gather statistics about the fit for each different clearing voltage. The χ^2 test is used to check the likelihood that each measured profile is drawn from the same parent distribution as the simulated one. The Q-value of this test is the probability that the observed chi-square should exceed a value χ^2 by chance even if the distributions *are* drawn from the same parent. Small values of this test statistic indicate that it is unlikely that two distributions are derived from the same parent. Thus it provides an indication of whether the true beam is a gaussian that has been distorted by space charge or not. The Q-value is given in Table 5.2 for each of the clearing field voltages.
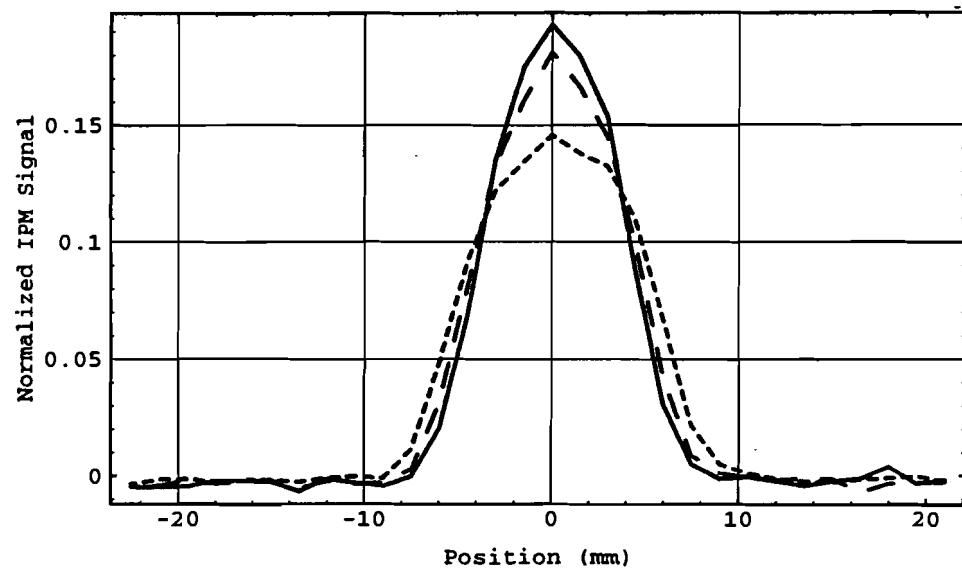
Figure 5.9: Beam profiles taken by IPM for different clearing field voltages.
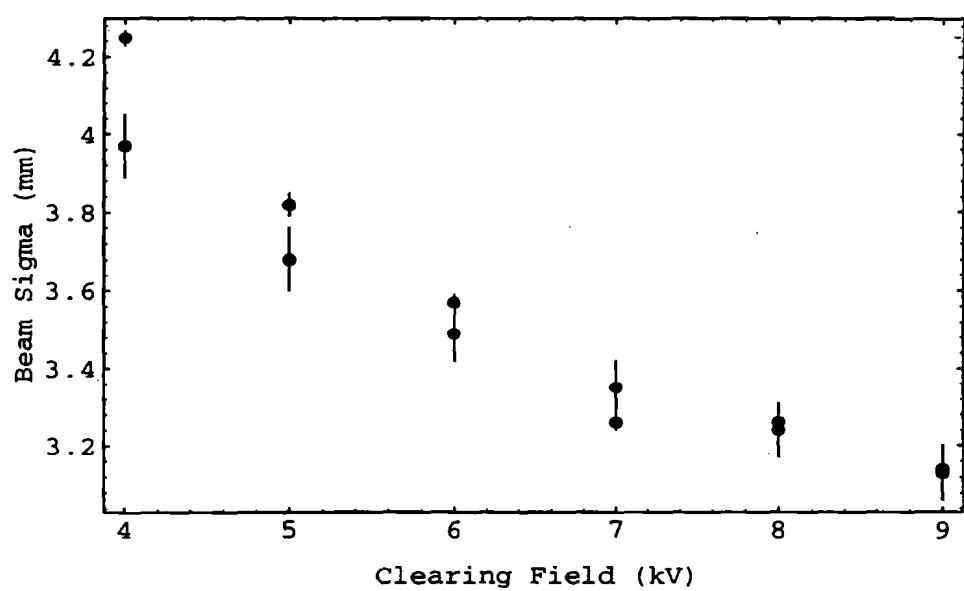
Figure 5.10: Plot of measured beam width and simulated width for different clearing field voltages and fixed intensity.

Table 5.2: Results from χ^2 test comparing experimental and simulated data at different clearing field voltages. Beam intensity = 2.25×10^{12}.

Clearing Field Voltage	χ^2	Q-Value
4.0	2.88	0.564
5.0	3.94	0.558
6.0	2.64	0.756
7.0	2.15	0.828
8.0	1.77	0.879
9.0	3.33	0.649

5.4 Effect of Beam Aspect Ratio

In all of the space charge error calculations it has been assumed that the beam is round. Experiments show that this is not always true. The effect of a changing aspect ratio (horizontal/vertical width) has been calculated analytically in Reference 26. In that work it was found that the measured beam width varies by less than 5% for aspect ratios ranging from 0.5 to 2.0. It is expected to be a small effect because the beam size in the direction orthogonal to the MCP does not directly affect the profile in the plane of interest. Its only impact is to change the beam density, thus the deflecting space charge force on the drift ions.

The horizontal IPM data shows a large beam width oscillation just after the transition energy. Thus the beam density and space charge force are modulated. Figure 5.11 shows the density oscillation near transition. The oscillation is superimposed on a slow linear decrease in beam density marked by the dashed line. Note that when the oscillation is at a maximum, the density is about the same as before transition. A small oscillation in the vertical width

Table 5.3: Space charge correction coefficients and their confidence intervals.

Coefficient	Value	99% Confidence Interval
C_1	-0.3839	(-0.5966, -0.1713)
C_2	1.1093	(1.0592, 1.1594)
C_3	-0.3808	(-0.4396, -0.3220)

is also clearly visible (Figure 5.12) at transition and is assumed to be due to the changing space charge force. The horizontal and vertical data were taken on different days. It's clear that the decay in vertical width oscillations is slower than that for the horizontal data so the estimate of the effects is only approximate. For this measurement, a change in horizontal density of 40% leads to a change in measured vertical width of 6%, a bit larger than the analytical results[26] indicate.

5.4.1 Space Charge Error Correction

Based on the simulations, a two parameter (width and intensity) linear fit was developed to correct the measured rms width to the true value. The correction is given by

$$\sigma_{beam} = C_1 + C_2 \sigma_{measured} + C_3 N.$$

where the constants and their 99% confidence intervals are given in Table 5.3. χ_ν^2 for the fit is 0.995. The mean value of the response for this fit is 2.15 and the standard deviation is 0.09 for an error estimate of 4% due to the computer model.
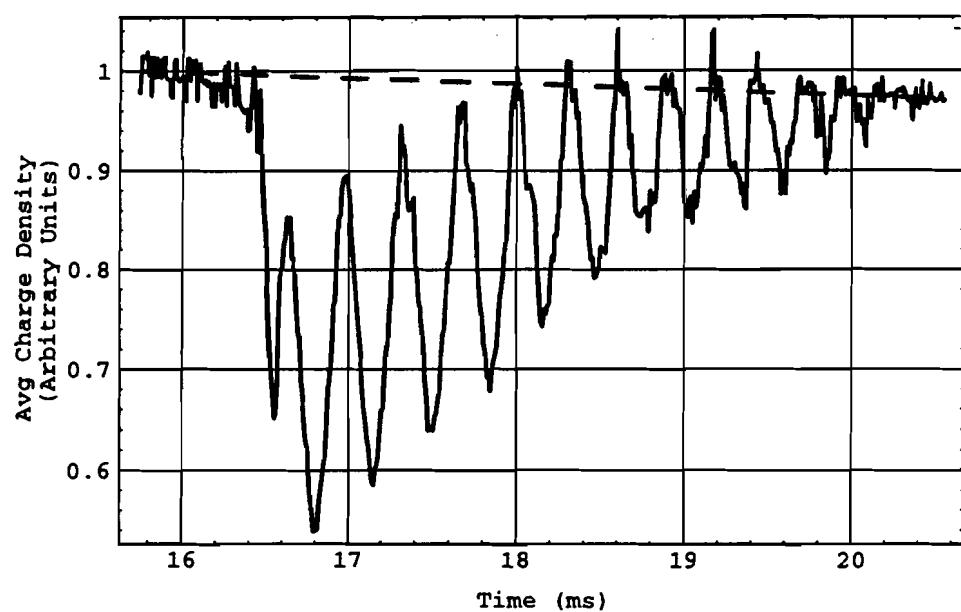
Figure 5.11: Measured horizontal beam density oscillation at transition.
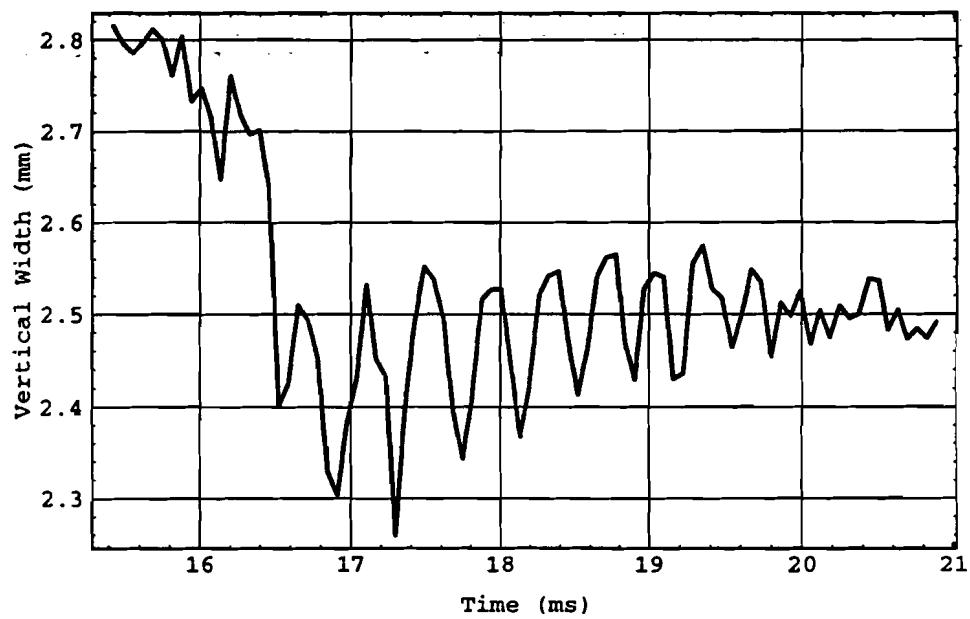
Figure 5.12: Apparent vertical beam width oscillation measured just after transition.

5.5 Possible Improvements in Space Charge Errors

For this first prototype IPM it was necessary to use mostly existing hardware. Improvements might be made in the resolution two ways: apply a transverse magnetic field to confine the drift ions to spiral about the field lines, and/or raise the clearing field voltage. The effects of raising the clearing field voltage were examined with the computer model. Figure 5.13 shows how the measured beam size reduces with increasing voltage. Unfortunately, the improvement is small beyond approximately 10 kV. Large clearing fields will also deflect the beam. An applied magnetic field will confine the ions to oscillate about the field lines at their cyclotron radii. To improve the resolution of the detector the radii should be less than the deflection caused by space charge, which is about 3 mm maximum. The equation of cyclotron motion is

$$B\rho = \frac{p_t}{e}$$

where B is the applied field, ρ is the bend radius, and p_t is the ion's transverse momentum. For the worst case, near extraction

$$p_t \approx 2.0 \times 10^{-22} \text{kg} \cdot \text{m/s}, \tag{5.1}$$

$$B = 0.4\text{T}. \tag{5.2}$$

A 4000 gauss DC field is not practical for a device with a 12 cm gap, so a transverse magnetic field will have limited effect unless the gap is made smaller.

True Beam Sigma = 2.44 mm
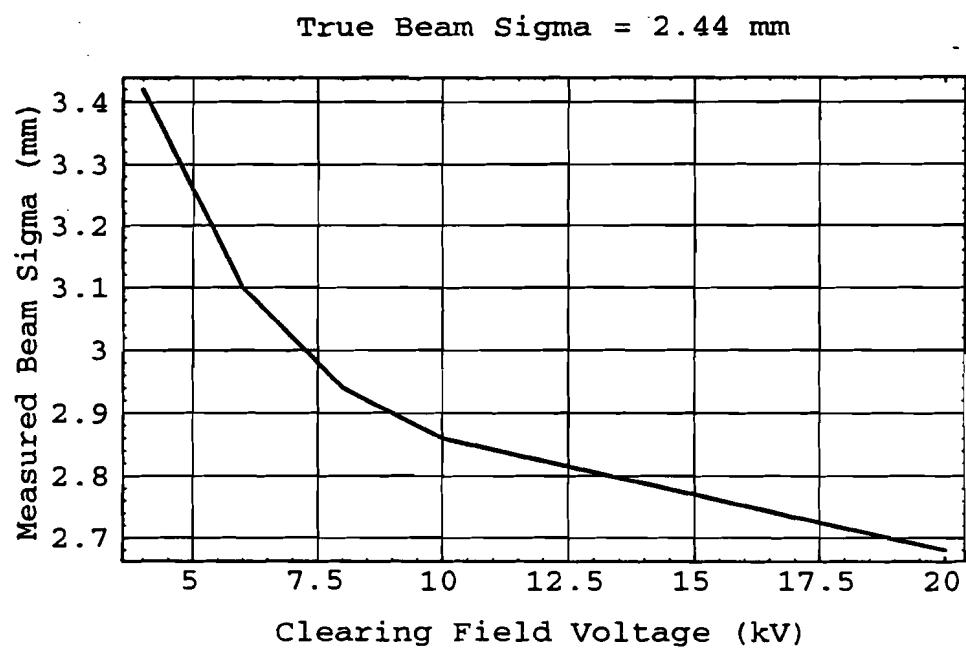
Figure 5.13: Simulation of effect of raising the clearing field voltage.

Table 5.4: Contributions to error in beam width measurement.

Source of Error	Error
space charge correction	4%
beam aspect ratio	5%
channel-to-channel variations	< 1%
measurement fluctuations	2%

5.6 Total Error Estimate

The primary causes of error have been shown to be due to space charge deflections of the ion trajectories, and inaccuracy in the calculated correction due to a beam that isn't round. Additional sources of error are the channel-to-channel variations in the electronics and the statistical fluctuations in the beam width. Table 5.4 summarizes the contributions of each to the total measurement accuracy. The total measurement error is found by adding the individual contributions in quadrature. This error is 7% in the worst case. For larger beams or lower intensities the error will be smaller.

Chapter 6

Measurements at Injection

The emittance is observed to increase throughout the acceleration cycle, with particularly fast growth at injection and at the transition energy. This chapter presents results and analysis near injection.

The calculation of the rate of emittance growth at injection is complicated by beam losses. Obviously, one cannot measure a beam profile larger than the beam pipe. However, the emittance is indeed increasing even if the beam width isn't; the increase is manifested as losses instead. The following section describes a model for determining what the beam width would be if the pipe weren't present. This is used to get the true emittance growth rate. Note that this loss correction is only used to find the initial growth rate, and will not be used in later calculations to change the value of the measured emittance. The experimental results at injection are then presented and compared to previous work.

6.1 Effect of Aperture Restriction

Figure 6.1 shows a measurement of the Booster aperture at a point in the ring where large losses indicate the aperture is a minimum. The data shows beam

5-JAN-1993 11:31
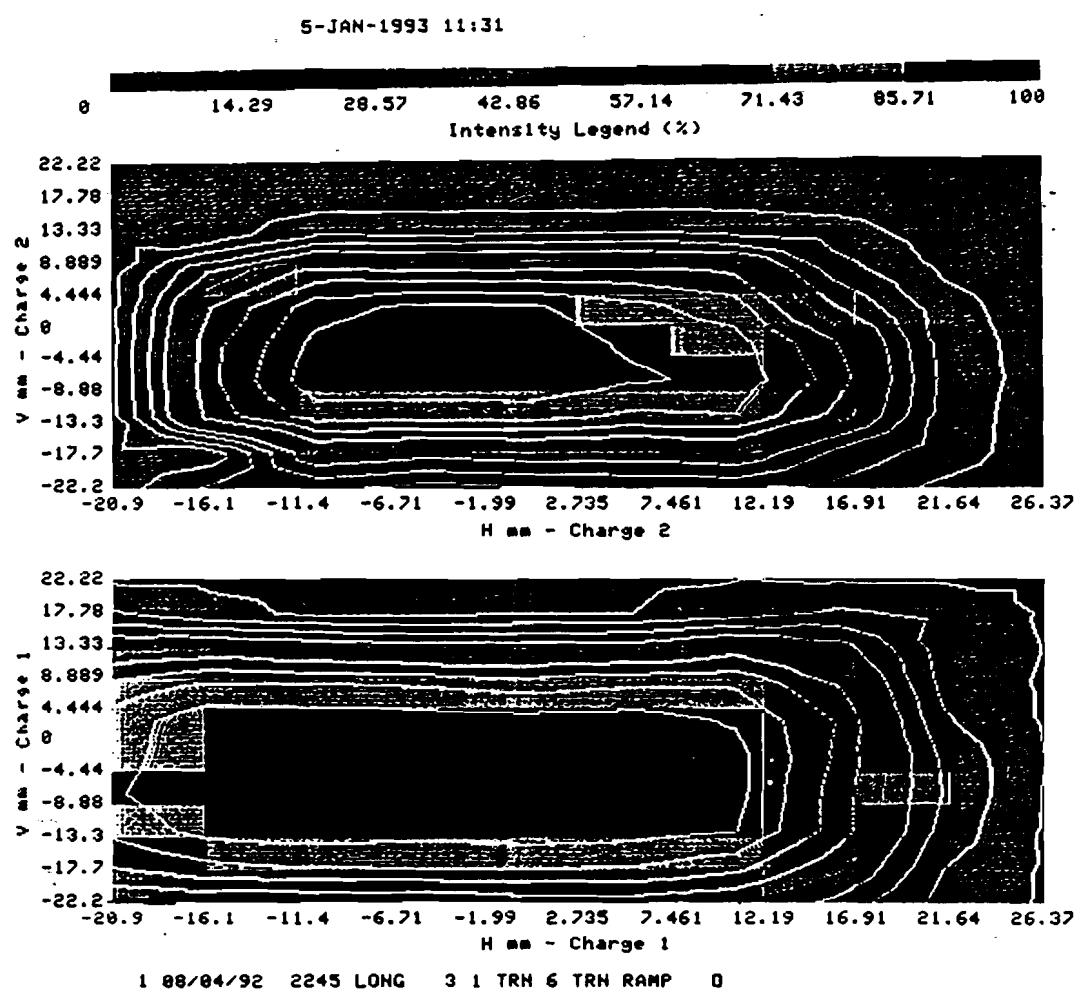
Figure 6.1: Booster aperture at extraction girder.
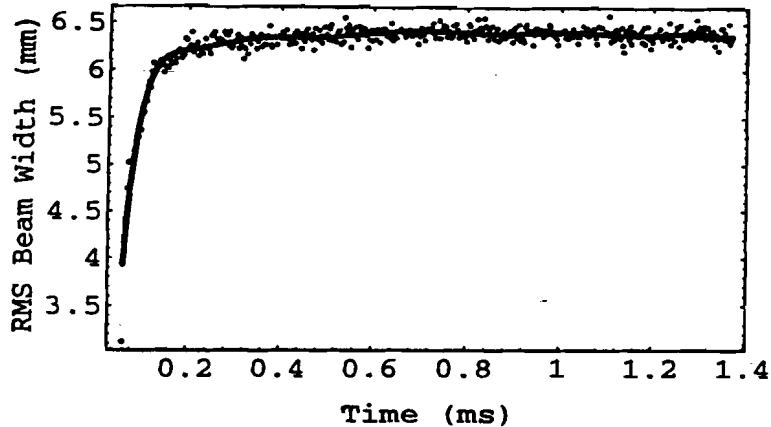
Figure 6.2: Beam size at injection is limited by vertical aperture.

intensity vs position in the pipe, and was taken by creating a very small pencil beam and locally bumping its position until the intensity dropped. Although the design vertical aperture in the Booster is 40 π mm-mrad, these measurements indicate a true aperture of only about 10 π mm-mrad. Furthermore, as shown by Figure 6.2, the measured rms vertical beam size at injection grows to 6.3 mm, then remains flat due to the restricted aperture. This beam size corresponds to an unnormalized emittance of 12 π mm-mrad, in agreement with the aperture scans.

A simple model gives an approximate account of the emittance increase measured as beam loss. The line charge density of the beam is

$$\lambda = \frac{N}{2\pi R},$$

(6.1)

where N is the total charge, and R is the ring radius. Then if the beam is

gaussian in x and y, its volume density is

$$\rho(x,y) = A \exp\left(-\frac{(x-\bar{x})^2}{2\sigma_x^2}\right) \exp\left(-\frac{(y-\bar{y})^2}{2\sigma_y^2}\right). \qquad (6.2)$$

where the constant A is found by integrating ρ over the transverse dimensions and equating it to λ,

$$\lambda = \int \int \rho(x,y)\, dx\, dy$$
$$= A(2\pi\sigma_x\sigma_y). \qquad (6.3)$$

In estimating the real emittance growth rate based on the losses we will assume that all beam losses are due to scraping caused by an increase in vertical beam size. This is only an approximation because other factors such as the capture of the beam into rf buckets also account for some of the losses. Our calculation should be considered an upper bound on the vertical emittance growth rate.

Assuming that the horizontal aperture is adequate, any change in λ is directly proportional (but of opposite sign) to a change in the rms vertical width, σ_y.

$$\frac{\Delta\sigma_y}{\sigma_y} = -\frac{\Delta\lambda}{\lambda}. \qquad (6.4)$$

We have an independent measure of λ from the charge monitor which will be used to correct the measured σ_y. Figure 6.3 shows the difference in normalized emittance before and after the correction, as well as the beam charge. This data is for high intensity (6 turns of beam injected). This correction to the emittance growth rate due to beam losses on the walls will be included in all of our future calculations.

One might ask whether the beam profile remains gaussian during the period of losses, because the scraping may alter the shape. Figure 6.4 shows profiles
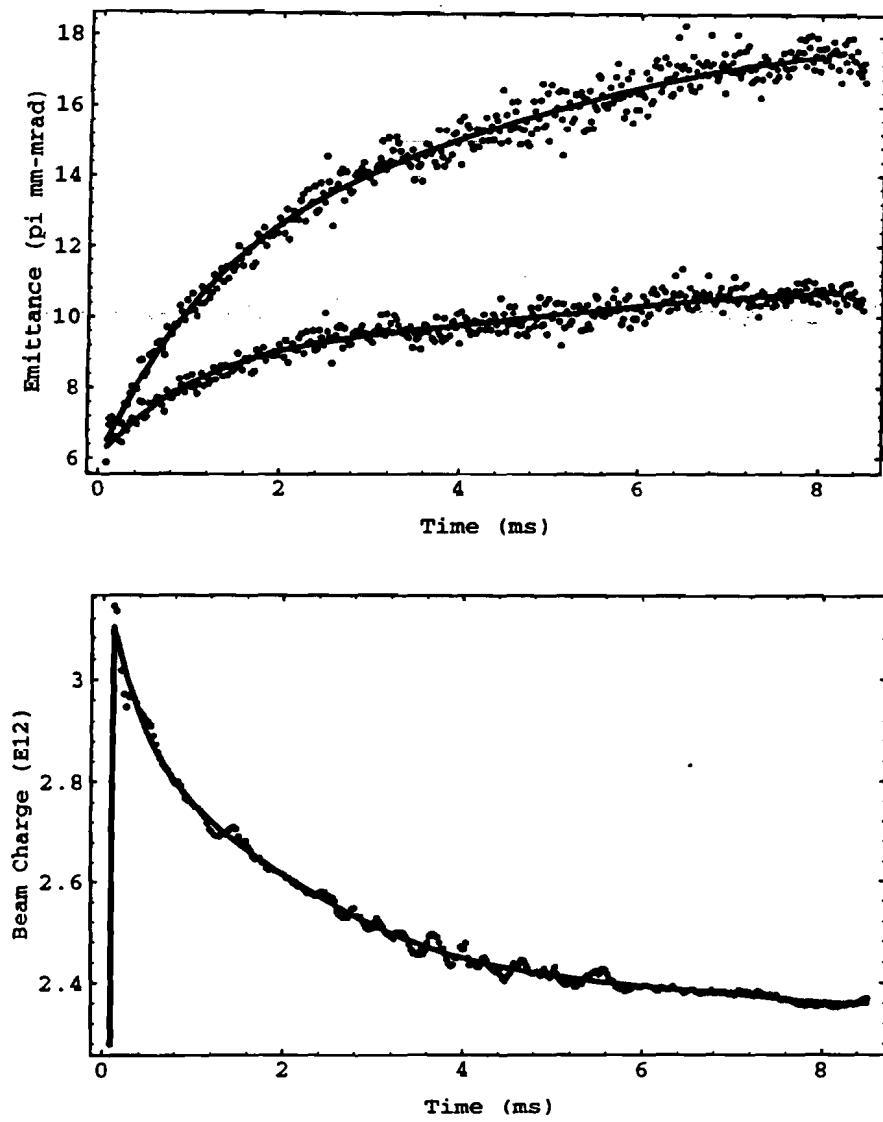
Figure 6.3: Top: Emittance at injection before and after correction for aperture restriction. Bottom: Beam charge.

of the beam taken just at injection, 2 ms later, and finally 5 ms after injection where there are no more losses. This data shows that even though the beam scrapes, the profiles remain gaussian in shape.

6.2 Experimental Results

6.2.1 Previous Work

At the inception of this experiment it was expected that all of the emittance growth occurs very early in the cycle due to the space charge tune shift onto the 1/2 integer resonance line. This is because at the low injection energy of 200 MeV, space charge forces are still strong within a bunch. Previous experiments[5] indicated the growth occurs in the first 5 ms, but that set of data suffered from uncertain time resolution. Previous computer simulations[1] predicted that the emittance growth occurs within the first 0.8 ms. The pattern of emittance growth in these computer simulations closely followed the rf voltage curve which ramped up in 600 μs in the simulation. A plausible explanation for the simulation predictions is that the space charge forces increase as the rf voltage bunches the beam, causing emittance growth. Figure 6.5 shows the rf curve used in the simulations and Figure 6.6 shows the simulated emittance for several beam intensities. Note that the emittance in the figure is total (horizontal + vertical) emittance. However, one wouldn't expect the growth to stop when bunching is finished. It is at this time that the space-charge forces are greatest, so that emittance growth will continue unabated unless there is a loss in intensity due to scraping, or the beam gains enough energy that space-charge forces are significantly reduced. Both of these phenomena
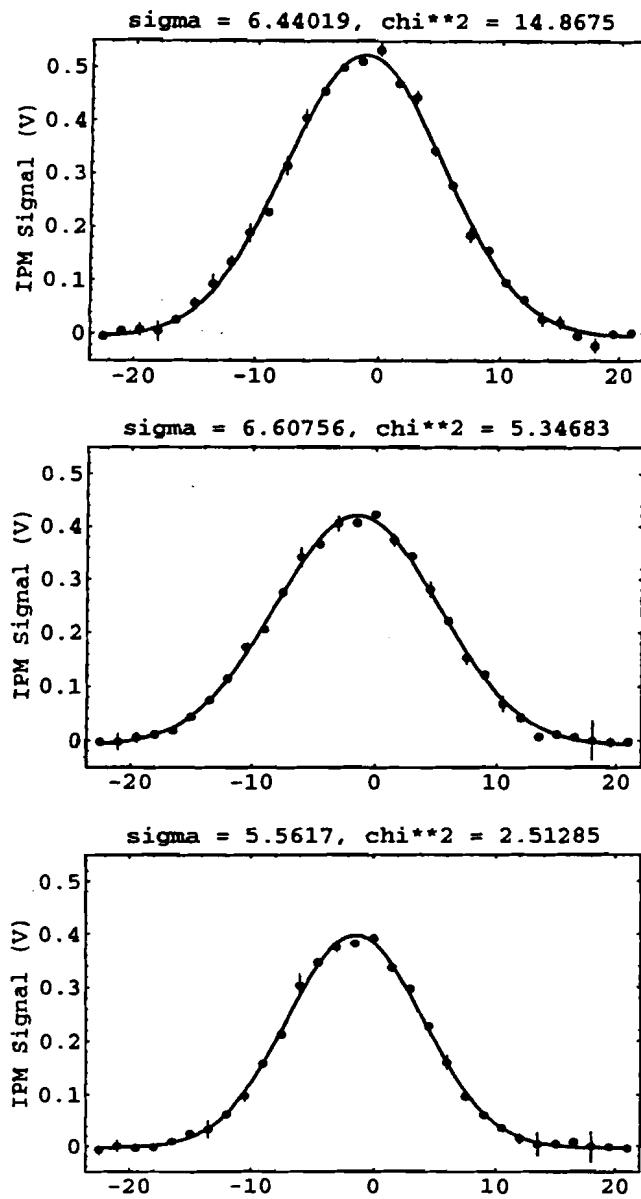
Figure 6.4: Vertical beam profiles from same data as RMS widths. Top profile is at injection, middle is 2 ms later, and bottom is 5 ms after injection.
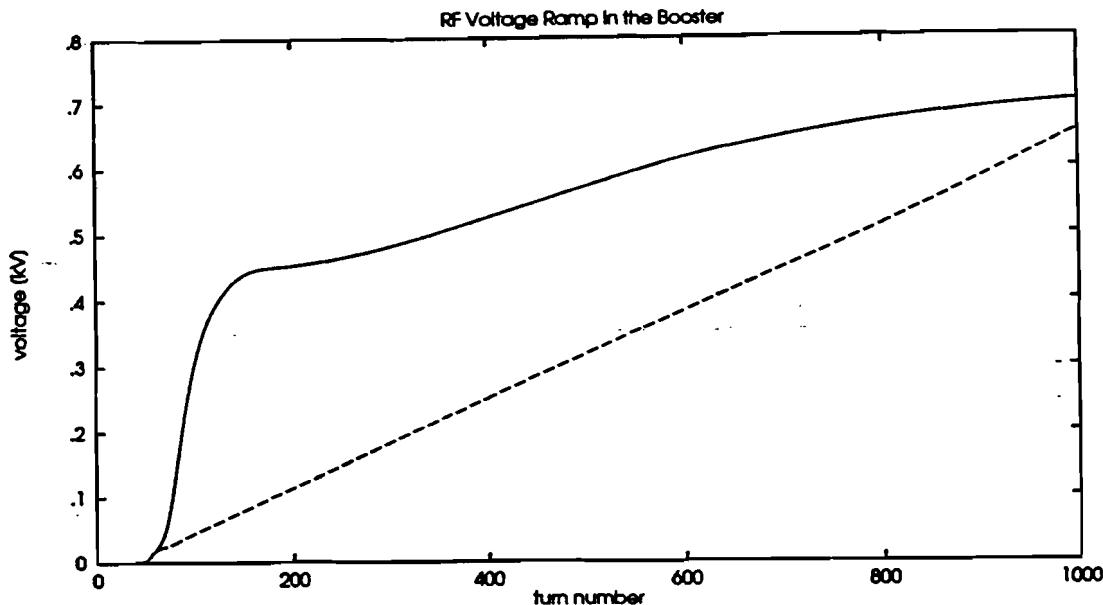
Figure 6.5: RF voltage ramp used in simulations (from Reference 1).

take at least several milliseconds.

We will show below that results from the IPM experiments do not completely support the previous work. Emittance growth is observed at injection, and in particular during rf bunching. However, this is only a small fraction of the total growth.

6.2.2 Effect of RF Bunching

At injection, there is indeed fast emittance growth associated with the rf bunching of the beam. As shown in Figure 6.7, the measured rf ramp has a duration of about 150 μs. Figure 6.8 shows the emittance increase during
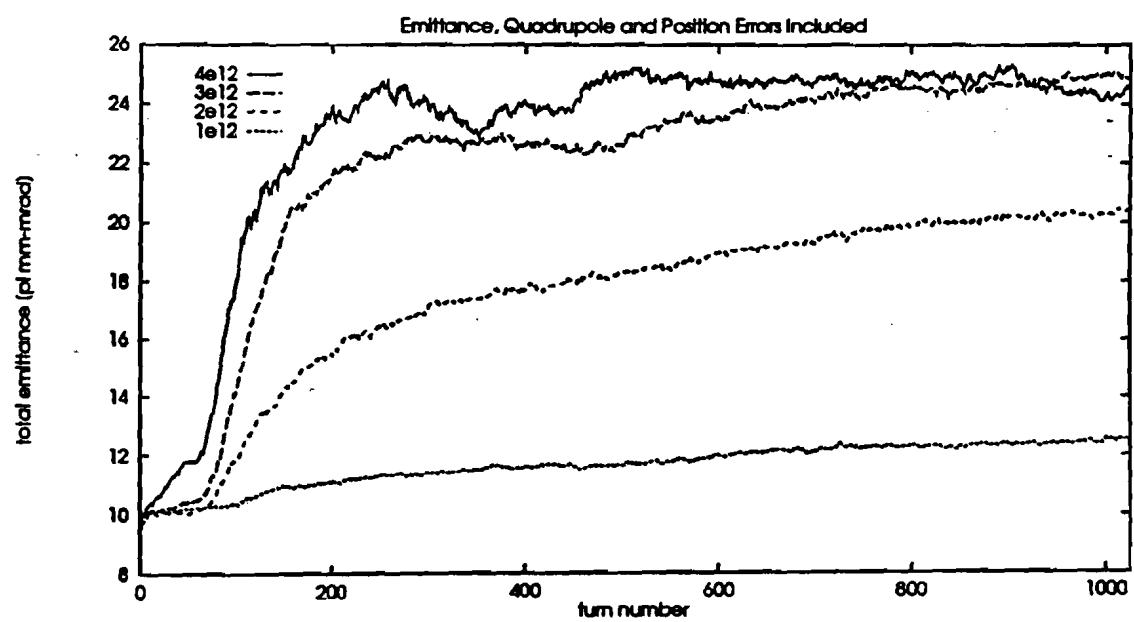
Figure 6.6: Simulation results of emittance growth showing total transverse emittance (from Reference 1).
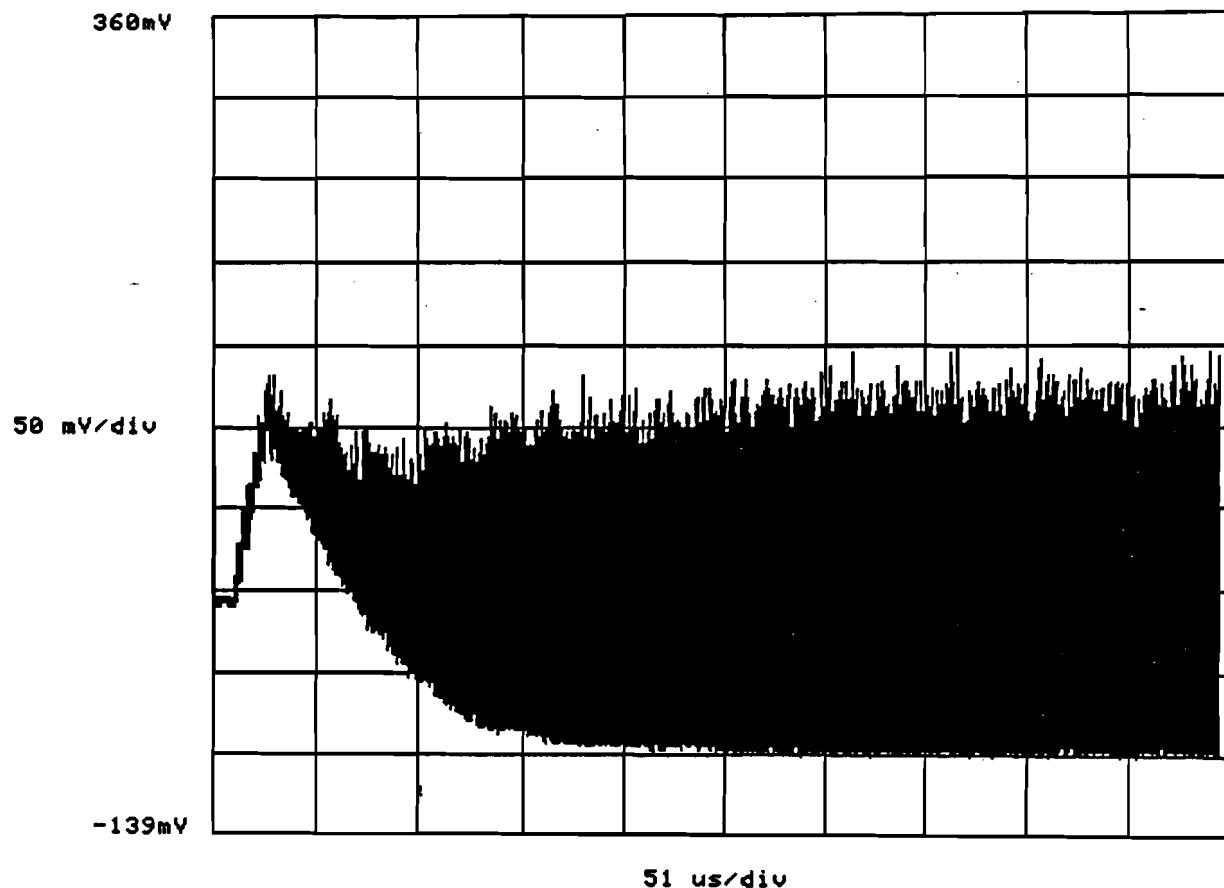
Figure 6.7: Bunch intensity signal from Resistive Wall Monitor. Six steps of beam injected can be seen at left side, followed by bunching caused by rf voltage turn-on. Bunching is complete after $\sim 150\mu$s.
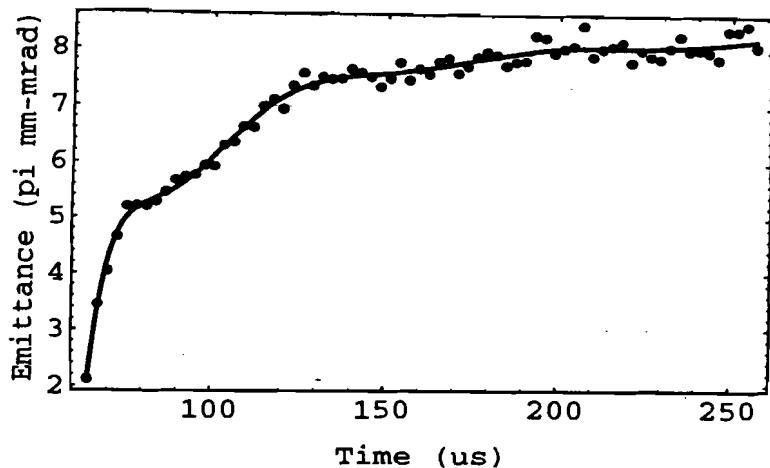
Figure 6.8: Emittance during rf bunching of beam.

this same time for 6 turns of beam injected. The initial very fast growth (first 6 turns) is just the subsequent turns of injected beam being laid on top of each other. If each injected turn was laid perfectly on top of the existing beam there would be little emittance growth as more turns were added. However, the high intensity caused by this would increase the space-charge driven growth. The best performance is obtained when the beam aperture is "painted" by creating a transverse injection mismatch, thus producing a broader beam. Figure 6.9 shows the emittance for the first 20 turns. The first 6 points are again the initial turns whose fitted profiles are shown in Figure 6.10. After the growth during injection there is a brief pause and then the rf bunching begins. Its effect can be seen for the next 150 μs. This growth accounts for an emittance increase from 5.2 to 7.5 π mm-mrad, which is only about 20% of the total
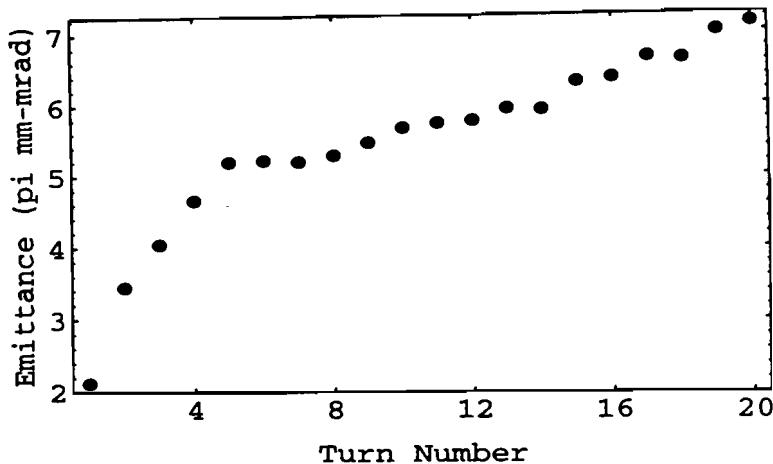
Figure 6.9: Emittance during first 20 turns after injection.

growth through the cycle.

For 6 turns injected, the emittance growth rate during bunching is 0.18 π mm-mrad/turn. The high intensity and low energy cause a large detuning due to space charge. The space charge tune shift from Equation 3.33,

$$\Delta \nu_{sc} = -\frac{3r_0 NB}{2\gamma^2 \beta \epsilon_N},$$ (6.5)

is plotted in Figure 6.11. For this data the bare tune is 6.78, so the spread of tunes within the beam crosses not only the 1/2 integer, but also the integer resonance during rf bunching. This accounts for the large losses at the earliest times. It is surprising that the entire beam is not lost if the intense core of it is crossing the integer resonance. As explained in Section 3.3.1 this relatively small loss is probably due to the amplitude dependence of the space charge tune shift. It should be noted that the time resolution of the beam charge
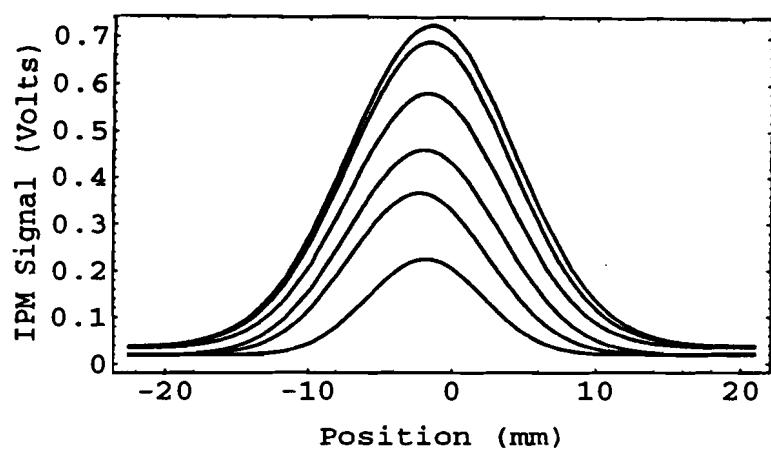
Figure 6.10: Curves fitted to measured profiles of first 6 turns injected show increasing beam intensity.
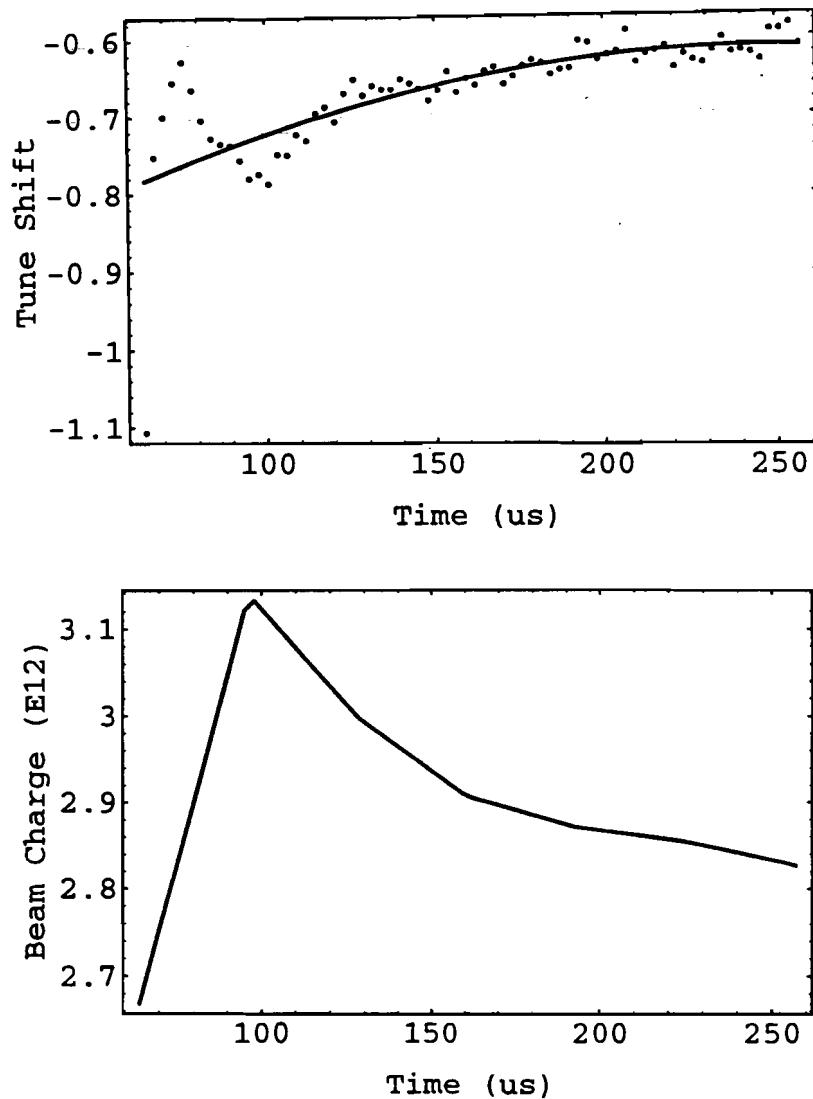
Figure 6.11: Space charge tune shift and beam charge during bunching for 6 turns of beam injected.

monitor is $30\mu s$ (10 turns), which also determines the time-accuracy of the tune-shift calculation. Figure 6.11 shows increasing beam charge for $100\mu s$, but the charge is actually at its maximum within $20\mu s$. This means that the tune shift is actually greater than our calculation at the earliest times. At approximately the same time that bunching is finished, the tune shift is reduced enough that the beam no longer crosses the $\nu = 6$ resonance.

The emittance at the beginning of the cycle for low intensity (1 turn injected, Figure 6.12) does not increase during bunching as does the high intensity case. The tune shift due to space charge is small enough that the tune is almost immediately off the 1/2 integer resonance line.

6.2.3   Measurements at Different Intensities

We turn now from examining phenomena during the first few hundred microseconds to the period of several milliseconds after injection during which most of the beam losses occur. The emittance growth, beam losses, and calculated tune shifts are shown in Figures 6.13 through 6.18.

Table 6.1 gives the coherent tunes for each intensity, found by taking the Fourier transform of the beam centroid position. By subtracting the space charge tune shift from the coherent tune we get a measure of the spread of tunes within the beam (Figures 6.19 and 6.20). Note that the space-charge shifted tunes for high intensity (4,5, or 6 turns) are indistinguishable from one another. This indicates that there is a maximum phase space density N/ϵ that can be supported.

The measured emittance growth rates are given in Table 6.2 for different intensities. Note that even though the phase space densities are the same for
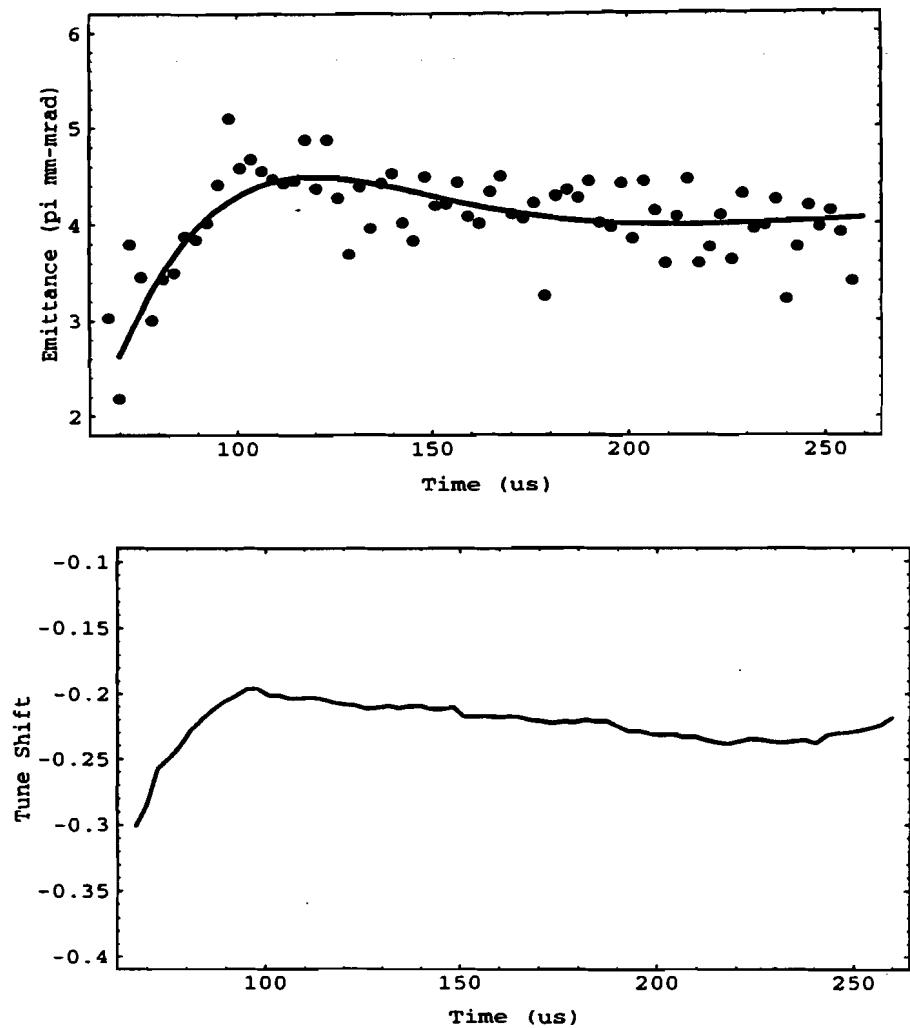
Figure 6.12: Emittance and space charge tune shift for 1 turn of beam injected.
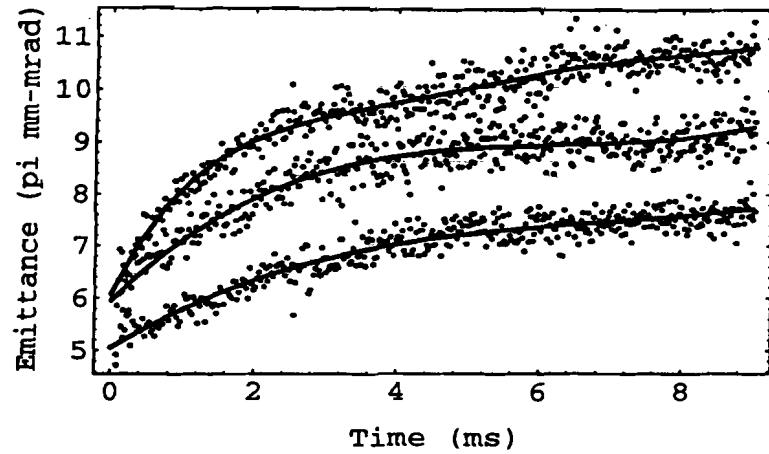
Figure 6.13: Vertical emittance at injection for 4, 5, 6 turns intensity.
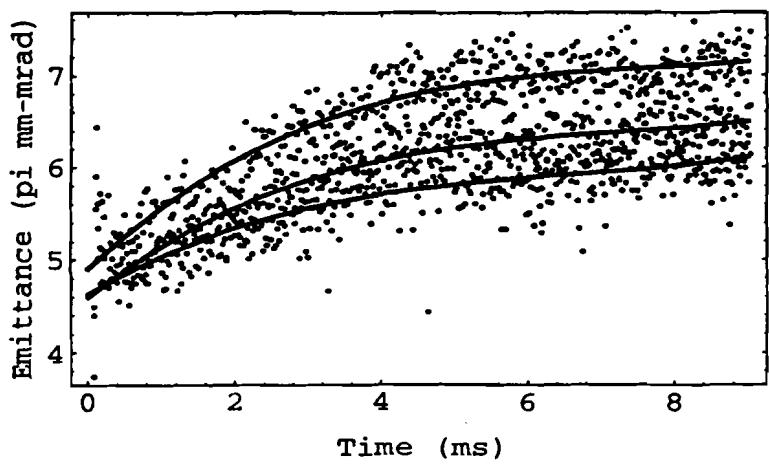
Figure 6.14: Vertical emittance at injection for 1, 2, 3 turns intensity.
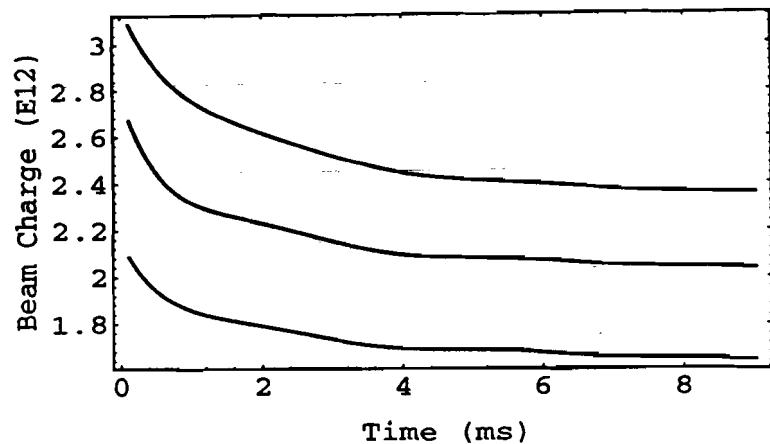
Figure 6.15: Beam charge at injection for 4, 5, 6 turns intensity.
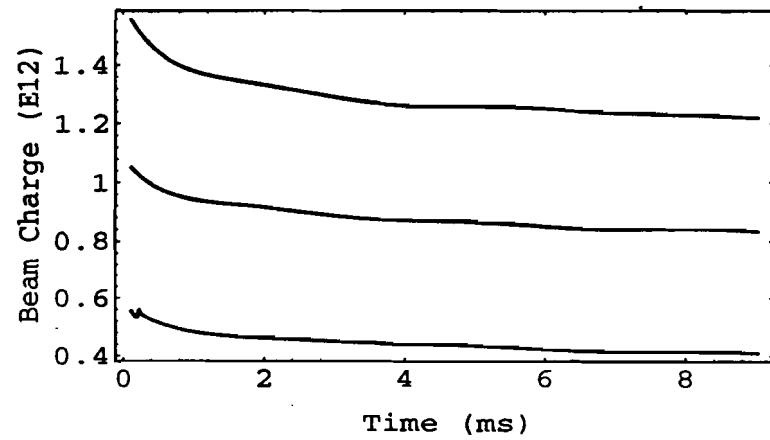
Figure 6.16: Beam charge at injection for 1, 2, 3 turns intensity.
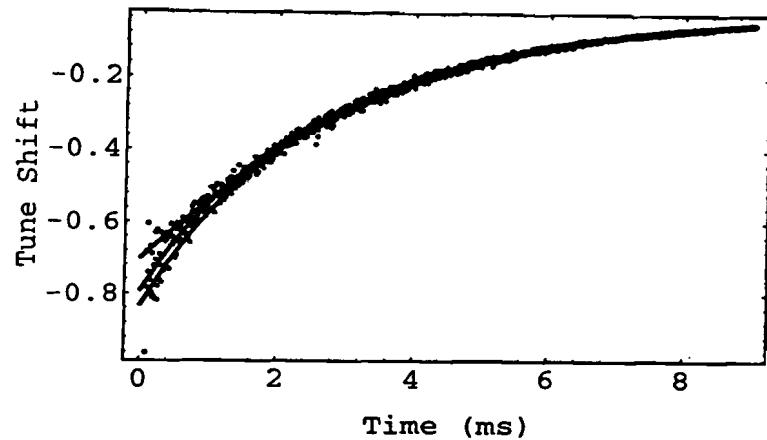
Figure 6.17: Tune shift at injection for 4, 5, 6 turns intensity.
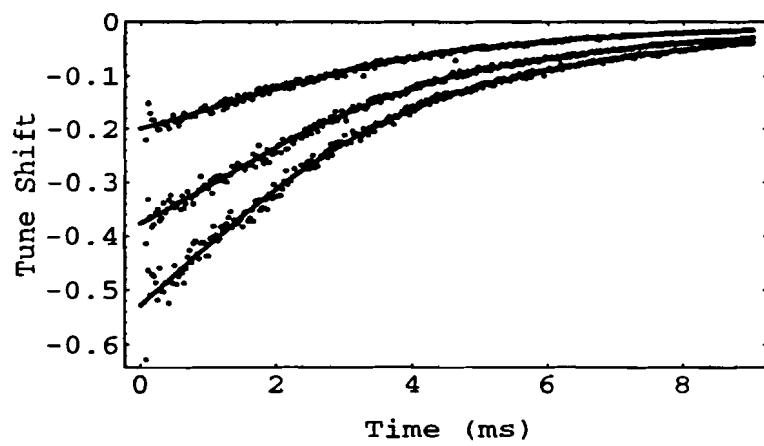
Figure 6.18: Tune shift at injection for 1, 2, 3 turns intensity.
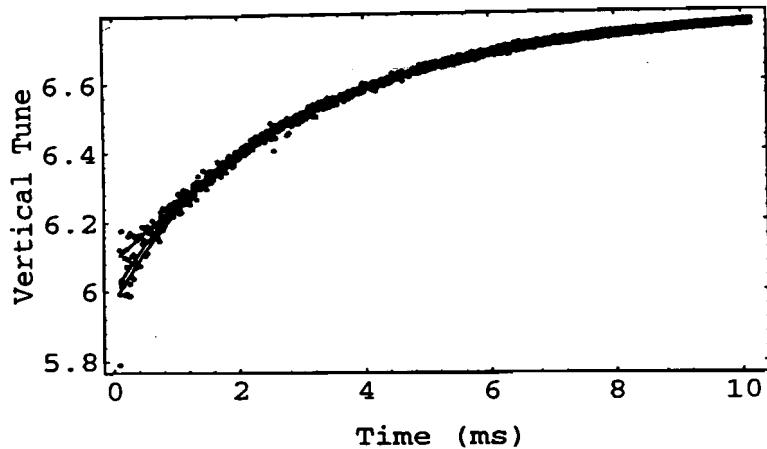
Figure 6.19: Space charge shifted vertical tunes for 4, 5, and 6 turns.
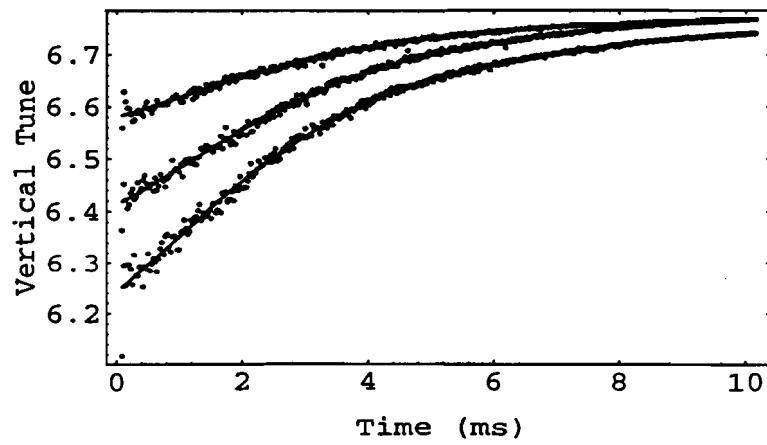
Figure 6.20: Space charge shifted vertical tunes for 1, 2, and 3 turns.

Table 6.1: Tune at injection for different intensities.

Intensity (turns injected)	Vertical Tune
1.0	6.78
2.0	6.79
3.0	6.77
4.0	6.79
5.0	6.79
6.0	6.80

Table 6.2: Emittance growth rates at injection.

Intensity (turns injected)	Growth Rate π mm-mrad/turn
1.0	2.26
2.0	2.30
3.0	3.32
4.0	3.50
5.0	6.13
6.0	6.56

the 4, 5, and 6 turn intensities, the emittance growth rates are quite different. The 6-turn case must sustain higher losses, thus faster growth, to maintain the same phase space density as the other cases.

6.3 Conclusions

The conclusions that may be drawn from these studies at injection are:

1. The tune shift due to space charge at injection is much larger than previously believed (approximately -0.8), and causes the beam to cross

the integer as well as the 1/2 integer resonance lines.

2. There is a maximum phase space density that the accelerator will support. This maximum will be reached through a combination of emittance growth and intensity reduction.

3. The emittance growth rate does not agree with previous computer simulations.

4. Even at high intensity (4.0 E12 injected) the emittance increases from 5.5 π mm-mrad at injection to 9.5 π mm-mrad 5 ms later, so that the space charge induced growth accounts for only 40% of the total emittance growth through the cycle.

In the next chapter we will describe the phenomena that cause the remainder of the emittance growth through the cycle.

Chapter 7

Measurements Throughout the Acceleration Cycle

The transverse emittance growth observed throughout the acceleration cycle was unexpected. After the initial growth due to resonance crossing at injection, a slower, linear growth is observed up until the time the transition energy is reached. At transition there are disturbances in the transverse beam shape that promote faster emittance growth until the end of the cycle. This growth after transition can account for as much as 40% of the total change in vertical emittance. First, the linear growth following injection will be described, and then the effects of transition on the transverse motion will be explained.

7.1   Linear Emittance Growth

Figure 7.1 shows the emittance for several intensities after the space-charge induced emittance growth has ended, but before transition time (5 - 15 ms into the cycle). The measured rates of emittance growth for this data are given in
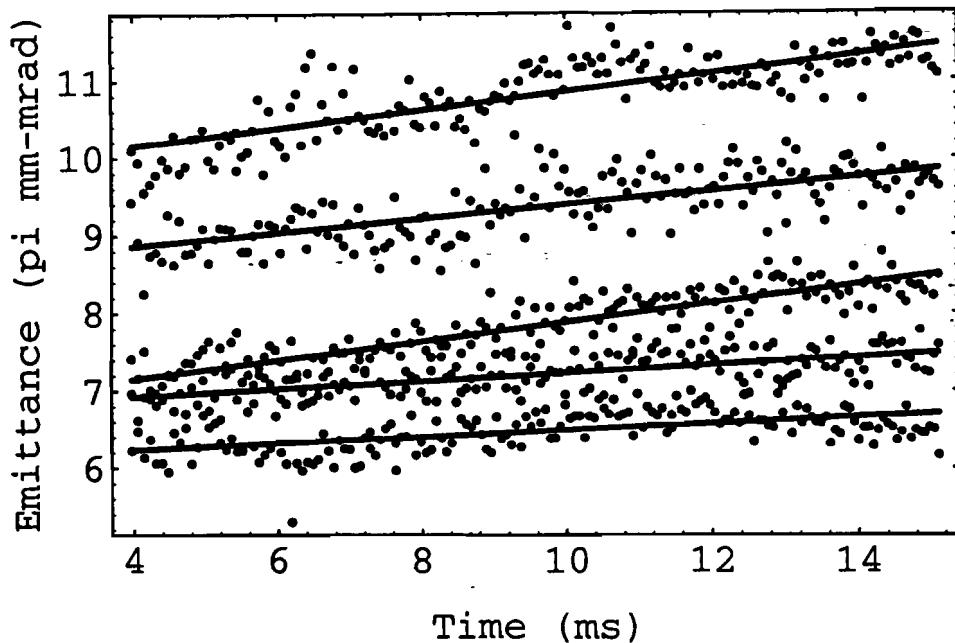
Figure 7.1: Emittances for 2, 3, 4, 5, and 6 turns from bottom to top respectively. Linear emittance growth is independent of intensity.

Table 7.1: Linear emittance growth rates of data in Figure 7.1. Units are 10^{-3} π mm-mrad/turn.

Intensity (turns injected)	Growth rate
2.0	0.07
3.0	0.09
4.0	0.21
5.0	0.15
6.0	0.20

Table 7.1. There is no clear dependence of growth-rate on intensity, which indicates that a noise source is probably the driving term. Recall Equation 3.35,

$$\frac{d\epsilon_N}{dt} = 3\pi\gamma f_0 D^2 \gamma_\ell \frac{e^2 \bar{V}^2}{\beta^3 E^2}. \tag{7.1}$$

Solve for $\bar{V}$ to get the rms amplitude of the noise voltage,

$$\bar{V}^2 = \frac{d\epsilon_N}{dt} \frac{\beta^3 E^2 \beta_\ell}{3\pi\gamma f_0 D e^2} \tag{7.2}$$

where we have assumed $\gamma_\ell = 1/\beta_\ell$

For a mean growth rate of $0.14 \times 10^{-3}\pi$ mm-mrad/turn, the rms amplitude of the noise voltage is 10.6 kV, or 1.5% of the accelerating voltage. This is only an estimate, but is quite plausible as an explanation of the cause of the linear increase in emittance.

7.2 Emittance Growth at Transition

The apparent drop in vertical emittance at transition (Figure 7.2) is due to two factors. First, when the γ_t quadrupoles pulse, the vertical amplitude function decreases from 20 meters to 19 meters for a few milliseconds before returning to its nominal value. This accounts for the majority of the change in beam size. Our emittance calculation assumes constant β_ℓ, which is true except for this period just after transition. Second, the apparent vertical beam width oscillation is an artifact of the IPM. As described in Section 5.4, the ratio of the transverse beam sizes has a small effect on the space-charge corrections that are applied to the profiles. This oscillation was useful for estimating the dependence of measured profile width on beam aspect ratio, but in the analysis to follow it will be ignored.
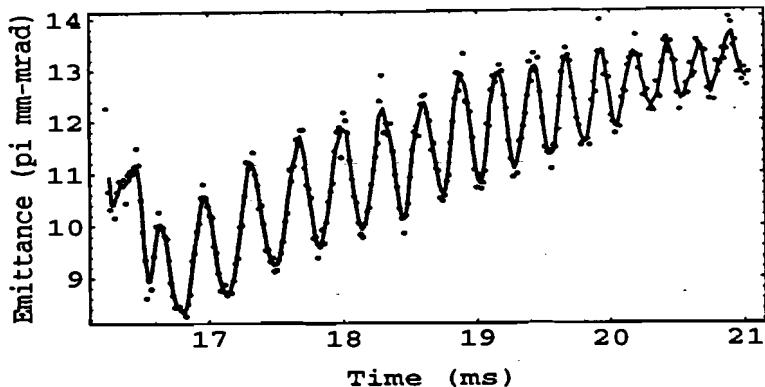
Figure 7.2: Sudden change in vertical emittance near transition, and ensuing oscillations at twice the synchrotron frequency.

In an ideal accelerator, the transition energy affects only the longitudinal beam dynamics, and should have no transverse effect. Depending on the state of the Booster, up to 40% of the total vertical emittance growth occurs after transition. This phenomena was not understood until the IPM was rotated a quarter turn about the beam pipe so that the horizontal profile could be measured. The horizontal *emittance* can't be measured with a single profile monitor due to the effects of momentum spread (see Chapter 2). Nevertheless, the raw profile data show striking horizontal effects that can be explained in terms of the longitudinal beam dynamics, and provides a mechanism for the vertical growth. The clues that longitudinal motion is responsible for these effects are that it occurs at transition, and there is a transverse oscillation at twice the *synchrotron* frequency (Figure 7.2), where $\omega_{sync} = 1.88$ kHz. We turn first to a description of how the longitudinal motion changes the

horizontal beam size, then relate that to the vertical emittance growth.

7.2.1   Horizontal Beam Profiles

Figure 7.3 shows a contour plot of the horizontal beam density throughout the cycle. Dark shades represent high intensity. There are several interesting features of the data:

1. The beam is a well-centered gaussian at injection.

2. After several thousand turns the gaussian becomes skewed toward small radius and the mean position also drifts to small radius.

3. At transition the beam widens substantially and begins a quadrupole oscillation.

4. Several thousand turns after transition the gaussian is skewed toward large radius and the centroid also drifts to large radius.

Each of these items are explained in the sections below.

Before Transition

Just after injection the beam shows a smooth gaussian profile (Figure 7.4). However, as acceleration begins and the peak current rises the bunch shape is distorted. The rf buckets that accelerate the bunches are parabolically shaped when the effect of the self-fields of the bunches is neglected. However, for an intense beam the self-fields distort the buckets.[11] The distortion causes the majority of particles to lead in phase, leading to a denser distribution at small radius below the transition energy (Figure 7.5).
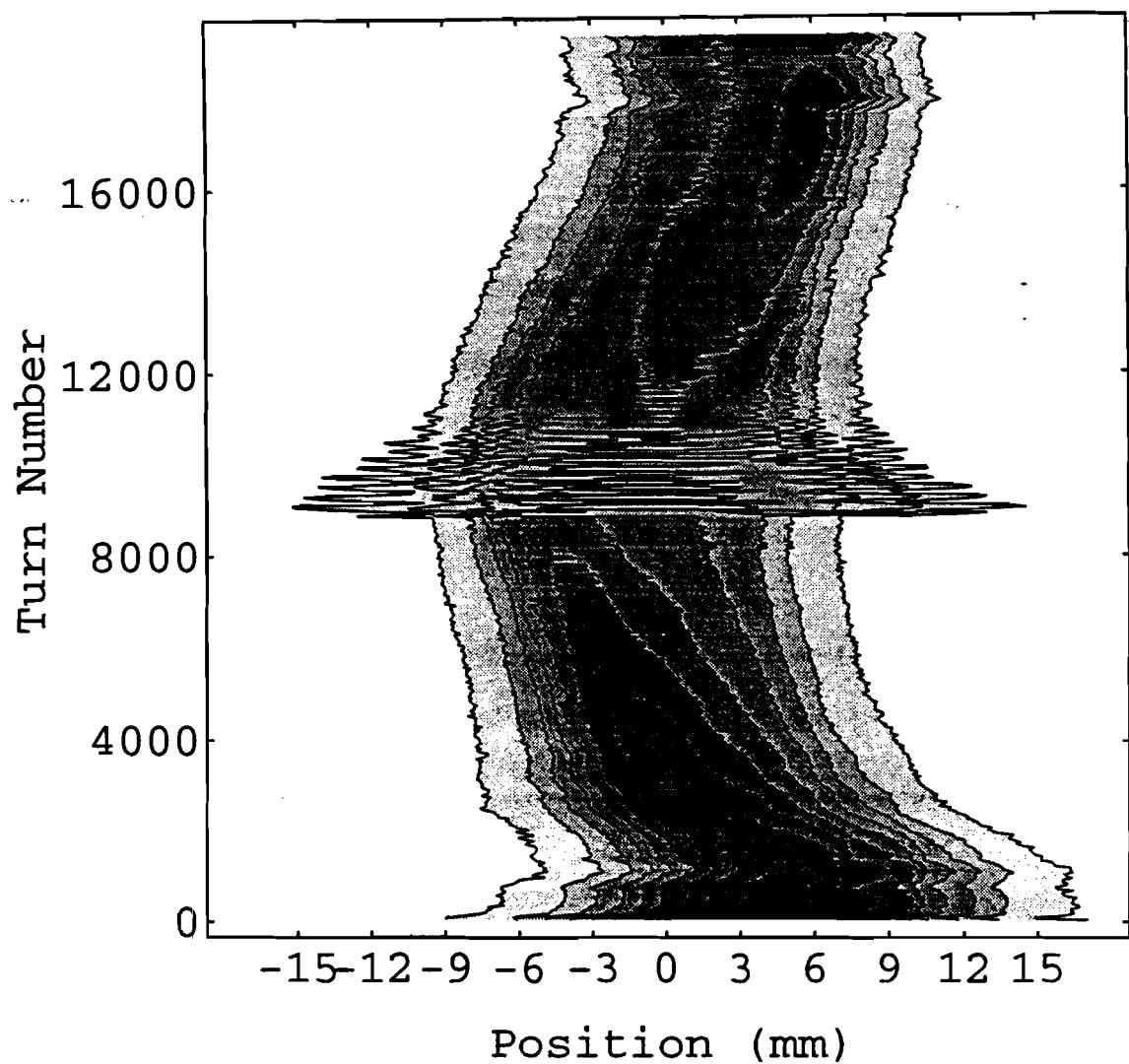
Figure 7.3: Contour plot of horizontal beam density through cycle for 6 turns injected.
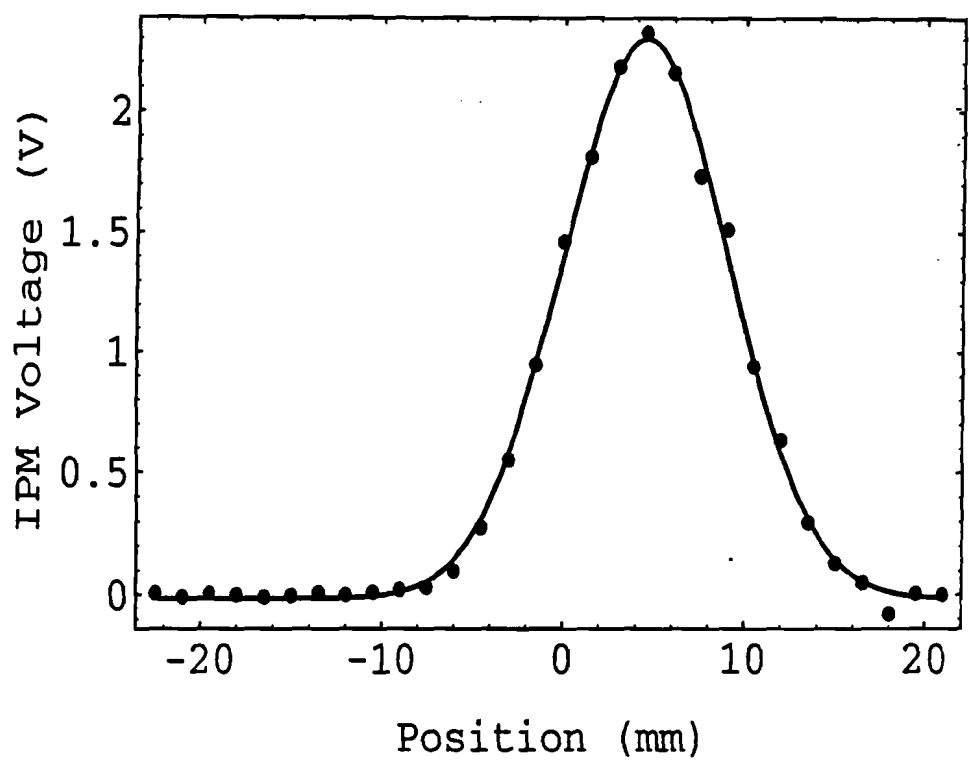
Figure 7.4: At injection the horizontal profile is gaussian in shape.

Figure 7.5: Horizonal beam profile below transition is distorted toward small radius by space charge (this profile is 14 ms into cycle).

The magnet ramps must be closely matched to the beam energy in order to maintain a constant radius throughout the acceleration cycle. The low-level rf system has the capability to adjust the average orbit radius during the cycle. The drift in radius observed is the curve that is programmed into the rf.

At Transition

From Section 2.3.5 the rms horizontal beam width is

$$\sigma_x = \sqrt{\frac{\epsilon_N \beta_\ell}{6\pi} + D^2 \left(\frac{\Delta p}{p}\right)^2}. \tag{7.3}$$

In the presence of dispersion D the beam width is sensitive to the spread in momentum $\frac{\Delta p}{p}$. Near transition the bunches become very short (Figure 7.6). Therefore, to conserve longitudinal emittance their momentum spread becomes large. When the γ_t quadrupoles pulse at transition, they change the lattice so that both D and β_ℓ are larger in the long straight sections. The Booster lattice has been modelled by the computer program MAD.[27] Simulation results[28] of the γ_t jump show that D changes from 2.0 meters to 2.3 meters, and horizontal β_ℓ changes from 5.3 meters to 5.8 meters. The increasing $\frac{\Delta p}{p}$, D, and horizontal β_ℓ all are responsible for the increase in width at transition.

Figure 7.7 is a contour plot of the beam density near transition. Figure 7.8 is helpful in visualizing what the contours mean. It is a mountain range plot of the first few oscillations shown in Figure 7.7. Just before the large oscillation the smooth skewed density distribution is visible. Recall that at transition, the synchronous phase must suddenly jump from the falling edge of the rf wave to the rising edge to maintain longitudinal focusing. If the phases aren't
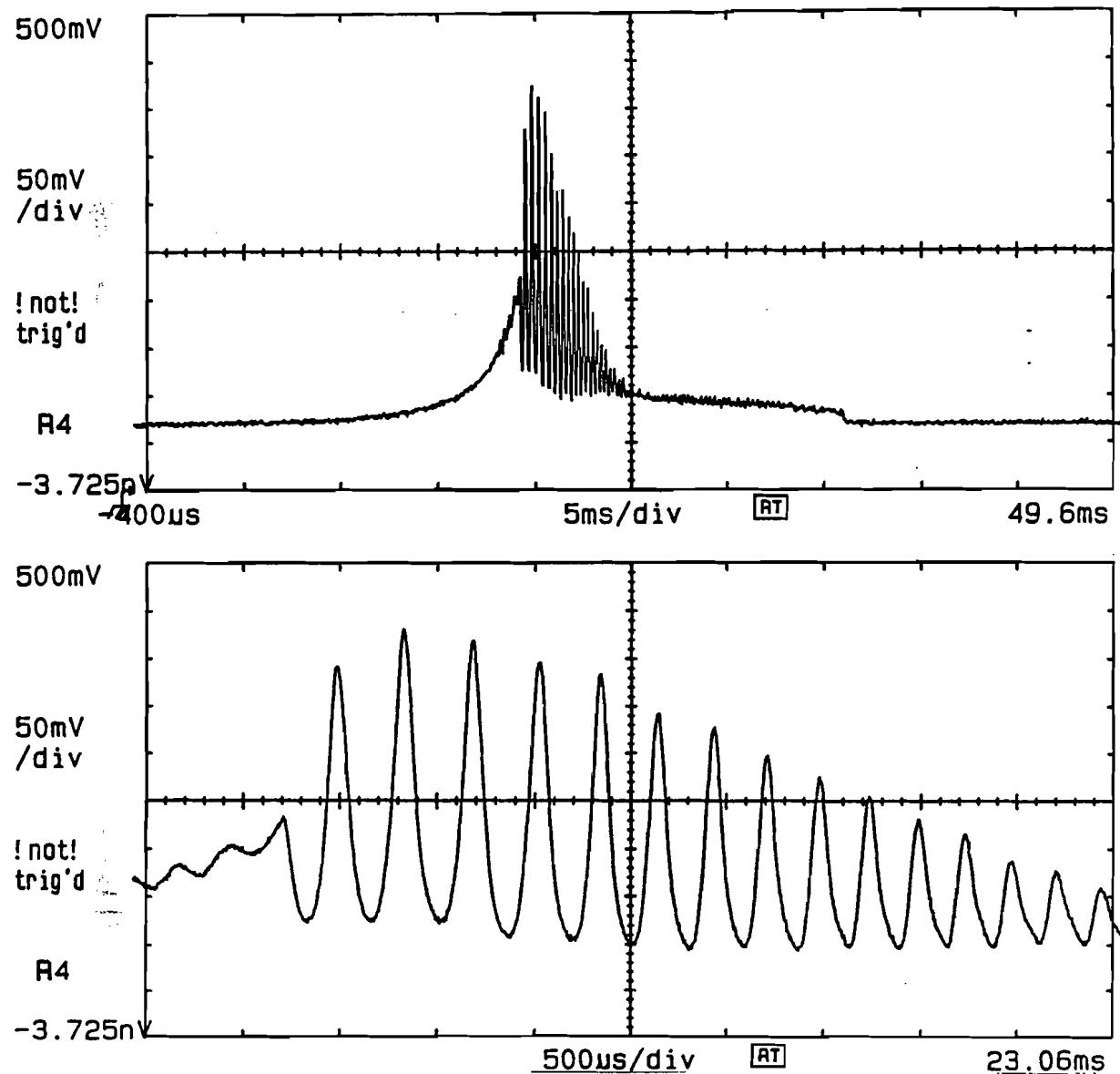
Figure 7.6: Signal from peak current monitor near transition. Large amplitude indicates short bunches.
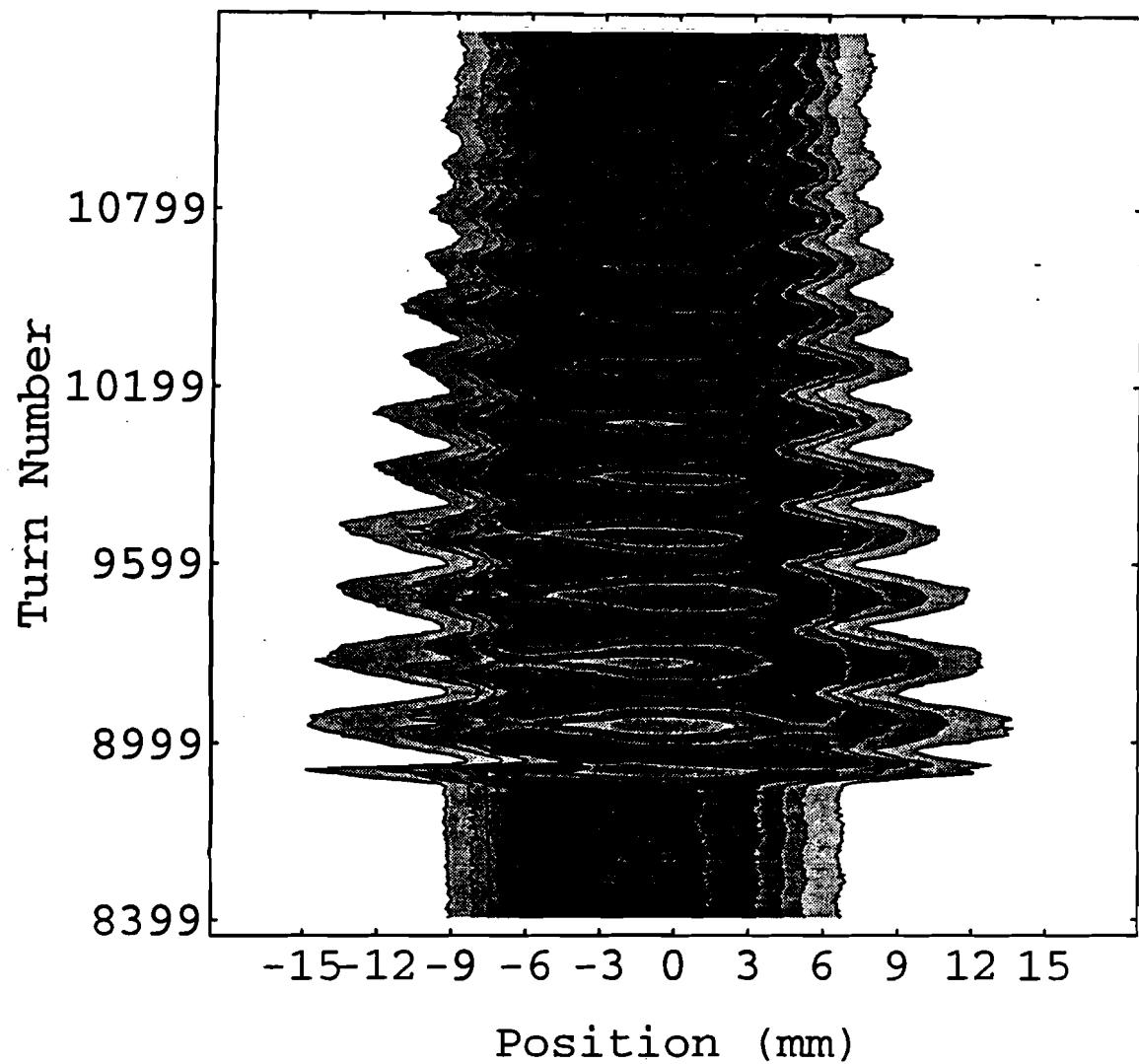
Figure 7.7: Contour plot of horizontal beam density at transition.
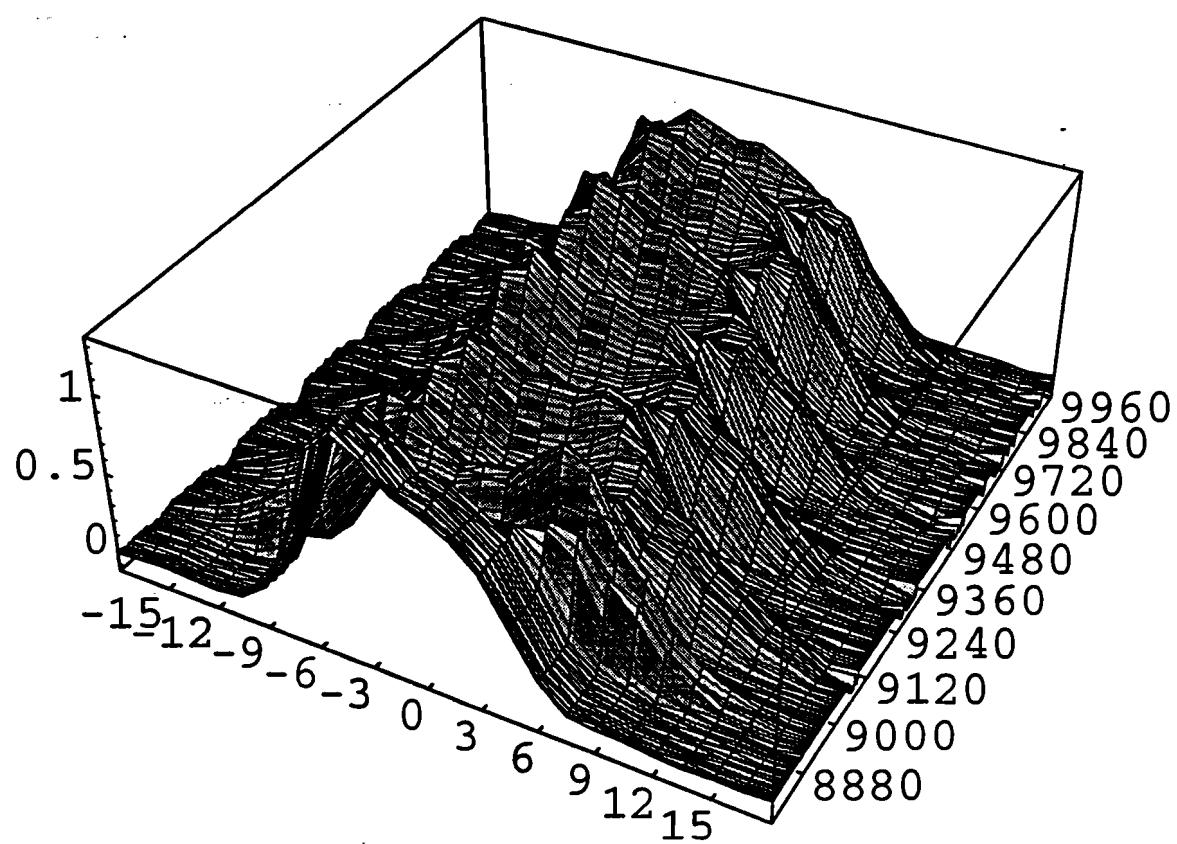
Figure 7.8: Mountain range plot of horizontal profiles at transition.

carefully matched, the bunch won't be centered in the rf bucket and phase space oscillations will result. This is the oscillation that is visible horizontally. The distribution shown clearly varies between a single central peak and twin peaks. The oscillation frequency is twice that of the synchrotron motion, which is consistent with a quadrupole distribution in longitudinal phase space (Figure 7.10). As the distribution rotates, its projection onto the energy axis varies from a single peak to the double peak. This motion is visible in the horizontal profile because of the large dispersion and energy spread.

The modulations may be damped by applying an rf voltage at the bunch frequency that is 90 degrees out of phase with the accelerating voltage. This has the effect of damping the spread in energy, thus shortening the bunch. In the brief time available to experiment with this damper before the current accelerator shutdown period it was found that the oscillation was effectively damped, but that the resulting short, high-intensity bunches excited multi-bunch transverse instabilities that caused severe beam loss just before extraction. When the accelerators are turned on again, this effect will be investigated in more detail.

After Transition

After the shape oscillations at transition damp out, the beam again maintains a skewed shape (Figure 7.11). However, the skew is then toward large radius. This is expected because the switch in synchronous phase above transition means that most of the particles are now at higher than synchronous energy, again distorting the rf bucket.
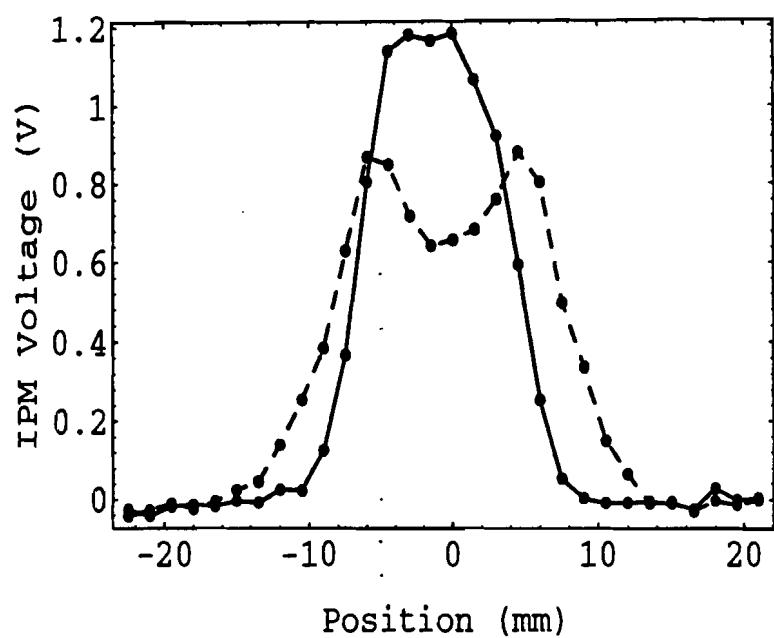
Figure 7.9: Horizontal profiles showing extremes of variation in beam shape during oscillations at transition.
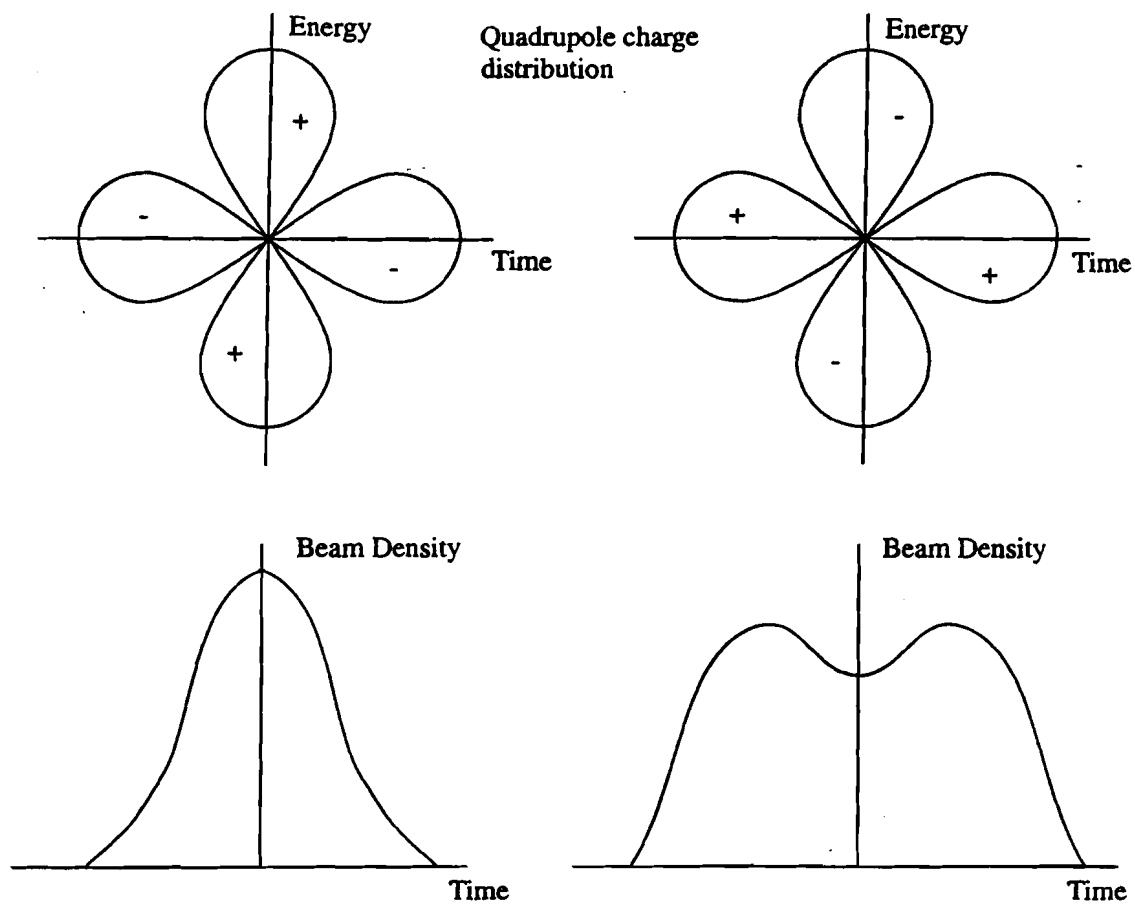
Figure 7.10: Rotating quadrupole distribution.
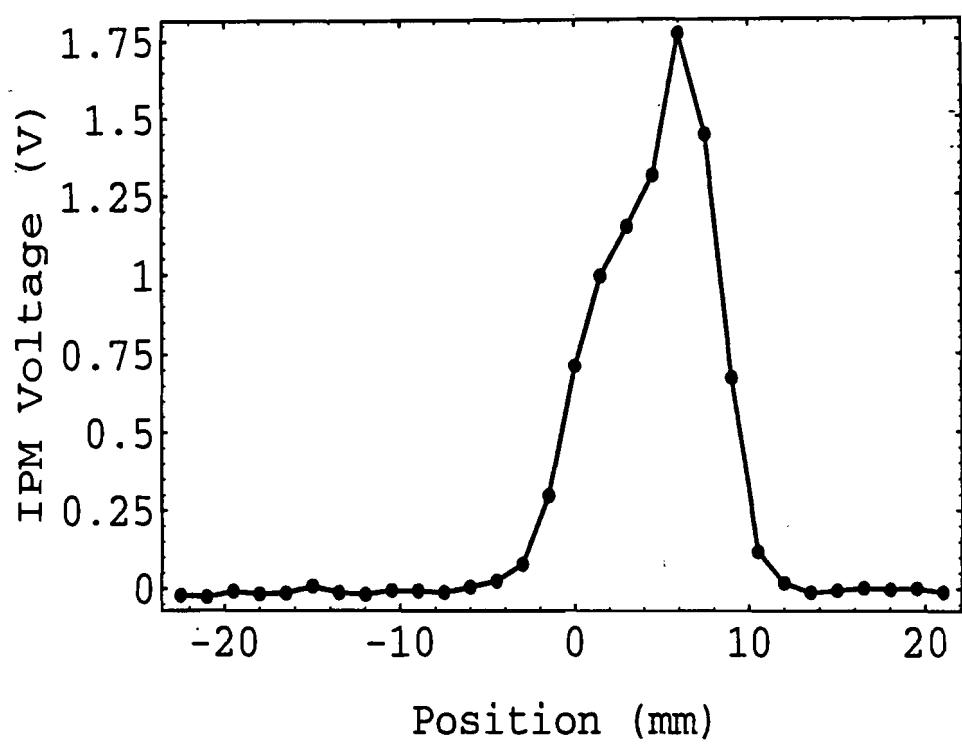
Figure 7.11: Horizontal profile near extraction after synchrotron oscillations have damped.

7.2.2 Effect of Transition on Horizontal Beam Size

The combined function magnets that are used to bend and focus the beam have a limited region near their axis where the optics are linear. The focusing fields are within 1% of their design value [3] up to ± 1 inch from the axis (Figure 7.12). Near transition, when the momentum spread is large, the beam may wander outside the good-field region. If this happens, horizontal emittance growth will result due to the incorrect quadrupole fields seen by the beam.

While we cannot directly measure the horizontal emittance with a single detector, it is possible to deduce that horizontal emittance growth *occurs* by observing the evolution of the beam width and the peak bunch intensity. The horizontal profile is not gaussian (nor any other simple distribution), therefore the full-width at half max will be used as a measure of the beam size. Figure 7.13 shows the beam width throughout the cycle, and Figure 7.14 shows the bunch intensity. The quadrupole oscillation is obvious in both sets of data. Note the rise in bunch intensity before transition when the rf phase jumps and the oscillations begin. This increase in the bunch intensity also marks increasing $\frac{\Delta p}{p}$. Also note that about 5 ms after the oscillation begins, it damps out and the intensity returns to its pre-transition value ($\frac{\Delta p}{p}$ also back to pre-transition value). However, the FWHM does *not* return to its pre-transition value - emittance growth has occurred. At about 10ms into the cycle the beam width is 9.0 mm. After the oscillation damps, the beam size has increased to 12.0 mm.

To estimate the maximum excursion of the beam, multiply the position of each channel by the ratio of the beta function in the short straight to that in the long straight. This is because in the long straight section where the IPM is

$k_1(F) = 2.2006 \ m^{-1}$

$k_1(D) = -2.7627 \ m^{-1}$

$B_o(F) = 7259 \ G$

$B_o(D) = 6152 \ G$
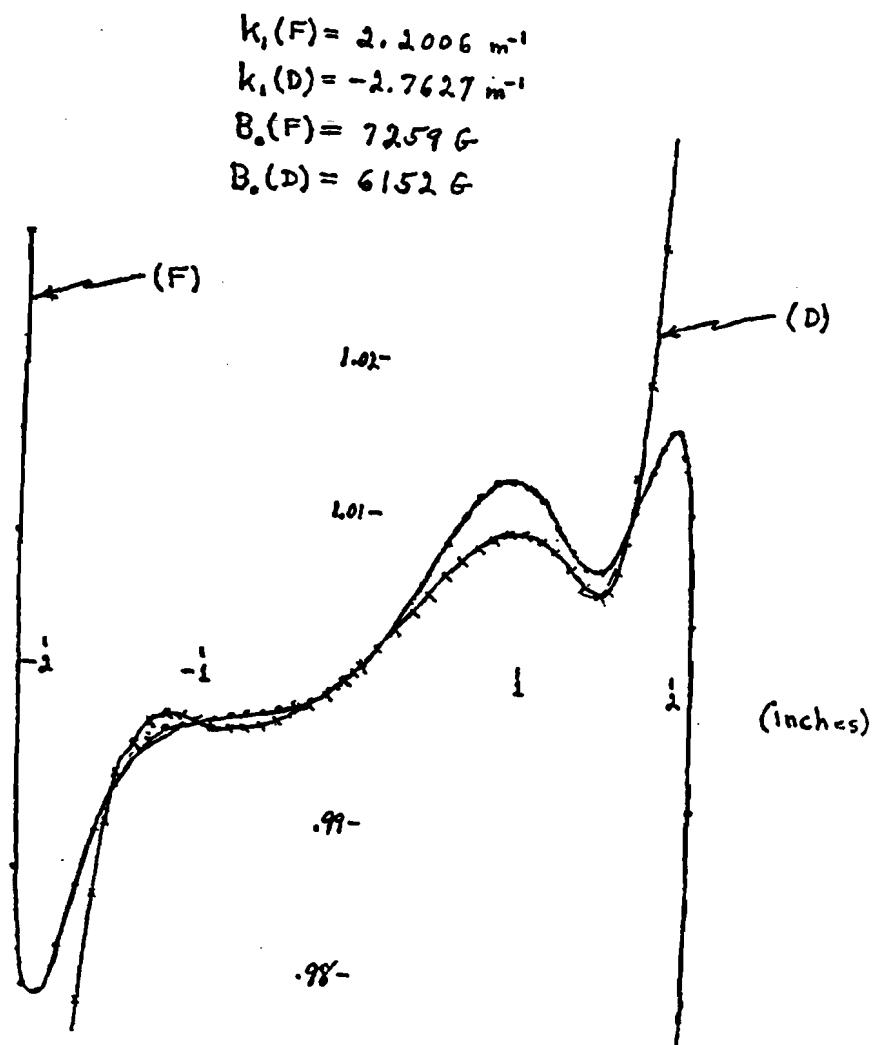
Figure 7.12: Normalized focusing strengths in the Booster quadrupole magnets.
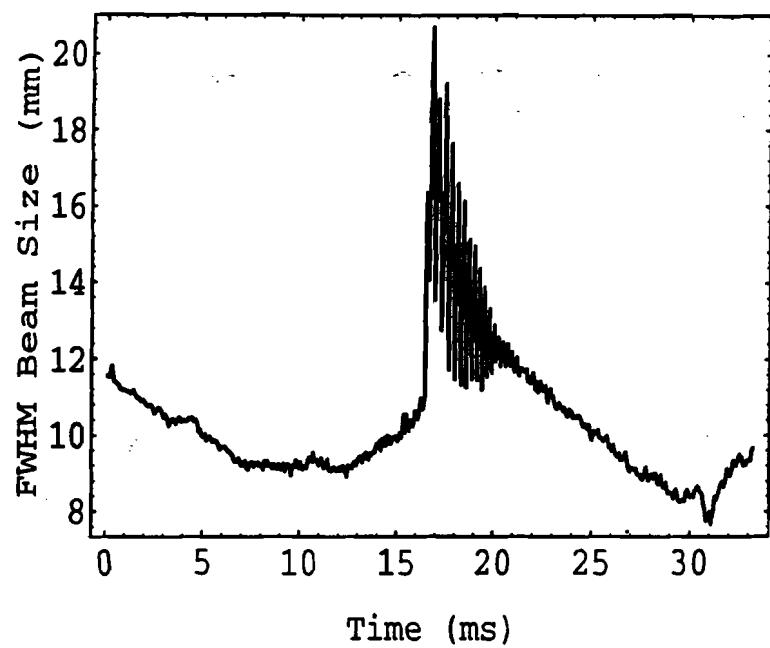
Figure 7.13: FWHM (6 turns intensity) for horizontal profiles throughout cycle.
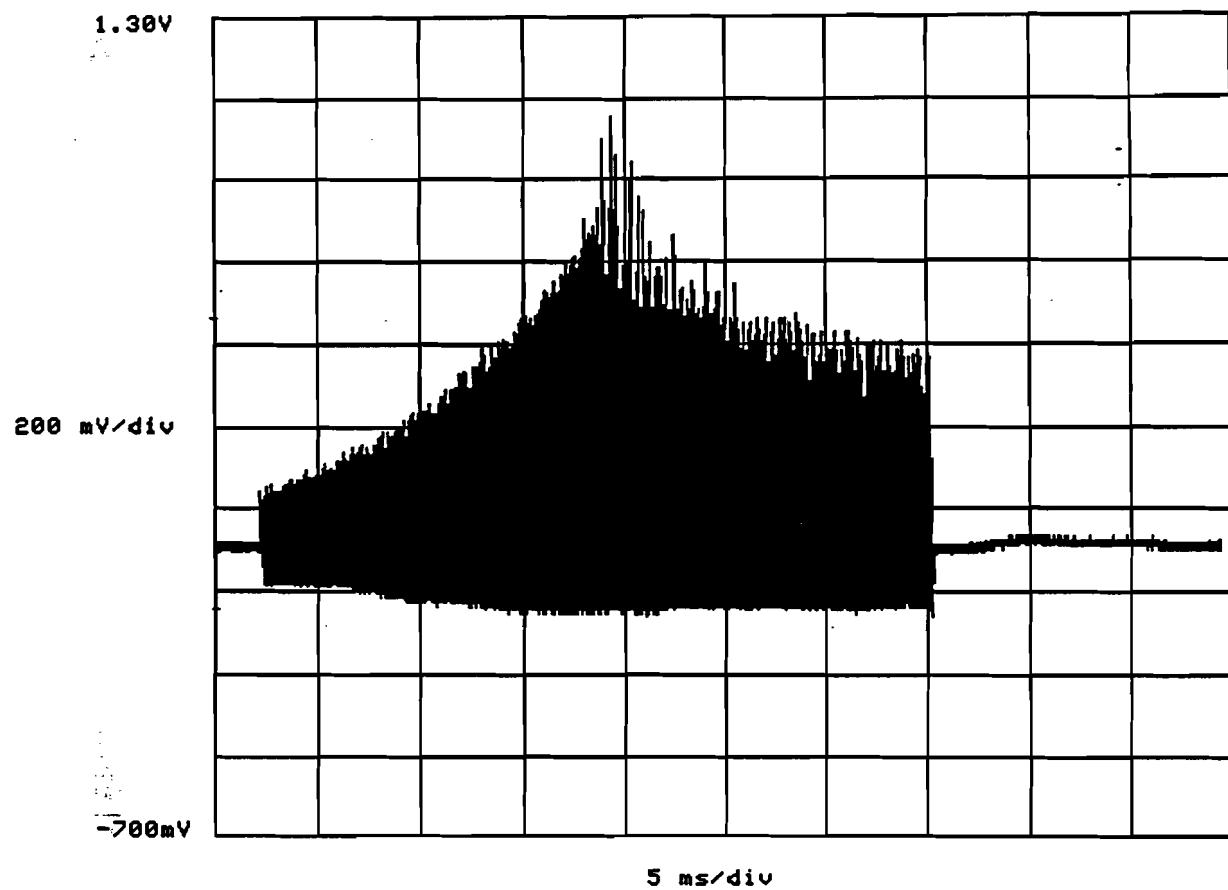
Figure 7.14: Bunch intensity signal throughout cycle. Provides a measure of the change in $\frac{\Delta p}{p}$.
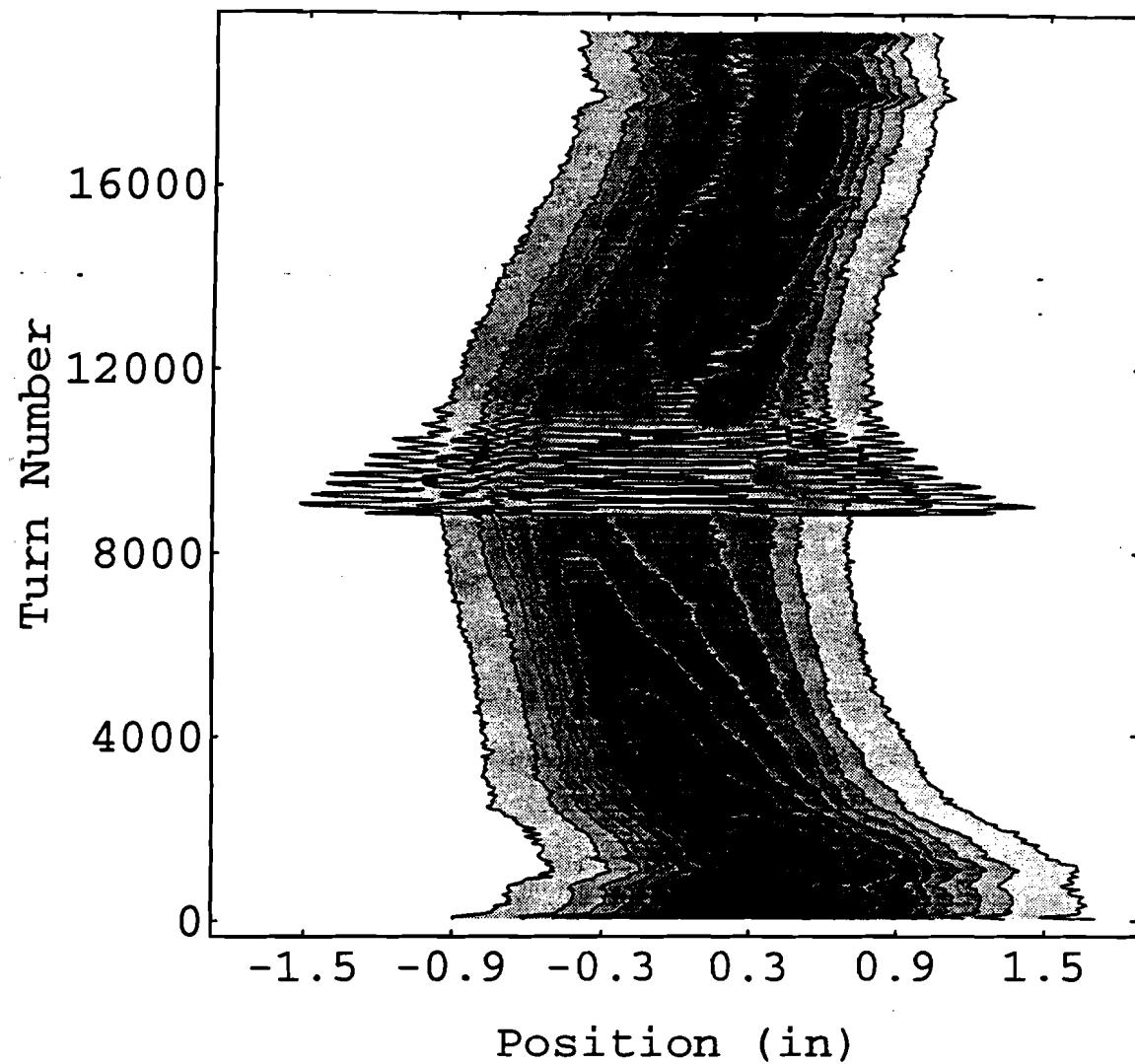
Figure 7.15: Maximum excursion of beam from magnet axis reaches limits of the good-field region. See text.

situated, the horizontal beta function is at a minimum. Figure 7.15 shows the results of this calculation. Distances are in inches to facilitate comparison with Figure 7.12. The edge of the beam passes the 1 inch mark at injection (where beam losses and rapid emittance growth are problems) and at transition. This amplitude is approximately where the focusing fields diverge rapidly from their design values. In light of this, it is not surprising that the beam width does not return to its pretransition value. In a sense, it has been stretched beyond its elastic limit.

The quadrupole oscillation is due to a phase space mismatch which is probably caused by two factors: The γ_t quadrupole magnets must be triggered at precisely the right time to change the lattice so that the beam passes through the transition energy quickly, and the usual rf phase shift must also be properly timed with regard to the transition energy. The correct implementation of these two important procedures is currently being studied with intent to improve upon the beam dynamics at transition. In the next section, horizontal profiles of different intensities are studied.

Horizontal Profiles at Different Intensities

Figure 7.16 shows the beam widths for different intensities throughout the cycle. Early in the cycle, the rate of change of width dw/dt for each case is the same. However, after transition, there is different behaviour for the high intensity vs low. For 2 turns injected, dw/dt is apparently unaffected by transition. Once $\frac{\Delta p}{p}$ returns to its pretransition value, the width continues to decrease as if transition had no effect. The beam has not strayed beyond the limits of the linear focusing optics in this case. As previously shown, for 6
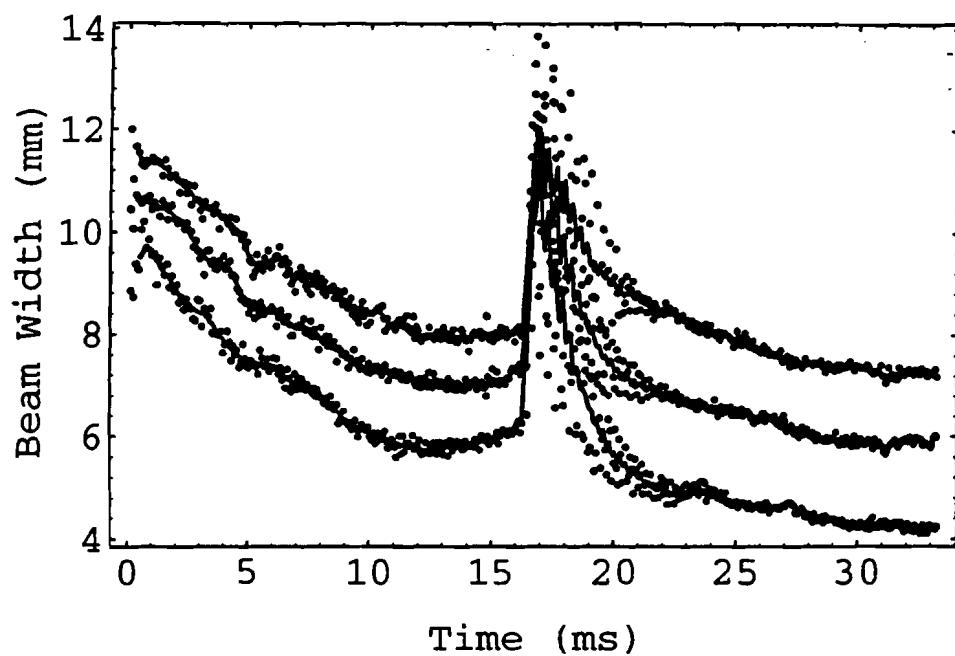
Figure 7.16: FWHM of horizontal beam for 2, 4, and 6 turns of beam injected.
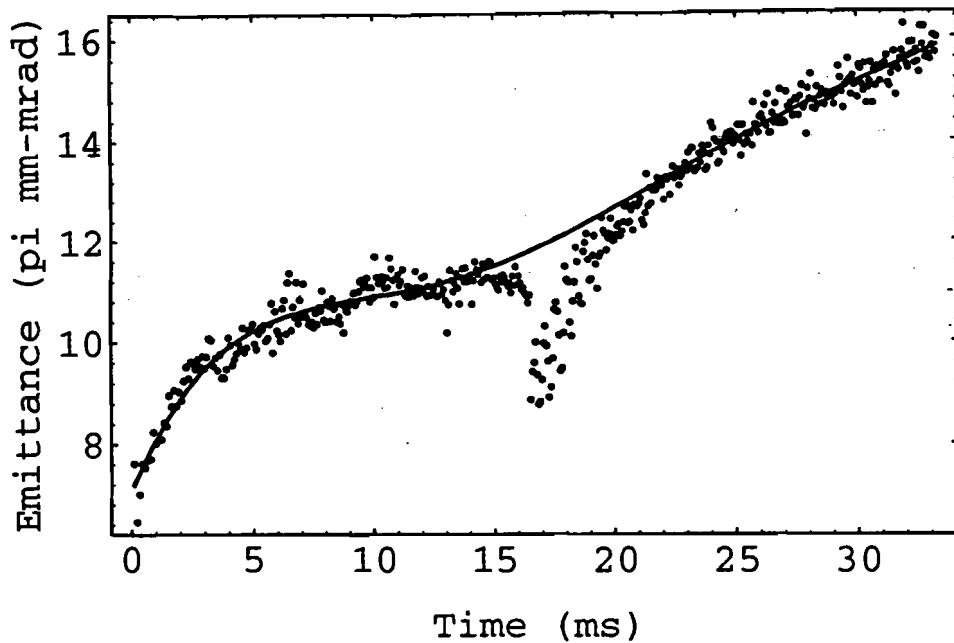
Figure 7.17: Vertical emittance throughout the cycle for 6 turns injected.

turns injected, transition does adversely affect the beam width, and it remains wider than its pretransition value.

7.3 Horizontal Coupling into Vertical Plane

The effects of longitudinal dynamics on the horizontal beam size through transition have been shown. The large variations in energy spread and lattice parameters can cause the beam width to grow irreversibly. These effects are also

evident in the vertical emittance data. Figure 7.17 shows the vertical emittance through the cycle. After the excursion at transition the linear rate of emittance growth increases. This is the increased horizontal emittance being coupled into the vertical plane. The coupling may be explained as follows: For any given magnet the vertical and horizontal directions are perpendicular. However, each magnet is imperfectly aligned with respect to the others. In particular, suppose that one of the combined-function magnets is rotated about the beam axis. The vertical motion of the beam is then affected by the bending fields, and nominally horizontal motion is observed in the vertical direction. Among the many magnets in the Booster, there is a distribution of alignment errors which introduce small amounts of coupling between the two transverse planes. The cumulative effect of all these errors is to couple the increasing horizontal emittance following transition into the vertical plane.

7.4 Vertical Emittance after Transition

In previous sections we looked at phenomena at injection and before transition. Here the effect of transition on the vertical emittance is studied. The vertical emittance after transition is shown in Figure 7.18 for several intensities. Following transition the rate of emittance growth is seen to increase and to remain linear in time. Table 7.2 gives the emittance growth rates for each intensity.

The rate of emittance growth following transition does appear to be mildly intensity dependent, with the high intensities and low intensities falling into two different growth-rate regimes. One explanation for this behavior is that
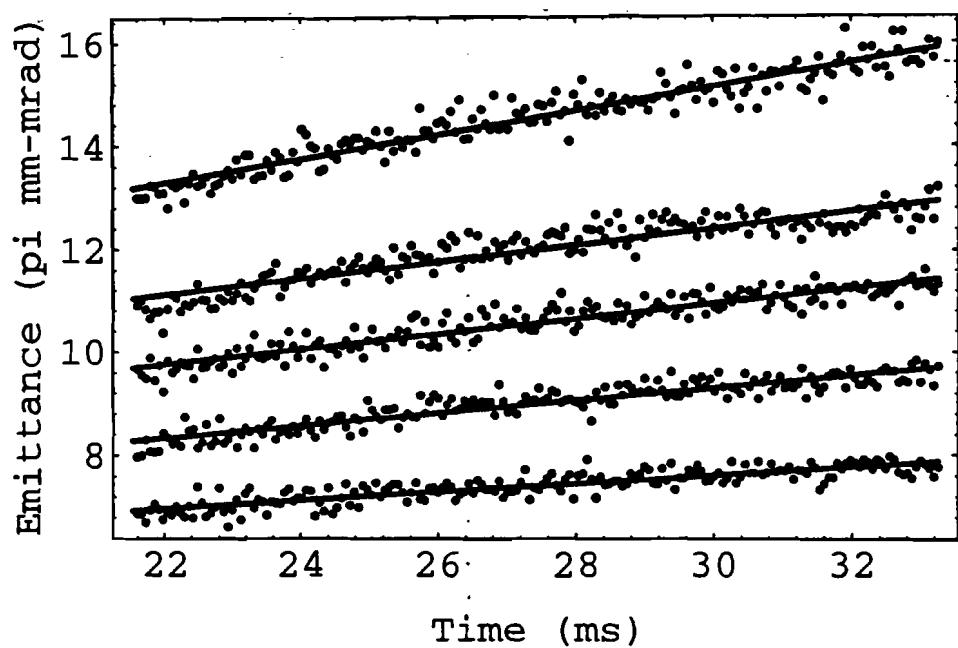
Figure 7.18: Vertical emittance after transition for 2, 3, 4, 5, and 6 turns intensity.

Table 7.2: Emittance growth rates following transition for different intensities. Units are 10^{-3} π mm-mrad/turn.

Intensity (turns injected)	Emittance Growth Rate
2.0	0.10
3.0	0.17
4.0	0.26
5.0	0.25
6.0	0.35

the more intense beams (4, 5, or 6 turns) are wide enough that the quadrupole oscillation at transition causes a large fraction of the beam to stray outside the linear focusing region, whereas a small fraction of the less intense beams wanders outside this good-field region.

7.5 Conclusions

The conclusions that can be drawn from observations of emittance throughout the cycle are:

1. Vertical emittance growth occurs throughout the cycle, and isn't limited to space-charge driven growth at injection.

2. The emittance growth before transition is linear in time and appears to be independent of intensity. It is probably driven by dipole kicks to the beam caused by rf noise at the betatron sidebands.

3. The crossing of the transition energy causes a large quadrupole oscillation at twice the synchrotron frequency which is visible in the horizontal profiles.

4. At high intensity, the longitudinal dynamics at transition irreversibly increase the horizontal beam size.

5. The horizontal motion couples into the vertical plane, causing the rate of emittance growth to increase after transition.

This completes the study of emittance growth in the Fermilab Booster. In the next chapter, all of the results and conclusions are pulled together and some suggestions for future studies are made.

Chapter 8

Summary, Conclusions, and Future Work

8.1 Summary of Experiment

This thesis has examined the evolution of the vertical emittance in the Fermilab Booster accelerator. To measure the beam profiles, a non-destructive ion profile monitor (IPM) was constructed. This monitor measures the profile on each successive orbit. It was found that space-charge forces due to the beam distort the profiles, but that the original width may be recovered by applying a correction generated by computer simulation. The emittances calculated from these corrected profiles agree well with other, independent devices. The IPM was then used to measure the emittance throughout the cycle at different intensities and for different operating conditions.

This is the first set of experiments where beam profiles in a circular accelerator have been recorded on a turn-by-turn basis. The IPM has enabled us to measure fast transverse emittance growth and to characterize its causes. The combination of fast response and noninterference with the beam make it a unique instrument for observing a beam of high-energy charged particles.

8.2 Conclusions

The original purpose of the experiment was to verify that space charge forces within the beam drove a tune shift that caused the tune to cross the $\nu = 6.5$ resonance line, and that this accounted for the observed beam losses and increased emittance.

It was found that the Laslett tune shift at injection is much larger than previously believed (0.8 *vs* 0.37) so that the tune crosses the integer as well as the 1/2 integer resonance lines. The emittance growth that is driven by this resonance-line crossing is found to be smaller and and to occur at a slower rate than previous work [1,5] indicated.

Even after beam losses end, and the tune no longer crosses nearby low-order resonance lines, the vertical emittance continues to increase. The observed increase is linear in time and independent of beam intensity. It is suggested that dipole kicks driven by noise in the rf system are responsible for this linear emittance growth.

Horizontal profiles were also measured, but because of the dependence of horizontal beam width on energy spread, an absolute determination of horizontal emittance is not possible with a single detector. However, this dependence of width on energy spread enabled us to observe longitudinal effects in the transverse plane. In particular, bunch distortion due to space charge was seen, and a significant phase-space mismatch at the transition energy was observed. This mismatch caused width oscillations at twice the synchrotron frequency after which the horizontal beam size was irreversibly increased.

Coupling between the horizontal and vertical planes caused the rate of

Table 8.1:   Emittance growth rate at different intensities.   Units are $10^{-3} \pi$ mm-mrad/turn.

Intensity (turns injected)	Time in Cycle (ms)		
	0 - 5	5 - 15	20 - 30
2.0	2.30	0.07	0.10
3.0	3.32	0.09	0.17
4.0	3.50	0.21	0.26
5.0	6.13	0.15	0.25
6.0	6.56	0.20	0.35

emittance growth to increase following transition. Table 8.1 summarizes the observed rates of emittance growth at different times and intensities in the Booster.

8.3   Future Work

The measurements made with the IPM have raised more questions than they have answered. The emittance increase at injection should be helped considerably by the upgrade in linac energy from 200 to 400 MeV. However, this only accounts for about 1/2 of the total increase in emittance. An effort is underway to build dampers that will reduce the effect of the rf noise on the beam. Their design is complicated by the fast ramp in energy and slew in orbit frequency of the Booster. When the dampers are installed in the coming months, experiments should be done to determine in more detail the emittance growth caused by the rf system.

The combination of the dampers and increased injection energy will cause a more intense, smaller emittance beam to be successfully accelerated to high

energy. However, there is evidence that the problems at transition are intensity dependent, so that they may be exacerbated by the improvements at injection. More studies are needed of transition crossing to ensure that high intensity, low emittance beam is delivered by the Booster. To carry out these studies, two horizontal profile monitors should be installed in regions of different dispersion so that the true horizontal emittance can be measured.

The insights into beam behavior that the IPM provides, and the improvements in performance that result, should guarantee that the Booster is able to meet requirements for high quality beam well into the future.

Appendix A

Accelerator Terms

Betatron Frequency(ν) The number of oscillations a particle makes about the reference trajectory in one orbit around the accelerator. Also called the transverse tune.

Bucket The longitudinal phase space area available to the beam. Also called an rf bucket.

Bunch A group of particles confined to one rf bucket.

Chromaticity (ξ) The spread in betatron frequency due to momentum differences.

Courant-Snyder Parameters Parameters that characterize the accelerator lattice. See Chapter 2.

Decoherence When coherent betatron oscillations are induced in a beam, the oscillations will decohere with time because the individual particles have slightly different oscillation frequencies. This will increase the beam's emittance.

Design Orbit An idealized orbit that the accelerator design is based on. Particles oscillate about the design orbit. Also called the reference orbit

or trajectory.

Dispersion(D) The change in bending radius of a particle due to a difference in energy.

Emittance(ϵ) The phase space area occupied by some fraction of the beam. Most often refers to the area in just one of the three planes that describe the six dimensional phase space.

Emittance, Normalized(ϵ_N) When multiplied by $\gamma\beta$, the emittance is normalized to be invariant throughout the acceleration cycle.

Energy, Units of MeV$= 10^6$ electron-volts, GeV $= 10^9$ eV, TeV $= 10^{12}$ eV.

Filamentation See *Decoherence.*

Instability An oscillation in particle motion that feeds back on itself causing the amplitude of the motion to grow. Undesireable.

Harmonic Number(h) The ratio of the rf frequency to the orbit frequency. Determines the maximum number of bunches in the ring.

Luminosity(L) Number of collisions per second per unit area between colliding beams. High L is one of the primary goals of accelerator designers.

Longitudinal In the primary direction of particle travel. Along the circumference of the ring.

Quadrupole Magnet The most common type of focusing magnet.

RF Cavity A resonant cavity that transfers electomagnetic energy to particle kinetic energy.

Sextupole Magnet Has the property of focusing strength that varies with transverse position. Useful for correcting momentum-dependent effects.

Synchronous Particle The particle which has energy such that its phase with respect to the rf voltage is constant from turn to turn.

Transition Energy(γ_t) The kinetic energy at which path length is independent of energy. Longitudinal focusing is lost at this energy.

Transverse Perpendicular to the primary direction of particle travel.

Tune, Horizontal and Vertical See *Betatron Frequency.*

Tune, Synchrotron Number of longitudinal oscillations a particle makes about the synchronous particle in one orbit of the accelerator. Also called longitudinal tune.

Tune Space Two dimension space where ν_x and ν_y are the axes.

References

1. S. M. Stahl. *Beam Dynamics in the Fermilab Booster in the Presence of Space Charge.* PhD thesis, Northwestern University, 1991.

2. E.D. Courant and H. S. Snyder. Theory of the alternating gradient synchrotron. *Ann. Phys. 3, 1 (1958).*

3. E.L. Hubbard, Editor. Booster synchrotron, 1973. Fermi National Accelerator Laboratory, TM-405.

4. S. Machida. *Space Charge Effects in Low Energy Proton Synchrotrons.* PhD thesis, University of Houston, 1990.

5. C. Ankenbrandt and S. D. Holmes. Transverse beam motion in the fermilab booster. In *Proceedings of the 1987 IEEE Particle Accelerator Conference,* 1987.

6. D. A. Edwards and M. J. Syphers. *An Introduction to the Physics of High Energy Accelerators.* John Wiley & Sons, Inc., 1993.

7. A.V.Tollestrup and G. Dugan. Elementary stochastic cooling. In *Physics of High Energy Particle Accelerators,* 1983. AIP Conf. Proc. 105.

8. G.I. Budker. In *Proc. 1966 Int. Symp. Electron and Positron Storage Rings,* 1967.

9. M. Sands. The physics of electron storage rings - an introduction, 1970. SLAC publication SLAC-121, UC-28 (ACC).

10. L. J. Laslett. On intensity limitations imposed by transverse space charge effects in circular particle accelerators. In *Proceedings of the 1963 Summer Study on Storage Rings*, 1963.

11. A. W. Chao. *Physics of Collective Beam Instabilities in High Energy Accelerators*. John Wiley & Sons, Inc., 1993.

12. A. Piwinski and A. Wrulich. DESY 76/07 (1976).

13. T. Suzuki. Synchrobetatron resonance driven by dispersion in rf cavities. *Particle Accelerators Vol. 18*, 1985.

14. D. P. McGinnis. Coupled bunch mode instabilities measurement and control. In *Accelerator Instrumentation, Third Annual Workshop*, 1991.

15. K. Robinson. Stability of beam in radio-frequency systems, 1964. CEAL-1010.

16. U. Fano. *Ann. Rev. Nucl. Sci. 13*, 1963.

17. *Characteristics and Applications of Microchannel Plates*. Hammamatsu Technical Manual RES-0795.

18. J. Gayrete. Collective phenomena and instabilities. In *Advances of Accelerator Physics and Technologies*. World Scientific Publishing Co., 1993.

19. J. Krider. Residual gas beam profile monitor. *Nuclear Instruments and Methods A278*, 1989.

20. Galileo Electro Optics Corp., Sturbridge, MA, USA.

21. Model AH0014 from Optical Electronics Inc., P.O.Box 11140, Tucson, AZ 85734.

22. *ACNET Console Users Guide.* Fermilab Software Doc. Memo 62.3, June 23, 1985.

23. Proceedings of the Accelerator Instrumentation Workshops, published by AIP.

24. Vector Fields Limited, 24 Bankside, Kidlington, Oxford OX5 1JE, England. *PE2D Reference Manual, Version 8.3*, 1991.

25. Wolfram Research, Inc. *Mathematica.* Wolfram Research, Inc., Champaign, IL, 1993. Version 2.2.

26. R. E. Thern. Space-charge distortion in the brookhaven ionization profile monitor. In *Proc. of the 1987 IEEE Particle Accelerator Conf.*, 1987.

27. F. C. Iselin H. Grote. The mad program user's reference manual, v8.4, 1992. CERN SL/90-13 Revision 2.

28. J.-P. Shan, 1993. Private communication.